Ph.D. Thesis

Structural, magnetic and dielectric properties of $NiFe_2O_4$ – $BaTiO_3$ magnetoelectric multiferroic composites

Prakash Bongurala

School of Physics
University of Hyderabad
Telangana, India

November, 2020

UNIVERSITY OF HYDERABAD

DOCTORAL THESIS

Structural, magnetic and dielectric properties of $NiFe_2O_4-BaTiO_3$ magnetoelectric multiferroic composites

---

A thesis submitted in partial fulfillment of
the award of the degree of
Doctor of Philosophy

in

Physics

by

Mr. Prakash Bongurala

[Reg. No.: 14PHPH10]

School of Physics
University of Hyderabad
Hyderabad 500 046
Telangana, INDIA

November, 2020

DECLARATION

I hereby declare that the matter embodied in this thesis entitled, "**Structural, magnetic and dielectric properties of $NiFe_2O_4-BaTiO_3$ magnetoelectric multiferroic composites**", is the result of investigations carried out by me in the School of Physics, University of Hyderabad, Hyderabad, India under the supervision of **Dr. Venkataiah Gorige**.

Place: Hyderabad
Date: 23.11.2020

Prakash Bongurala
Reg. No. 14PHPH10

CERTIFICATE

This is to certify that the thesis entitled, "**Structural, magnetic and dielectric properties of $NiFe_2O_4-BaTiO_3$ magnetoelectric multiferroic composites**", submitted by **Mr. Prakash Bongurala** bearing the registration number: 14PHPH10 in partial fulfillment of the requirements for the award of Doctor of Philosophy in Physics at the School of Physics is a bonafide work carried out by him under my direct supervision.

This thesis is free from plagiarism and has not been submitted previously in part or in full to any other University or Institution for the award of any degree or diploma.

Further, the student has the following publications and conference proceedings before the submission of the thesis for adjudication.

Papers in Refereed Journals

(2) Correlation between size, shape and magnetic anisotropy of $CoFe_2O_4$ ferrite nanoparticles.
Avisek Das, Kranthi kumar Bestha, **Prakash Bongurala** and Venkataiah Gorige
Nanotechnology **31,** 335716 (2020).

(1) Structural, magnetic and electric properties of multiferroic $NiFe_2O_4-BaTiO_3$ composites
Prakash Bongurala and Venkataiah Gorige
J. Magn. Magn. Mater. **477,** 350 (2019).

Manuscripts under preparation

(2) Temperature dependent structural and magnetic properties of $NiFe_2O_4-BaTiO_3$ magnetoelectric multiferroic particulate composites.
Prakash Bongurala and Venkataiah Gorige.

(1) The dielectric and ESR properties of ferrite−ferroelectric magnetoelectric multiferroic composites.
Prakash Bongurala and Venkataiah Gorige.

Conferences attended

(9) Internatinal Conference on Magnetic Materials and Applications (ICMAGMA-2018) held at School of Physical Sciences, National Institute of Science Education and Research (NISER), Bhubaneswar, Odisha, India, during 9^{th} - 13^{th} December 2018.
Poster presentation "*Low temperature Raman spectroscopy of NFO−BTO composites*".

(8) Functional magnetic materials workshop held at UGC-NRC, School of Physics, University of Hyderabad, Telangana, India, during 9^{th} February - 3^{rd} March 2018.
(Participated).

(7) International symposium on integrated functionalities (ISIF-2017) held at Shangri − La's Eros Hotel, New Delhi, India, during 10^{th} - 13^{th} December 2017.
Poster presentation"*Magnetoelectric multiferroic behavior in ferrimagnetic - ferroelectric composites* "

(6) National conference on Physics at small scales and advanced materials (PSAM-2017) held at School of Physics, University of Hyderabad, Telangana, India, during 8^{th} - 9^{th} September 2016.
Poster presentation "*Magnetoelectric coupling in $NiFe_2O_4-BaTiO_3$ composites* "

(5) Frontiers in Physics (FIP-2016) held at School of Physics, University of Hyderabad, Telangana, India, during 9^{th} February - 3^{rd} March 2016.
(Participated).

(4) CSR lecture series, UGC-DAE Consortium for scientific research, Indore, Madhya Pradesh, India, during 14^{th} - 25^{th} September 2015.
(Participated).

(3) Recent advances in smart materials and probing techniques (RASMPT-2015) held at Department of Physics, Telangana University, Bhiknur, Nizamabad, Telangana, India, during 21^{st} - 22^{nd} August 2015.
(Participated).

(2) 25^{th} National symposium on cryogenics (NSC-2014) held at School of Physics, University of Hyderabad, Telangana, India, during 8^{th} - 10^{th} December 2014.
(Participated).

(1) Frontiers in Physics (FIP-2014) held at School of Physics, University of Hyderabad, Telangana, India, during 17^{th} - 18^{th} October 2014.
(Participated).

Further, the student has completed the following courses towards the fulfillment of course-work required for Ph.D.

S.No.	Course code	Name of the course	Credits	Pass/Fail
1	PY801	Advanced Quantum Mechanics	4	Pass
2	PY803	Advanced Statistical Mechanics	4	Pass
3	PY804	Advanced Electromagnetic Theory	4	Pass
4	PY821	Research Methodology	4	Pass

Dean
School of Physics

DEAN
School of Physics
University of Hyderabad
Hyderabad-500 046, INDIA.

23/11/2020

Dr. Venkataiah Gorige
Thesis Supervisor
School of Physics

Dr. VENKATAIAH GORIGE
Assistant Professor
School of Physics, University of Hyderabad
Gachibowli, Hyderabad 500046, INDIA

ACKNOWLEDGEMENTS

I am pleased to express my deepest gratitude and sincere thanks to my mentor and supervisor Dr. Venkataiah Gorige for giving me an opportunity to join his research group and for supporting me in carrying out different experiments to accomplish my dream. My work was benefited greatly from his immense knowledge and commitment while I learned so much through our numerous discussions. Moreover, I would like to thank him for his caring attitude and concern. I never felt under pressure, which was not only important for me in terms of my research, but also for me personally, especially during the hard times that I had to endure.

I would like to take this opportunity to thank my doctoral review committee members Prof. K. C. James Raju, Prof. S. Srinath for their valuable suggestions and useful questions.

I am thankful to the present Dean, Prof. Ashok Chatterjee and former Deans, Prof. V. Seshubai, Prof. Bindu A. Bambah, Prof. Rajender Singh and Prof. S. Chaturvedi.

I am obliged to Professor-in-charge, Center for Nanotechnology, University of Hyderabad, for allowing me to use Physical Property Measurement System for carrying out the magnetic measurements and scanning near-field optical microscope for Raman measurements. I wish to thank Mr. G. Pranshanth for Raman measurements. I wish to thank Mr. Sudhakar, Mr. Balakrishan and Ms. Jyothi for x-ray diffraction measurements. I thank Dr. L. Venkatesh, International Advanced Research Centre for Powder Metallurgy and New Materials (ARCI), Hyderabad for Field Emission Scanning Electron Microscopy measurements. My special thanks to Mr. T. Abraham, Mrs. Shailaja, Mr. Prasad, Mrs. Deepika, Mr. Sudarshan, Ms. Vijaya Lakshmi, Mr. Mukunda Reddy, Mr. Srinivas (gaddam) and other non-teaching staff at the School of Physics.

I would like to thank Dr. J. Arout Chelvane and Dr. A. R. James scientists, Defence Metallurgical Research Laboratory, Hyderabad for allowing me to perform magnetic and ferroelectric hysteresis (P−E) loop measurements in their labs, respectively.

A big thanks also go to the lab members Mr. Avisek Das, Mrs. B. Praneetha, Mr. A. Sridhar and Mr. B. Kranthi Kumar and others, infact, their love affection and timely help made me to enjoy in the lab. I am very much appreciate all their cooperation during my study in lab. I express my gratitude to my friends and research scholars at the School of Physics, Mr. Pundareekam, Mr. Mahender, Mr. Rajesh, Mr. Joshi, Mr. Arun, Mr. Pandu Sunil Kumar, Mr. Sandeep Sharma, Mr. Naveen, Mr. Andrews, Dr. Ravibabu and Dr. Byram Chandu.

I thank my family members for their unfailing cooperation and support during my PhD thesis work.

Dedicated

to

Family Members

List of Abbreviations

AFM	Antiferromagnetic
BFO	$BiFeO_3$
BSE	Back scattered electron
BTO	Barium titanate
CCD	Charge coupled device
CFO	Cobalt ferrite
CME	Converse Magnetoelectric
DME	Direct Magnetoelectric
EDXS	Energy dispersive X-ray spectroscopy
EPR	Electron paramagnetic resonance
ESR	Electron spin resonance
FC	Field cooled
FE	Ferroelectric
FESEM	Field emission scanning electron microscopy
FM	Ferro(ferri)magnetic
FW	Field warming
FWHM	Full-width at half-maxima
ICDD	International center for diffraction data
GOF	Goodness of fit
LSMO	$La_{0.67}Sr_{0.33}MnO_3$
ME	Magnetoelectric
M−H	Magnetic hysteresis loop
M−T	Temperature dependent magnetization
NFO	Nickel ferrite
NMR	Nuclear magnetic resonance

List of Abbreviations

P−E	Polarization verses electric field
PE	Paraelectric
PMN-PT	$Pb(Mg_{1/3}Nb_{2/3})O_3$–$PbTiO_3$
PPMS	Physical property measurement system
PZT	$PbZrTiO_3$
SE	Secondary electrons
SNOM	Scanning near field optical microscopy
SSR	Solid state reaction
T_C	Curie temperature
TGA	Thermal gravimetric analysis
VSM	Vibrating sample magnetometer
XRD	X−ray diffraction

List of Figures

1.1 Schematic representation of multiferroics 2
1.2 Schematic representation of magnetic thin film on ferroelectric substrate. 6
1.3 Schematic representation of laminate composites. 6
1.4 Schematic representation of particulate composites formation from individual phases. 7
1.5 Schematic representation of spinel ferrite structure. 10
1.6 Schematic of perovskite (ABO_3) structure. 11
1.7 Schematic representation of structural phase transitions of BTO 11

2.1 Schematic representation of solid-state reaction method. 21
2.2 Photograph of x-ray diffractometer. 23
2.3 Representation of basic principle of field emission scanning electron microscope. 26
2.4 Schematic representation of electron interaction with the atom. 27
2.5 Schematic representation of vibrating sample magnetometer 28
2.6 Photograph of physical property measurement system. 29
2.7 Schematic representation of splitting of spectral line in the presence of magnetic field. 31
2.8 Schematic representation of ESR signal. 32
2.9 Photograph of electron spin resonance spectrometer. 32
2.10 Dielectric constant instrument photograph. 34
2.11 Schematic representation of Raman spectroscopy. 35

3.1 The thermal gravimetric analysis plot of NFO and BTO compounds. . 40
3.2 A flow chart for the preparation of single phase BTO and NFO samples. 41
3.3 A flow chart for the preparation of composite (x)NFO+(1-x) BTO composite materials. 42
3.4 The pellets of NFO−BTO composites for x = 0 to 1, sintered at 1350 °C. 42
3.5 The x-ray diffraction patterns of (a) NFO and (b) BTO annealed at different temperatures 43
3.6 X-ray diffraction patterns of NFO - BTO composite samples. 44
3.7 Typical x-ray diffraction pattern of x = 0.5 composite sample. 45
3.8 The variation of lattice parameters of NFO and BTO phases in composites as a function of NFO content (x). 47

3.9 The variation in tetragonality of BTO phases in composites as a function of NFO content (x). 47
3.10 Volume of BTO and NFO in NFO−BTO composites. 48
3.11 The back scattered scanning electron micrographs of NFO - BTO composite samples for different x (=0-1). The inset shows the grain size distribution histogram and the solid curve represents Gaussian fit to the data. 51
3.12 The average grain size values of NFO and BTO in composites. 52
3.13 The EDXS spectrum of BTO (bright) phase and NFO (dark) phase in the 0.5NFO+0.5BTO composite. 53

4.1 (a) XRD patterns of BTO measured at 150, 230, 300 and 570 K temperatures and (b) enlarged view of the peak present at $2\theta\sim 45^{\circ}$. 56
4.2 The Rietveld refinement XRD patterns of BTO (x = 0) at four different structural phases. 56
4.3 The variation lattice parameters of BTO with respective temperature. . 57
4.4 The XRD patterns of NFO at obtained 150, 230, 300 and 570 K temperatures. 58
4.5 The variation of lattice parameter of NFO with temperature. 59
4.6 The Rietveld refinement patterns of NFO (x = 1) at measured different temperatures. 59
4.7 The XRD patterns of NFO −BTO for x= 0.2, 0.4, 0.6 and 0.8 composites at 150 K, 230 K, 300 K and 570 K temperatures. 60
4.8 Rietveld refined XRD patterns of NFO−BTO for x = 0.2 composite at different temperatures. 61
4.9 The rietveld refined XRD patterns of NFO −BTO for x = 0.4, 0.6 and 0.8 composite at different temperatures. 62
4.10 The schematic representations of possible vibrational Raman modes of atoms in BTO. 65
4.11 The vibrational Raman spectrum of BTO (x = 0) sample at different temperatures and the solid red line represents the deconvoluted specral peaks fitted with Lorentzian curve. 66
4.12 The schematic representation of the possible Raman mode vibrations of single phase NFO 69
4.13 The Raman spectrum of NFO (x = 1) sample at different temperatures and peak fittings are done with Lorentz curve. 70
4.14 Raman spectra of NFO − BTO composites at 150 K, 230 K and 300 K. . 71
4.15 The Raman spectra along with Lorentz fitting of NFO − BTO samples for (a) x = 0.2 and (b) x = 0.8 at different temperatures. 73

5.1 The temperature-dependent magnetization of NFO - BTO composites for different x values. 79

5.2 The temperature-dependent magnetization of NFO−BTO composites for different x values. . . . 81
5.3 The variation of Curie temperature of NFO with x in NFO−BTO composites. . . . 81
5.4 (a-c) Magnetic hysteresis loops of NFO−BTO composites at 300 K, 230 K and 150 K. . . . 83
5.5 (a-c) Variation in the H_C, M_S, M_R with respect to x in NFO-BTO composites. . . . 84
5.6 The magnetic hysteresis loops of NFO sample at 5 K and 300 K. . . . 85
5.7 The variation of magnetic moment with x for NFO-BTO composites at 300 K. . . . 86
5.8 The magnetic hysteresis loops of NFO-BTO composites for different x values at 300 °C. . . . 86
5.9 The variation of remanence magnetization and coercive field values for different x values at 300 °C of NFO-BTO composites. . . . 87
5.10 The electron spin resonance spectra of NFO-BTO composites for different x values. . . . 87
5.11 The variation of g - factor and spin−spin relaxation time values with x of NFO-BTO composites. . . . 89

6.1 The temperature-dependent dielectric constant of single phase BTO measured at 1 kHz frequency. . . . 94
6.2 The temperature-dependent dielectric constant of NFO−BTO composites for x = 0.1 to 1 measured at 1 kHz frequency. . . . 95
6.3 The variation of Curie temperature of NFO−BTO composites with respect to x (NFO content). . . . 95
6.4 The variation of dielectric constant of NFO−BTO composites with NFO content (x) at 1 kHz frequency. . . . 96
6.5 The temperature−dependent dielectric constant of x = 0.2 composite at different frequencies. . . . 97
6.6 The frequency−dependent dielectric constant plots of NFO−BTO composites for x = 0 to 1 at RT, 100, 200, 300 °C, (b) magnified plots of figure (a). . . . 99
6.7 (a) Frequency−dependent dielectric constant of x=0−1 composite samples at resonance (b) Variation in the resonance and dielectric constant of composites with respective x (NFO content). . . . 100
6.8 Variation in the resonance frequency and dielectric constant of NFO−BTO composites with respective temperature. . . . 101
6.9 The variation of dielectric loss with temperature of NFO−BTO composites for x = 0 to 1. . . . 102
6.10 The frequency dependent dielectric loss of the x = 0.0 to 1.0 composites at 30 °C, 100 °C, 200 °C, 300 °C. . . . 103

6.11 The ferroelectric hysteresis loops of NFO−BTO composites for $x = 0$ - 0.3. 104

List of Tables

1.1 Requirements for the magnetoelectric materials 3

2.1 List of frequency, wavelength and magnetic field of various ESR spectrums 30

3.1 Refined crystallographic parameters of single phase (NFO, BTO) and NFO - BTO composite samples. 46
3.2 The phase percentage (P_B,P_N), x-ray density (ρ_{xrd}), experimental density (ρ_{exp}), percentage of density (ρ%) and percentage of porosity (P%) values of NFO - BTO composites for different x values. 49

4.1 The Rietveld refined crystallographic parameters of BTO. 57
4.2 The Rietveld refined crystallographic parameters of NFO sample at different temperatures. 59
4.3 The Rietveld refined crystallographic parameters of NFO $-$BTO composites for x = 0.2, 0.4, 0.6 and 0.8 at different temperatures. 61
4.4 The lattice strain ($\times$ 10^{-4}) values of NFO$-$BTO composites for x = 0, 0.2, 0.4, 0.6, 0.8 and 1 samples at different temperatures, corresponding to different ferroelectric phases of BTO. 63
4.5 The possible Raman mode positions (cm^{-1}) of BTO in NFO$-$BTO composites at different temperatures. 67
4.6 The FWHM (cm^{-1}) of BTO in NFO$-$BTO composites at different temperatures. 68
4.7 The Raman mode position and FWHM of the NFO in NFO$-$BTO composites at different temperatures. 72
4.8 The cation distribution, magnetic moment per formula unit and the effective force constant values for x = 0.8, 0.9 and 1 samples. 75

5.1 The resonance field (H_r), peak to peak line width (ΔH_{pp}) and ratio between positive and negative intensity(A/B) of NFO-BTO composite samples for different x values. 88

Abstract

The thesis entitled "***Structural, magnetic and dielectric properties of $NiFe_2O_4-BaTiO_3$ magnetoelectric multiferroic composites***" presents the experimental research work done during the last five years. It consists of seven chapters viz., ***Introduction***, ***Experimental methods***, ***Preparation and characterization***, ***Structural properties***, ***Magnetic properties***, ***Dielectric properties*** of $NiFe_2O_4-BaTiO_3$ particulate composites and finally the ***Summary and future scope*** of the present research work. The main contents and the discussion pertaining to them are systematically presented in the following paragraphs as chapters wise.

The ***first chapter*** gives an overview of multiferroics focusing on magnetoelectric (ME) phenomena, particularly in ferrite and ferroelectric (FE) materials. The chapter begins with the importance of ME coupling in composites for a fundamental understanding of basic physics. The essential basic information like crystal structure and phase transitions of the single phase materials were presented. This chapter also gives a thorough literature review and the existing gap between the past research and present work. The motivation and main theme of the work were discussed along with the specific objectives of the thesis.

The ***second chapter*** starts with importance of the solid state reaction (SSR) method. The appropriate experimental strategies adopted to fulfill the objectives of the research work were mentioned in the thesis. The phase purity and structural characterization were carried out by x-ray diffraction (XRD) along with rietveld refinement. The microstructural and morphological analysis was done by the field emission scanning electron microscopy (FESEM) in the back scattered electron (BSE) mode. The Archimedes principle was used to determine the density of the samples, and it was explained clearly. The temperature-dependent structural properties of the ferrite−ferroelectric composites were measured by the XRD and Raman spectroscopy. The magnetic properties of the composites were measured by the physical property measurement system (PPMS) in the low-temperature regime ($T < 300$ K) and the vibrating sample magnetometer (VSM) was used in the high-temperature regime ($T > 300$ K). The electron spin resonance (ESR) data were measured for the prepared composites. The dielectric properties, ferroelectric hysteresis loops of the composites were obtained as a function of temperature and frequency. In this chapter, all the working principles of the instruments used in the present work were discussed with schematic diagrams and with photographical pictures.

The ***third chapter*** deals with the preparation of ferrite and ferroelectric individual and composite phases and their characterization. The policrystalline materials of ferrite, $NiFe_2O_4$ (NFO), and ferroelectric, $BaTiO_3$ (BTO) composite pellets were prepared by SSR method by sintering at 1350 °C. The primary structural characterization was done by the XRD; this result confirms single phase formation of individual phases; no third phase was present in the composite samples. The XRD data were analyzed by using Rietveld refinement, and the variation of various crystallographic parameters were discussed. The BSE micrographs show the coexistence of

two phases in composites. The measured density of the samples was found to be approximately 90% with the theoretical density.

The ***fourth chapter*** deals with the XRD and Raman measurements carried out at different temperatures, corresponding to different FE phases of BTO. The BTO exhibits FE to paraelectric phase transition along with structural phase transition at 393 K. Therefore, the Raman and XRD measurements were expected to give significant changes in structural and vibrational modes of the molecules of samples due to strain-mediated ME coupling. Therefore, XRD and Raman measurements were carried out at the four structural phases of the BTO. The temperature-dependent XRD, and Raman measurements enable one to see the variation of crystallographic and vibrational phonon mode parameters as a function of phase content. The results obtained in this chapter indirectly established the strain-mediated ME coupling in NFO−BTO particulate composites. The magnetic moment per formula unit was calculated from the XRD and Raman measurements based on the cation distribution in sample, and it was found to be approximately 2.1 $\mu_B/f.u$. These values matches well with mangetic moment per formula unit calculated from magnetic measurements.

The ***fifth chapter*** deals with the magnetic properties of NFO−BTO composite samples. The temperature-dependent magnetization measurements were done in the low-temperature (100 K - 300 K) range and high-temperature (30 °C - 700 °C) by applying the magnetic field of 250 Oe. In these measurements, the jumps in the temperature-dependent magnetization curves were observed at structural phase transitions of the BTO. It is due to the transferred strain from BTO to NFO across the hetero-grains of NFO-BTO. The Curie temperature of single-phase NFO is found to decrease with an increase of BTO in composites. The magnetic hysteresis loops were measured at four different temperatures corresponding to the different FE phases of BTO. The ESR measurements were measured in the magnetic field range, 0 - 8000 Oe at room temperature. The variations in peak to peak line width, g-factor, peak intensity, and resonance field were observed with respect to composition, and underlying mechanisms were explained.

The ***sixth chapter*** explored the dielectric properties of NFO−BTO composite samples. It describes the variation of dielectric parameters such as dielectric constant, dielectric loss as a function of temperature and frequency. The dielectric constant values were found to be maximum for the samples for equal weight percent of phase contents. It gives an indication that the high ME coupling is possible for maximum interfaced sample. The Curie temperature of BTO was found to increase with increase in NFO content in the composite. The frequency-dependent dielectric constant measurements were done at different temperatures in FE phase and paraelectric phase of BTO. In the frequency-dependent dielectric measurements, the resonance was observed for both single-phase as well as composite samples and data were interpreted. The electric hysteresis loops for some of the samples in the series were measured and underlying physics was discussed.

The final chapter, ***seventh chapter*** of the thesis deals with summary and conclusions made out of the present work. This chapter also presents the future prospects and scope for further investigations in line with the present work.

Contents

1 Introduction **1**
1.1 Multiferroics . . . 1
1.2 Magnetoelectrics . . . 2
1.2.1 Type-I ME multiferroics . . . 3
1.2.1.1 Perovskites (displacement type) . . . 3
1.2.1.2 Perovskites (lone pair type) . . . 4
1.2.1.3 Hexagonal rare earth manganites (geometric type) . . . 4
1.2.1.4 More complex structures . . . 4
1.2.2 Type-II ME multiferroics . . . 4
1.2.2.1 Spiral type . . . 5
1.2.2.2 Collinear type . . . 5
1.2.3 Single-phase magnetoelectrics . . . 5
1.2.4 Two-phase magnetoelectrics . . . 5
1.2.4.1 Thin films . . . 5
1.2.4.2 Laminate composites . . . 6
1.2.4.3 Particulate composites . . . 6
1.3 ME coupling mechanisms . . . 8
1.3.1 Strain-mediated effect . . . 8
1.3.2 Charge-mediated effect . . . 8
1.3.3 Exchange bias-mediated effect . . . 8
1.3.4 Orbital-mediated effect . . . 8
1.4 Applications of ME materials . . . 8
1.4.1 Magnetic memories . . . 9
1.4.2 Random access memories and logic devices . . . 9
1.4.3 Electrically tunable microwave devices . . . 9
1.4.4 Magnetic sensors . . . 9
1.4.5 Energy harvesters and conversion devices . . . 9
1.5 Literature review . . . 10
1.5.1 Ferrites . . . 10
1.5.2 Ferroelectrics . . . 11
1.5.3 Ferrite−ferroelectric MEs . . . 12
1.6 Aim . . . 13
1.7 Objectives . . . 13
1.8 Thesis organization . . . 14

2 Experimental techniques **19**
2.1 Material preparation . . . 19
2.1.1 Solid-state reaction method . . . 19
2.1.2 SSR reaction mechanism . . . 20
2.2 Characterization . . . 21
2.2.1 X-ray diffraction . . . 22
2.2.2 Rietveld refinement . . . 23
2.2.3 Field emission scanning electron microscopy . . . 25
2.2.4 Energy dispersive x-ray spectroscopy . . . 26
2.3 Magnetic Properties . . . 27
2.3.1 Vibrating sample magnetometer . . . 27
2.3.2 Physical properties measurement system . . . 29
2.3.3 Electron spin resonance . . . 30
2.3.3.1. Origin of the ESR signal . . . 30
2.4 Dielectric properties . . . 33
2.5 Raman Spectroscopy . . . 34
2.6 Ferroelectric properties . . . 36

3 Preparation and characterization of NFO−BTO composites **39**
3.1 Sample preparation . . . 39
3.2 X-ray diffraction . . . 42
3.2.1 Rietveld Refinement . . . 45
3.2.2 Lattice parameters . . . 47
3.2.3 Phase percentage . . . 48
3.3 Density . . . 49
3.3.1 The theoretical x-ray density . . . 49
3.3.2 The experimental (bulk) density . . . 49
3.3.3 The percentage of density . . . 50
3.3.4 The percentage of the porosity . . . 50
3.4 Scanning electron microscopy analysis . . . 50
3.4.1 Energy dispersive x-ray analysis . . . 52
3.5 Chapter summary . . . 53

4 Structural properties of NFO−BTO composites **55**
4.1 Temperature-dependent x-ray diffraction . . . 55
4.1.1 $BaTiO_3$ . . . 55
4.1.2 $NiFe_2O_4$ . . . 58
4.1.3 $BaTiO_3 - NiFe_2O_4$ composites . . . 60
4.1.4 Lattice strain . . . 63
4.1.5 Cation distribution . . . 63
4.2 Raman spectroscopy . . . 65
4.2.1 $BaTiO_3$ . . . 65
4.2.2 $NiFe_2O_4$ . . . 69

4.2.3 $BaTiO_3 - NiFe_2O_4$ composites . . . 70
4.2.4 Cation distribution . . . 73
4.3 Chapter summary . . . 75

5 Magnetic properties of NFO−BTO composites 78
5.1 Temperature dependent magnetization . . . 78
5.1.1 Low-temperature regime (100 < T < 330 K) . . . 78
5.1.2 High-temperature regime (30 < T < 700 °C) . . . 80
5.2 Magnetic hysteresis loops . . . 82
5.2.1 Low-temperature regime (100 < T < 330 K) . . . 82
5.2.2 High-temperature regime (30 < T< 700 °C) . . . 86
5.3 Electron spin resonance . . . 87
5.4 Chapter summary . . . 90

6 Dielectric properties of NFO−BTO composites 93
6.1 Dielectric constant . . . 93
6.1.1 Temperature-dependent dielectric constant ($BaTiO_3$) . . . 93
6.1.2 Temperature dependent dielectric constant (NFO−BTO composites) . . . 94
6.1.3 Dielectric constant of NFO−BTO composites at different frequencies . . . 96
6.1.4 Frequency−dependent dielectric constant . . . 97
6.2 Dielectric loss . . . 101
6.2.1 Temperature-dependent dielectric loss . . . 101
6.2.2 Frequency-dependent dielectric loss . . . 102
6.3 Ferroelectic hysteresis loops . . . 103
6.4 Chapter summary . . . 104

7 Summary and future scope 107
7.1 Summary . . . 107
7.2 Future scope . . . 109

Chapter 1

Introduction

1.1 Multiferroics

The multifunctional materials are having a huge demand for various device applications for the ongoing technology, such as memory devices, magnetic sensors, tunable electronic devices, resonators, filters, transformers, and gyrators [1]. The functional materials such as ferroelectric (FE), ferromagnetic (FM), ferrotoroidic, and ferroelastic with their spontaneous order parameters i.e., spontaneous "polarization", "magnetization", "toroidicity", and "elasticity", respectively, are of current interest in the field. However, if the material or the material system exhibit two or more ferroic orders in it and if it becomes possible to manipulate these order parameters by their cross-coupled fields, then the material or material system is said to be a multiferroic material or multiferroic material system [1]. As per this definition, if the material exhibits spontaneous "polarization" and "magnetization" simultaneously and manipulation of these order parameters viz., the electric "polarization" by an applied magnetic field and the "magnetization" by an applied electric field, then such materials are said to be the magnetoelectric (ME) material and the phenomena associated with these manipulations are called "direct magnetoelectric" (DME) and "converse magnetoelectric" (CME) effects, respectively [2]. Similarly, one can discuss the relations between magnetic and elastic, electric and elastic parameters, and associated phenomena. Due to the unavailability of spontaneous "elasticity" in many materials, the research on the material is very much limited. The order parameters, field combinations, and associated phenomena of multiferroics are schematically shown in Fig. 1.1. In view of the wide range of applications due to the availability of a variety of room temperature FE and FM materials, the research on the ME materials has flourished a lot. The origin of ME multiferroics has been presented here in the following sections.

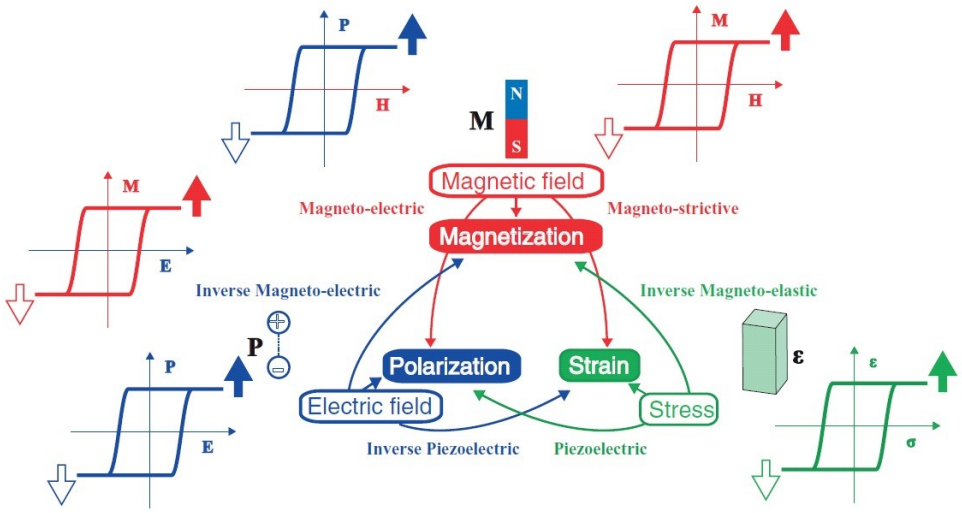

FIGURE 1.1: Schematic representation of multiferroics, reprinted from [3] (2015, Institute of Physics).

1.2 Magnetoelectrics

As discussed in the previous section, the MEs are the subclass of multiferroics. The free energy equation can explain the origin of the effect for a given ME system, [4, 5],

$$F(E,H) = F_o - P_i^s.E_i - M_i^s.H_i - \frac{1}{2}\epsilon_o\epsilon_{ij}E_iE_j - \frac{1}{2}\mu_o\mu_{ij}H_iH_j - \alpha_{ij}E_iH_j - ... \tag{1.1}$$

where, F_0 is the ground state free energy, P^s and M^s are the saturation "polarization" and "magnetization", respectively. The H and E are the magnetic and electric fields. The ϵ , μ, and α are the "permittivity", "permeability", and "ME coupling coefficient", respectively. The partial differentiation of F with respect to electric field gives the "polarization", and similarly, the partial differentiation of F with respect to magnetic field gives the "magnetization", as given below,

$$-\frac{\partial F}{\partial E_i} = P_i^s + \frac{1}{2}\epsilon_o\epsilon_{ij}E_j + \alpha_{ij}H_j + ... \tag{1.2}$$

$$P = P_i^s + \frac{1}{2}\epsilon_o\epsilon_{ij}E_j + \alpha_{ij}H_j + ... \tag{1.3}$$

$$-\frac{\partial F}{\partial H_i} = M_i^s + \frac{1}{2}\mu_o\mu_{ij}H_j + \alpha_{ij}E_i + ... \tag{1.4}$$

$$M = M_i^s + \frac{1}{2}\mu_o\mu_{ij}H_j + \alpha_{ij}E_i + ... \tag{1.5}$$

In the above partial derivative equations of free energy concerning electric and magnetic fields, particularly the third term, gives an impression that both DME and CME coefficients can be easily obtained. The partial derivative of "polarization" with respect to magnetic field provides the ME with a coupling coefficient, which quantifies

the DME coupling effect. Similarly, the coefficient which originates due to the partial derivative of the magnetization with respect to electric field quantifies the CME effect.

$$\frac{\partial P}{\partial H} = \alpha_{DME} \tag{1.6}$$

$$\frac{\partial M}{\partial E} = \alpha_{CME} \tag{1.7}$$

Therefore, from the above equations, the applied magnetic field can manipulate polarization, and the magnetization can be changed by the applied electric field.

Based on the above discussion, it is understood that the ME phenomena can be observed only when material exhibits spontaneous order parameters. Therefore, the material must be at least ferro(ferri) magnetic (FM) and FE in nature in the detectable range of temperature with reasonable coupling between these order parameters. In general, the individual FM and FE materials should possess the following requirements, as given in Table 1.1 [6].

TABLE 1.1: Requirements for the magnetoelectric materials

	Requirements	Ferromagnetism	Ferroelectricity
1	*d* orbital	partially filled	fully filled or empty
2	symmetry breaking	time reversal	space inversion
3	conductivity	metallic	insulating

However, to obtain a reasonably good value of the ME coefficient, the material should have reasonable high electric and magnetic susceptibilities.

There exist two types of ME multiferroics based on the underlying mechanism responsible for ME coupling; viz., (1) Type-I multiferroics (2) Type-II multiferroics [7].

1.2.1 Type-I ME multiferroics

Suppose the FE and magnetic order parameters are originated from two distinct sublattices or different regions of the lattice. Such type of ME multiferroic materials comes under the category of type-I ME multiferroics. The ferroelectricity breaks the "spatial-inversion" symmetry in these materials. Similarly, the ferromagnetism breaks the "time-reversal" symmetry. Since the different order parameters originate from different sub-lattices, the ME coupling is feeble in type-I multiferroics [8].

1.2.1.1 Perovskites (displacement type)

The materials with perovskite-type structure with compositional formula, $A(B^{'}B^{''})O_3$ will come under this category. Here, "polarization" originates from the $B^{'}$-sublattice, and $B^{''}$-sublattice is responsible for magnetic order. In general, this type of materials

will be synthesized by the substitution of FM ion in the FE lattice. The example for this type of materials are: $PbFe_{1/2}Nb_{1/2}O_3$ and $PbFe_{1/2}Ta_{1/2}O_3$ [9].

1.2.1.2 Perovskites (lone pair type)

The perovskite materials have the compositional formula, ABO_3, here, B is the magnetic atom, and A contains the electron pair in outer "*s*-orbital", which is not a part of the bond formation (lone pair). Interestingly, these electrons polarize easily. The ferroelectricity is produced by theses polarized "*s*-electrons" and the ferromagnetism by the magnetic ion with partly filled "*d*-orbitals". For example, Bismuth and Lead-based perovskites, in addition to $BiFeO_3$ (BFO) [10, 11].

1.2.1.3 Hexagonal rare earth manganites (geometric type)

This type of ME multiferroics are the hexagonal "manganites" with compositional formula, $RMnO_3$, where R is a "rare-earth element" [12]. The magnetism in these materials arises due to the Mn ion, and the ferroelectricity is caused by the geometrical distortion of the Oxygen octahedra. The examples of these types are $YMnO_3$ and $HoMnO_3$. The ME coupling between two hetero-domains is found in $YMnO_3$ [13]. Interestingly, the FM behavior in $HoMnO_3$ was shown to be switchable reversely "on" and "off" by an applied electric field [14].

1.2.1.4 More complex structures

In some materials, magnetic ordering is due to magnetic ion, and ferroelectricity is due to the rest of the ion complex in the lattice. The examples include "boracites", $M_3B_7O_{13}X$, here, M is the "transition metal" and X = Cl, Br, I [15, 16]. The "boracites" are FE antiferromagnets, in which the magnetism originates from the "transitional metal" atoms and the "polarization" from the "X-O-octahedron". The "fluorites" of $BaMF_4$, where M is a "transition metal", also shows cooccurring FE and antiferromagnetic (AFM) [17, 18].

1.2.2 Type-II ME multiferroics

The type-II category of materials were discovered recently, in which the "magnetic ordering" breaks both the "spatial" and "time inversion" symmetries. In these multiferroics, the applied magnetic field induces the ferroelectricity, and hence the ME coupling, certainly bigger than type$-$I materials [19] . A serious issue of this class of ME multiferroics is that the minimal polarization compared with many established FEs.

1.2.2.1 Spiral type

The materials with compositional formula, $TbMnO_3$ or $TbMn_2O_5$; the ground magnetic state is due to long-range "spiral" ordering [20, 21]. In this type, the "polarization" arises in conjunction with the magnetic phase owing to the "spin–orbit interaction", given by $\tau = r_{ij} \times (s_i \times s_j)$, here, r_{ij} is a vector joining the adjacent spins s_i and s_j [22, 23]. This process allows the "polarization" to rotate by 90° in $TbMnO_3$ and changes its sign in an applied magnetic field, in a certain direction [20, 21] .

1.2.2.2 Collinear type

When two different magnetic atoms are coupled with exchange coupling, the "polarization" may originate in the material. Such a type of materials come under collinear type multiferroics. Example: Ca_3CoMnO_6. In this compound, the exchange occurs along 1-D links of Co and Mn atoms [24]. The magnetic ordering deforms the bonds by breaking the "space inversion" and allows the "polarization" to emerge [6, 7].

1.2.3 Single-phase magnetoelectrics

If a single material consists of two or more ferroic orders, then it is called single-phase multiferroic. In these materials, the magnetic and electric order parameters are inherently coupled and exhibit the ME effect intrinsically. It is very difficult to realize the two ferroic orders simultaneously in materials due to their contradictory properties, as given in Table 1.1. However, there are few single-phase multiferroics available, for example: $Mg_3B_7O_{13}Cl$, Cr_2O_3, $BiFeO_3$, $TbMnO_3$, $TbMn_2O_5$, $YMnO_3$, $LuFe_2O_4$, $HoMnO_3$ and $DyFeO_3$. In these materials, some of them were discovered naturally, and some are synthesized artificially [6]. In these single-phase multiferroics, the ME coupling is very weak and confined to much below room temperature.

1.2.4 Two-phase magnetoelectrics

When a tailor-made material system with two different materials with ferroic order without any chemical reaction becomes possible, the material system comes under the two-phase multiferroic systems. It is necessary to prepare two-phase multiferroics for the improved ME coupling when compared to single-phase multiferroics. These two-phase multiferroics can be prepared in different forms; thin films, laminate composites, and particulate composites. The responsible ME coupling between the FM and FE phases with suitable examples are presented here.

1.2.4.1 Thin films

A thin FM layer is to be deposited on the thicker FE substrate/thin film in the present context. The schematic representation of a thin film is shown in Fig. 1.2. In this case, the FM and FE interface becomes crucial in obtaining the required ME effect. Principally, there exist three mechanisms taking place at the interface, viz., (a)

"charge-mediated" ME coupling, (b) "strain-mediated" ME coupling, and (c) "orbital-mediated" ME coupling. These mechanisms depend on the probe's location and the thickness of the film deposited on the FE substrates. The thin-film optimization is crucial in this case, and sample preparation is expensive and challenging. Although several connectivities are possible, the 2-2 connectivity is prominent in these material structures.

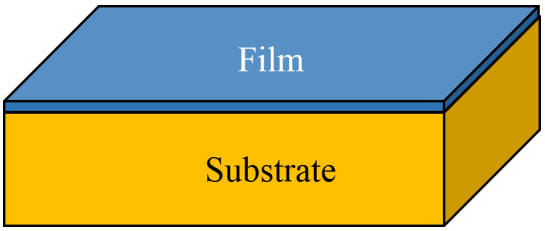

FIGURE 1.2: Schematic representation of magnetic thin film on ferroelectric substrate.

1.2.4.2 Laminate composites

The laminate composites are the bulk amount of layers attaching with a suitable chemical binder. The schematic diagram of laminate composites is shown in Fig. 1.3. The binder is designed to carry the strain efficiently from one layer to the other. The best-laminates available today are the strong "piezoelectric" materials such as $Pb(Zr,Ti)O_3$ and "magnetostrictive" materials such as ferrites ($NiFe_2O_4$), alloys ($TbDyFe_2$ (Terfenol-D)) [25, 26, 27]. These laminates are having 2-2 connectivity in between ferrite and FE materials. The proper connectivity between the two material laminates is challenging in the case.

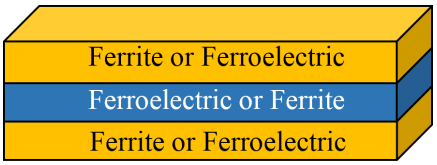

FIGURE 1.3: Schematic representation of laminate composites, modified after [28] (2008, American Ceramic Society).

1.2.4.3 Particulate composites

The particulate composites are the two hetero−ferroic powders, which are physically mixed. A schematic representation of particulate composite is shown in Fig. 1.4. In particulate composites, 0-3 connectivity exists between magnetic and electric phase. It also depends on the preparation techniques. The particulate composites have several advantages, such as their economic viability and technical feasibility. It does not require sophisticated equipment and does not involve any complex procedure to produce the sample materials. Remarkably, in particulate composites, one

can have the freedom to select the starting particle size and the processing parameters. Moreover, these composites can be sintered in an open air atmosphere. Additionally, it allows for combining the different crystal structures [1]. With a view to obtain the promising ME coupling between the FM and FE phases, the following conditions need to be ensured during the preparation [29].

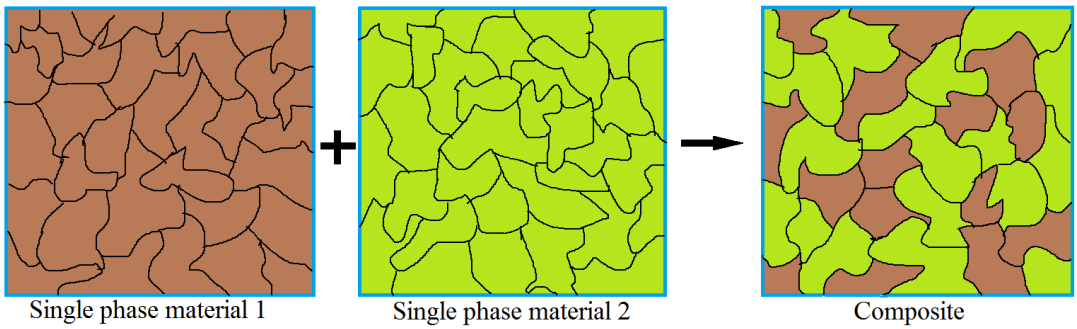

FIGURE 1.4: Schematic representation of particulate composites formation from individual phases, modified after [30] (2005, Springer).

- Individually, the FE and FM materials should in a single phase.
- The mixed single-phase materials should not react chemically in composites.
- There should not be any dead layer (either crystalline or amorphous form) between the grains of two single-phase materials.
- The contact interface between the hetero-grains should be as high as possible.
- The magnetic material should posses a high "magnetostriction" and high "permeability".
- Similarly, the FE material should have a high "dielectric constant" and high "piezoelectric coefficient".
- Finally, the FM and FE materials should have minimum lattice mismatch at heterograin interface.

1.3 ME coupling mechanisms

1.3.1 Strain-mediated effect

A widely observed phenomenon by transferring the strain across FM/FE bilayer interface and causes a significant change in the FM's magnetic properties. In this case, the strain generation in FE material is due to the "inverse piezoelectric effect" either by the electric field or by the FE material's structural phase transition. The strain-mediated ME coupling was commonly detected in thin films [2, 31, 32, 33]. In the particulate composites, this effect is rarely observed, i.e., the strain-mediated ME coupling phenomena [34], it is possible only with high-quality single-phase materials in composites without reaction between them, and there should not be any dead layer in between these single-phase materials.

1.3.2 Charge-mediated effect

An electric field could cause the aggregation of charges at the hetero-interface, which produces a change in (interface) magnetization. The charge-mediated ME coupling has the advantage of a manganite based ultrathin film for competing electronic ground states. The charge mediated ME was demonstrated in $Fe_3O_4/BaTiO_3$ (BTO), and $La_{0.67}Sr_{0.33}MnO_3$ (LSMO) /$PbZrTiO_3$ (PZT) thin films [35, 36].

1.3.3 Exchange bias-mediated effect

This effect ensures the exchange bias between the uncompensated interfacial AFM spins and the spins of the FM layer. This was employed for voltage controlled magnetism in thin films. The utilization of this effect in the multiferroic ME composite nanostructures are derived from single-phase MEs. The exchange bias-mediated ME coupling was demonstrated in permalloy/BFO, LSMO/BFO [37, 38].

1.3.4 Orbital-mediated effect

The external applied electric field changes the interfacial orbital occupancy; ultimately, ME material's magnetization will be changed. Hence, it is said to be an orbital-mediated ME coupling effect. This effect was rarely observed, and it is dominated by the major strain-mediated, charge-mediated exchange-bias mediated mechanisms. For example, in the LSMO/BTO heterostructural thin films, interfacial orbital occupancy was partially changed by the applying electric field, and resultant variation in the magnetization was observed [39, 40].

1.4 Applications of ME materials

Although the mechanism behind the ME coupling and the coupling schemes between the different ferroics are of primal importance, the recent flooded interest in

ME materials on account of the hope they hold for various device applications are also equally important. These promising applications are based on their intriguing physical properties for the present and future technology and are listed below [41].

1.4.1 Magnetic memories

The magnetization switching of the magnetic material with applying the electric field is useful in ME devices. In general, the magnetic medium storage device uses the magnetic field to write the data with two orientations of magnetization ($\pm$M), in the form of "0" and "1" bits. The high coercivity (hard) magnetic materials are required to write the data. However, the high coercivity materials will consume high power and low writing speed. Therefore, the ME material gives an opportunity to avoid this, i.e., the data will be written "electrically" and read "magnetically" [42, 43].

1.4.2 Random access memories and logic devices

In ME multiferroics, "polarization" and "magnetization" are used to store the data in the form of binary digits as "ferroelectric random access memories" and "magnetic random access memories", respectively. If "polarization" and "magnetization" are together used to store the data, then it is called ME random access memory, i.e., it is a four-state logic device. These devices will work with magnetization switching in 90° and 180°. Therefore, the logic gates (AND, NOR, OR, NAND, etc.) could be performed based on ME materials [44].

1.4.3 Electrically tunable microwave devices

The magnetic bias fields are used to tune the magnetization for microwave magnetic devices. The ME coupling shows excellent hope in achieving electrically controlled magnetization and it has resulted in entirely new devices such as "filters", "resonators", and "phase shifters" based on the ME composite films [45, 46].

1.4.4 Magnetic sensors

The ultra-sensitive magnetic field sensors can be devised by employing the ME composites having high ME coefficients. The magnetic sensors are low-cost than superconducting quantum interface devices. These sensors are used to sense the AC and DC magnetic fields. These sensors depend on the signal to noise ratio, i.e., electric noise, vibrating noise, and thermal noise [47].

1.4.5 Energy harvesters and conversion devices

The ME material can be used as an energy harvester for developing electricity from weak energies. In the harvesters, available sources will be used to produce the required energy. The energy harvesting devices based on ME should have sufficient

robustness to accept prolonged exposure to different environments and also to have a wide range of dynamic sensitivity [48, 49, 50].

1.5 Literature review

1.5.1 Ferrites

The ferrites are ceramic ferrimagnetic materials having spinel structure with compositional formula AFe_2O_4; here A is Fe, Ni, Co, Zn, etc. The spinel structure of ferrite with octahedral and tetrahedral site occupancy is shown in Fig. 1.5. The first ferrite ($FeFe_2O_4$) was invented in the year 1930 [51], later many ferrites with compositions, $NiFe_2O_4$ (NFO), $ZnFe_2O_4$, $MnFe_2O_4$ and $CoFe_2O_4$ (CFO) etc. were discovered. These ferrites were explored in thin-film, nanoparticles, core-shell structure, laminate composites, particulate composites, etc. Based on these ferrites' coercivity, they were classified into two classes, viz., soft-ferrites and hard-ferrites [52]. The hard-ferrites are alternatives for permanent magnets because of the difficulty in demagnetizing them. The hard-ferrite materials have applications in refrigerators, loudspeakers, and electric motors, etc. The best example for the semi-hard ferrites is CFO. Similarly, the ferrites with magnetic coercivity less than 50 Oe come under the soft-ferrites category. The examples are NFO, $ZnFe_2O_4$, $MnFe_2O_4$, and $FeFe_2O_4$. The soft-ferrites have applications in inductors, antennas, transformers, etc.

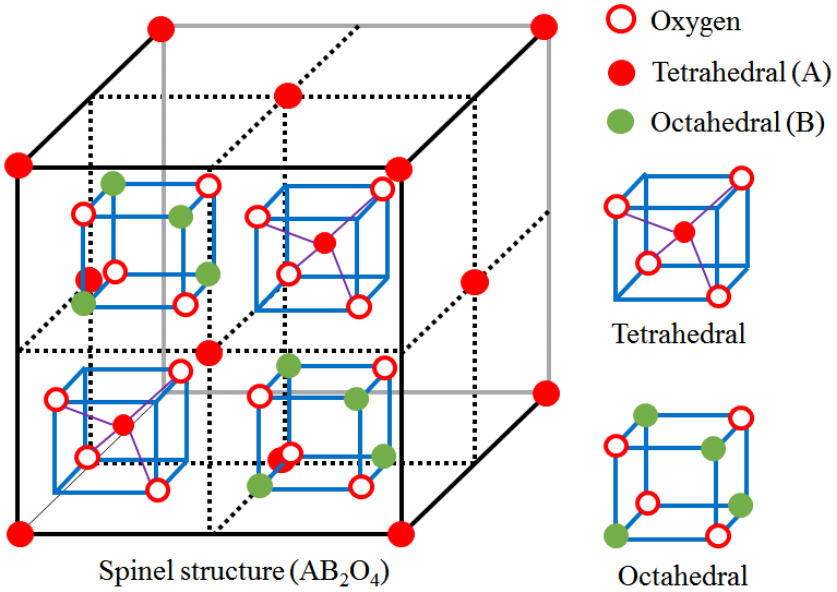

FIGURE 1.5: Schematic representation of spinel ferrite structure, reprinted from [53] (2020, Elsevier).

Among all room-temperature ferrimagnetic oxide materials, Nickel ferrite (NFO) is the most appropriate material to consider one of the constituent phases in two-phase ME composite. The NFO shows room-temperature ferrimagnetism with an inverse spinel structure. The Curie temperature of the NFO is about 870 K [54]. In

addition, the NFO is soft magnetic material having high "permeability" ($\mu_r = 20$) and reasonable "magnetostriction coefficient" (27 ppm), which are essential requirements for promising ME coupling in two-phase ME multiferroics [28].

1.5.2 Ferroelectrics

The phenomenon of ferroelectricity was discovered in 1920 [55]. The ferroelectricity is a characteristic feature of certain materials that have a spontaneous "polarization", and it can be switched by the application of electric field. The BTO and PZT are the well known FE materials. Also, the dopants in BTO and PZT at A and B sites resulted several perovskite-based FE structures [56]. These FEs have applications in capacitors, batteries, sensors, etc. [57].

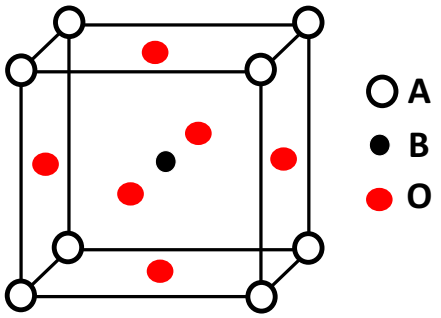

FIGURE 1.6: Schematic of perovskite (ABO_3) structure.

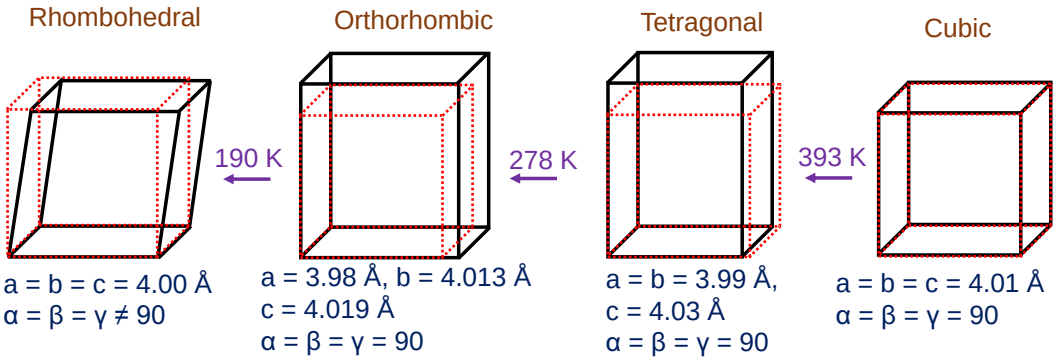

FIGURE 1.7: Schematic representation of structural phase transitions of BTO, modified after [58] (2019, Springer)

.

Among all the existing FEs, the BTO is well known and established FE material, and it is having a perovskite (ABO_3) structure, in which A is at the corners with "divalent cation", B is at the center of the unit cell with "tetravalent cation" and "oxygen" (O) will be at the faces of the unit cell in the perovskite structure. The schematic representation of perovskite is shown in Fig. 1.6. Most importantly, the BTO has structural phase transitions from "rhombohedral" to "orthorhombic" to "tetragonal" to "cubic" structures at temperatures 190 K, 278 K, and 393 K, respectively. The schematic representations of these structures are shown in Fig. 1.7.

While changing "tetragonal" to "cubic" structure, the materials undergo the FE phase changing to the paraelectric phase at 393 K. The BTO exhibits a high dielectric constant (i.e., ϵ =1200), which is very much useful in charge storage capacitors or power storage battery applications. The BTO has a reasonable "piezoelectric" coefficient of 191 pC/N. It is having saturation "polarization" of 26 $\mu C/cm^2$ [28]. These intriguing properties makes BTO one of the suitable constituent phases for ME multiferroic composites.

1.5.3 Ferrite−ferroelectric MEs

The research on multiferroics materials is an ongoing process for more than a decade, mainly in the ME materials, which was a sub-class of multiferroics. Among all other forms of ME multiferroic materials, thin films prominently show ME behavior. In the LSMO/PZT thin films, ME coupling was observed via charge-mediated mechanism [35]. In the LSMO /BFO thin films, ME coupling was observed via the exchange bias-mediated mechanism [37]. In the Fe_3O_4/$Pb(Mg_{1/3}Nb_{2/3})O_3$-$PbTiO_3$ (PMN-PT), thin-films ME coupling was observed via strain-mediated mechanism [45]. The magnetoelastic coupling with different underlying mechanism was observed in Fe_3O_4 /BTO, CFO/BTO thin films [36, 59]. In Fe_3O_4/BTO core-shell nano particles were explored for magnetoelastic coupling [60]. Also, CFO/BTO core-shell structure were presented with underlying mechanism [61]. Several reviews were reported on the underlying mechanisms of these ME multiferroics by several authors for the last couple of years [3, 35, 37, 38, 45, 62, 63].

It has been found from the reported literature from various sources that the different authors have explored the ME coupling by different physical properties. For example, Umashankar et al., have used Raman data to explore the ME coupling in NFO−BTO nano composites [64]. Similarly, Gorige et al., have used magnetization and microstructure analysis to demonstrate ME coupling in NFO−BTO multiferroic composites [65]. Manjusha et al., have reported strain mediated ME coupling in $Bi_{0.5}Na_{0.5}TiO_3$ - $MgFe_2O_4$ multiferroic composites by measuring the dielectric constant and ME coupling coefficient [66]. The ME coupling was also established by measuring piezoelectric resonance in NFO−PZT and CFO $-Pb_{0.988}(Zr_{0.52}Ti_{0.48})_{0.976}$ $Nb_{0.024}O_3$ composites [67, 68]. Ting et al, have measured electron spin resonance in Polyaniline − $BaFe_{12}O_9$ [69]. The core-shell structures of NFO−BTO composites were studied by analyzing the magnetic, dielectric, and ME coupling coefficient. In this case, the analysis was done by varying the NFO content in the composites [70]. The magnetic and dielectric studies were performed on the NFO−BTO multiferroic composites [71]. The effect of the FE phase on magnetic properties and vice versa were studied on NFO−BTO particulate materials and established the strain-mediated ME coupling [72]. The strain-induced ME coupling was also manifested by Tian et al., in magnetite and BTO thin films by measuring the temperature-dependent magnetic measurements [73].

Among all the fore-mentioned, FM materials and FEs, the ferrimagnetic CFO, NFO and FE BTO, PZT are well known parent compounds. Of course, many other elemental substitutions were also used for composites. While the "magnetostriction" of CFO is higher than that of NFO, the composites having magnetically hard CFO show a weak strain-mediated ME coupling, due to high magnetocrystalline anisotropy of CFO. Some times, the slight interface diffusion between ferrite and PZT is one of the possible reason to weaken the ME coupling [67]. Therefore, compared to CFO, NFO is much better to see substantial changes in magnetic properties in ME composites due to the strain changes in ferroelectric phase. Additionally, the BTO is better room-temperature FE compared to PZT. The PZT is having a lead (toxic element) in it. Most importantly, among the available reports on NFO−BTO particulate composites, no clear demonstration of strain-mediated ME coupling in bulk particulate composites was established yet. It has been felt that there is a need to explore the ME phenomena by studying the physical properties of NFO−BTO particulate composites. A comprehensive study on NFO−BTO bulk particulate ME composites was undertaken in the present thesis.

1.6 Aim

The present thesis's main aim is to establish the strain-mediated ME coupling by measuring the structural, magnetic, electric, and dielectric properties. The measurements were performed as a function of temperature, phase content, frequency, etc. to ensure the different strain states of FE material and corresponding physical properties changes in magnetic phase. With a view to realizing this aim, the specific objectives are mentioned below.

1.7 Objectives

- To prepare the high-quality ferrite−FE composites without any inter-diffusion between these phases.
- To understand the ME coupling via temperature-dependent Raman and x-ray diffraction (XRD) measurements.
- To study the magnetic properties of composites in different FE phases of BTO and observe the substantial changes in NFO that are driven by strain.
- To explore the magnetic phase's effect on FE material by evaluating the dielectric properties by varying the temperature, frequency, and composition.
- Finally, to correlate the structure and physical property relations in the context of ME coupling in ferrite−FE composites.

These specific objectives were systematically implemented by considering a strategic work plan and suitable equipment. The obtained results were thoroughly analyzed and interpreted appropriately, as described below.

1.8 Thesis organization

- The **first chapter** deals with the introduction, different types, and applications of ME multiferroics. A thorough literature survey on ME materials and the gap between the present work and reported literature was given. The theme of the research work, along with specific objectives of the thesis was mentioned.
- In the **second chapter**, the working principles of experimental techniques and mechanisms responsible for particular measurement protocols were presented.
- The **third chapter** deals with the preparation procedure, structural and morphological analysis of the prepared samples for the present work.
- The **fourth chapter** addresses the temperature-dependent XRD and Raman data analysis in different structural/FE phases of the FE material. A clear correlation of structural and spectroscopic properties with magnetic properties was established.
- The **fifth chapter,** explains the magnetic properties of samples as a function of temperature and magnetic field. This chapter is crucial in the thesis to establish the strain mediated ME coupling between NFO and BTO particulate composite.
- In the **sixth chapter**, the dielectric properties of the samples with varying temperature and frequency were explored. This chapter also presents the FE hysteresis loops as a function of NFO content.
- Finally, the **seventh chapter** presents the summary of the thesis along with the future scope.

Bibliography

[1] C. W. Nan, M. I. Bichurin, S. Dong, D. Viehland and G. Srinivasan, J. Appl. Phys. **103**, 031101 (2008).

[2] W. Eerenstain, N. D. Mathur and J. F. Scott, Nature **442**, 759 (2006).

[3] T. Taniyama, J. Phys: Condens. Matter **27**, 504001 (2015).

[4] K. F. Wang, J. M. Liu and Z. F. Ren, Adv. Phys. **58**, 321 (2009).

[5] C. A. F. Vaz, J. Hoffman, C. H. Ahn and R. Ramesh, Adv. Mater. **22**, 2900 (2010).

[6] D. Khomskii, Phys. **2**, 20 (2009).

[7] J. P. Velev, S. S. Jaswal and E. Y. Tsymbal, Phil. Trans. R. Soc. A **369**, 3069 (2011).

[8] B. B. Van Aken and T. T. M. Palstra, Phys. Rev. B **69**, 134113 (2004).

[9] G. A. Smolenskii and I. E. Chupis, Sov. Phys. Usp. **25**, 475 (1982).

[10] S. V. Kiselev, R. P. Ozerov and G. S. Zhdanov, Sov. Phys. Dokl. **7**, 742 (1963).

[11] J. R. Teague, R. Gerson and W. J. James, Solid State Commun. **8**, 1073 (1970).

[12] H. L. Yakel, W. C. Koehler, E. F. Bertaut and E. F. Forrat, Acta Crystallogr. **16**, 957 (1963).

[13] M. Fiebig, T. Lottermoser, D. Frohlich, A. V. Goltsev and R. V. Pisarev, Nature **419**, 818 (2002).

[14] T. Lottermoser, T. Lonkai, U. Amann, D. Hohlwein, J. Ihringer and M. Fiebig, Nature **430,** 541 (2004).

[15] E. Ascher, H. Schmid and D. Tar, Solid State Commun. **2**, 45 (1964).

[16] H. Schmid, H. Rieder and E. Ascher, Solid State Commun. **3**, 327 (1965).

[17] M. Eibschutz and H. J. Guggenheim, Solid State Commun. **6**, 737 (1968).

[18] J. F. Scott, Ferroelectrics **24**, 127 (1980).

[19] T. Kimura, Annu. Rev. Mater. Res. **37**, 387 (2007).

[20] T. Kimura, T. Goto, H. Shintani, K. Ishizaka, T. Arima and Y. Tokura, Nature **426**, 55 (2003).

[21] N. Hur, S. Park, P. A. Sharma, J. S. Ahn, S. Guha and S. W. Cheong, Nature **429**, 392 (2004).

[22] H. Katsura, N. Nagaosa and A. V. Balatsky, Phys. Rev. Lett. **95**, 057205 (2005).

[23] M. Mostovoy, Phys. Rev. Lett. **96**, 067601 (2006).

[24] Y. J. Choi, H. T. Yi, S. Lee, Q. Huang, V. Kiryukhin and S. W. Cheong, Phys. Rev. Lett. **100**, 047601 (2008).

[25] G. Srinivasan, E. T. Rasmussen, B. J. Levin and R. Hayes, Phys. Rev. B **65**, 134402 (2002).

[26] J. Ryu, A. V. Carazo, K. Uchino and H. E. Kim, Jpn. J. Appl. Phys. **40**, 4948 (2001).

[27] J. Y. Zhai, Z. Xing, S. X. Dong,J. F. Li and D. Viehland, Appl. Phys. Lett. **88**, 062510 (2006).

[28] J. Zhai, Z. Xing, S. Dong, J. Li, and D. Viehland, J. Am. Ceram. Soc., **91**, 351 (2008).

[29] S. Priya, R. Islam, S. Dong and D. Viehland, J. Electroceramics **19**, 147 (2007).

[30] R. M. German, Powder metallurgy and particulate materials processing, 2005.

[31] C. Thiele, K. Dorr, O. Bilani, J. Rodel and L. Schultz , Phys. Rev. B **75**, 054408 (2007).

[32] J. J. Yang, Y. G. Zhao, H. F. Tian, L. B. Luo, H. Y. Zhang, Y. J. He and H. S. Luo, Appl. Phys. Lett. **94**, 212504 (2009).

[33] J. W. Lee, S. C. Shin and S. K. Kim , Appl. Phys. Lett. **82**, 2458 (2003).

[34] P. Bongurala and V. Gorige, J. Magn. Magn. Mater. **477**, 350 (2019).

[35] C. A. F. Vaz, J. Hoffman, Y. Segal, J. W. Reiner, R. D. Grober, Z. Zhang, C. H. Ahn and F. J. Walker, Phys. Rev. Lett. **104**, 127202 (2010).

[36] M. K. Niranjan, J. P. Velev , C. G. Duan , S. S. Jaswal and E. Y. Tsymbal , Phys. Rev. B **78** , 104405 (2008).

[37] S. M. Wu, S. A. Cybart, P. Yu, M. D. Rossell, J. X. Zhang, R. Ramesh and R. C. Dynes, Nat. Mater. **9**, 756 (2010).

[38] D. Lebeugle, A. Mougin, M. Viret, D. Colson and L. Ranno, Phys. Rev. Lett. **103**, 257601 (2009).

[39] C. Liu, W. H. Wan, S. Gong, H. Zhang and W. Guo, Sci. Rep. **7**, 3856 (2017).

[40] B. Cui, C. Song, H. Mao, H. Wu, F. Li, J. Peng, G. Wang, F. Zeng and F. Pan, Adv. Mater. **27**, 6651 (2015).

[41] J. Ma, J. Hu, Z. Li and C. W. Nan, Adv. Mater. **23,** 1062 (2011).

[42] S. X. Wang and A. M. Taratorin, Magnetic Information Storage Technology, Academic Press , New York (1999).

[43] S. Parkin, X. Jiang, C. Kaiser, A. Panchula, K. Roche and M. Samant, Proceeding of IEEE, **91**, 661 (2003).

[44] J. M. Hu , Z. Li , Y. H. Lin and C. W. Nan , Phys. Status. Solidi RRL, **4**, 106 (2010).

[45] M. Liu, O. Obi, J. Lou, Y. J. Chen, Z. H. Cai, S. Stoute, M. Espanol, M. Lew, X. Situ, K. S. Ziemer, V. G. Harris and N. X. Sun, Adv. Funct. Mater. **19**, 1826 (2009).

[46] J. Das, Y. Y. Song, N. Mo, P. Krivosik and C. E. Patton, Adv. Mater. **21**, 2045 (2009).

[47] H. Greve , E. Woltermann , H. J. Quenzer , B. Wagner and E. Quandt, Appl. Phys. Lett. **96**, 182501 (2010).

[48] J. H. Song, J. Zhou and Z. L. Wang, Nano Lett. **6**, 1656 (2006).

[49] P. X. Gao, J. H. Song, J. Liu and Z. L. Wang, Adv. Mater. **19**, 67 (2007).

[50] S. P. Beeby, M. J. Tudor and N. M. White, Meas. Sci. Technol. **17**, R175 (2006).

[51] W. Ohashi, M. Sasaki, F. Takahashi and M. Murasato, Nippon Steel Tech. Rep. **59**, (1993).

[52] J. P. Zhou, H. C. He, Z. Shi, G. Liu and C. W. Nan, J. Appl. Phys. **100**, 094106 (2006).

[53] W. Zhang, A. Sun, X. Pan, Y. Han, X. Zhao, L. Yu,Z. Zuo and N. Suo, J. Magn. Magn. Mater. **506**, 166623 (2020).

[54] M. Kooti and A. N. Sedeh, J. Mater. Sci. Technol.,**29**, 34 (2013).

[55] S. J. Valasek, Phys. Rev. **15**, 537 (1920).

[56] J. R. Sambrano, E. Orhan, M. F. C. Gurgel, A. B. Campos, M. S. Goes, C. O. Paiva-Santos, J. A. Varela and E. Longo, Chem. Phys. Lett. **402**, 491 (2005).

[57] M. C. Cheung, H. L. W. Chan and C. L. Choy, J. Mater. Sci. **36**, 381 (2001).

[58] J. Su and J. Zhang, J. Mater. Sci. Mater. Electron. **30**, 1957 (2019).

[59] R. V. Chopdekar and Y. Suzuki, Appl. Phys. Lett. **89,** 182506 (2006).

[60] Y. S. Koo, K. M. Song, N. Hur, J. H. Jung, T.H. Jang, H. J. Lee, T. Y. Koo, Y. H. Jeong, J. H. Cho and Y. H. Jo, Appl. Phys. Lett. **94**, 032903 (2009).

[61] P. N. Oliveira, D. M. Silva, G. S. Dias, I. A. Santos and L. F. Cotica, Ferroelectrics **499**, 76 (2016).

[62] M. Liu, Z. Zhou, T. Nan, B. M. Howe, G. J. Brown and N. X. Sun, Adv. Mater. **25**, 1435 (2013).

[63] M. K. Niranjan, J. D. Burton, J. P. Velev, S. S. Jaswal and E. Y. Tsymbal, Appl. Phys. Lett. **95**, 052501 (2009).

[64] S. Umashankar, T. Parida, K. Ramesh kumar, A. M. Strydom, G. Markandeyulu and K. K. Bharathi, J. Magn. Magn. Mater. **439**, 213 (2017).

[65] V. Gorige, R. Kati, D. H. Yoon and P. S. Anil Kumar, J. Phys. D: Appl. Phys. **49**, 405001 (2016).

[66] Manjusha, K. L. Yadav, N. Adhlakha, J. Shah and R. K. Kontnala, Physica B **514**, 41 (2017).

[67] M. Zeng, J. G. Wan, Y. Wang, H. Yu, J. M. Liu, X. P. Jiang and C. W. Nan, J. Appl. Phys. **95**, 8069 (2004).

[68] C. E. Ciomoga, I. Dumitru, L. Mitoseriu, C. Galassi, A. R. Iordan, M. Airimioaei and M. N. Palamaru, Scr. Mater. **62**, 610 (2010).

[69] T. H. Ting and K. H. Wu, J. Magn. Magn. Mater. **322**, 2160 (2010).

[70] J. P. Zhou, L. Lv, Q. Liu, Y. X. Zhang and P. Liu, Sci. Technol. Adv. Mater. **13**, 045001 (2012).

[71] Y. Liu, Y. Wu, D. Li, Y. Zhang, J. Zhang and J. Yang, J. Mater. Sci. Mater. Electron. **24**, 1900 (2013).

[72] B. Sarkar, B. Dalal, V. D. Ashok, K. Chakrabarthi, A. Mitra and S. K. De, J. Appl. Phys. **115**, 123908 (2014).

[73] H. F. Tian, T. L. Qu, L. B. Luo, J. J. Yang, S. M. Guo, H. Y. Zhang, Y. G. Zhao, J. Q. Li, Appl. Phys. Lett. **92**, 063507 (2008).

Chapter 2

Experimental techniques

To understand ME phenomena in ferrite and FE composites, particularly in NFO−BTO particulates, the required samples were synthesized by using a SSR method. The synthesized samples were characterized by several physicochemical characterization techniques. The physical properties of these particulate composites were undertaken by using appropriate instruments and adopting suitable measurement techniques. In this chapter, the basic principles involved in preparation, characterization, and physical property measurements were discussed. This chapter also includes strategies and protocols adopted for various characterization tools and measurement techniques.

2.1 Material preparation

In the present context, to demonstrate the ME effect by measuring different physical properties of particulate composites, the quality of samples is very crucial. Obviously, the signatures of ME effects can be seen clearly in single-crystalline heterostructures, whereas it becomes difficult to observe the ME effect in poly-crystalline samples due to various reasons [1]. Therefore, the phase purity and distinct hetero-grain coupling in composites are critical. Also, for the chosen set of oxide materials, the composition, density, and coexistence of two individual phases in the composite form are the major concerns. In view of these reasons, even though several methods such as "sol-gel" [2], "co-precipitation" [3], "Pechini method" [4, 5], "hydrothermal method" [6], "SSR" method [7] and "microwave-hydrothermal" method [8] are available. Out of these methods, the SSR method is the best-suited method for preparing NFO, BTO, and BTO−NFO composites samples. The SSR technique was optimized for single-phase and composite samples to ensure data quality, which was acquired from various physical properties measured in the present investigation.

2.1.1 Solid-state reaction method

The SSR method is one of the most straightforward and primary preparation techniques to synthesis the ceramic materials in single-phase and composite forms. In this technique, a sufficiently high temperature is required for the chemical reaction

to occur among the solid ingredients. It is the best-suited to make bulk polycrystalline materials.

There are several advantages with this method, particularly in the present context; the materials prepared in this method are chemically stable, structurally pure, and non-toxic at room temperature as they are heat-treated at high-temperatures [9]. It is a physically viable method to prepare bulk quantities of polycrystalline samples with a low-loss of ingredients. However, the SSR method is a time-consuming process compared to other techniques. In general, once the single phase of material is formed, it will not react with any other chemical or decompose until it reaches at its melting point temperature. Therefore, in the case of materials prepared by the SSR method, the physical properties can be measured in the range of higher temperatures based on the requirement. Mainly, for estimated results of physical properties in ME particulate composites (a) there should not be any chemical reaction in between single-phase materials, (b) high "magnetostriction" coefficient for magnetic phase and the large "piezoelectric" coefficient for FE material, (c) there should be less lattice mismatch between the hetero-grains for optimal strain from one phase to the other phase and (d) there should be a clear contact interface between the hetero-grains [10, 11]. Therefore, SSR is a unique method for preparing the particulate composites because the issues mentioned above will be taken care of.

In this method, after weighing the individual ingredient solid materials in the stoichiometric ratio, the proper mixing will be done by either "pestle and agate mortar" or "ball milling" process. The ball milling is used to mix the powder in larger quantity whereas the pestle and agate mortar will be used for the small quantities. In these techniques, unlike wet chemical reaction techniques, the ingredient will not react at room temperature due to insufficient activation energy. Therefore, it requires high temperature i.e. 1000 °C to 1500 °C with suitable heating and cooling rates [12, 13]. During the grinding, acetone can be added to the powder for proper mixing.

2.1.2 SSR reaction mechanism

The mechanism involved in SSR was proposed by Randall M. German [9]. The formation of the required phase comes to form the proper mixing (grinding) and heating processes of solid ingredients. During the grinding process, the components were facilitated to be nearby with a fresh surface of its own phase, and as a result, relatively low external energy is required for SSR to occur. As shown in Fig. 2.1, the ingredients A and B will be activated to come nearby to form C when the sufficient temperature is provided, and the corresponding reaction is given by,

$$A + B \longrightarrow C \tag{2.1}$$

here, A and B are initial ingredients, and C is the final product. During the heating process, the temperature will act as a driving force for the individual ingredients to

react and form the required phase. Also, thermal energy will enable the ingredients to undergo microscopic geometrical change followed by atomic motion. Here, the motion of atoms will follow the Arrhenius relation given by,

$$\frac{N}{N_o} = e^{-\frac{Q}{RT}} \tag{2.2}$$

here, N is the number of atoms in motion, N_o is the total number of atoms, Q is the "activation energy", R is the "gas constant", and T is the absolute temperature.

During heating, the temperature will cause the interaction between the surfaces of two adjacent grains, thereby reducing the average surface area. The shrinkage in volume and increment in the density of the material takes place. Therefore, grinding and subsequent heating of the sample helps in forming the required phase progressively, thereby eliminating the pores in the sample. In general, the grain size of the final material (C) will be 1.26 times that of grain sizes of initial ingredient materials (A and B) [9]. The smaller grains of the ingredient will react easily to form the required phase due to the components' high contact interface. In each intermediate grinding and heating process, the required phase (C) formation needs to be checked using XRD measurement.

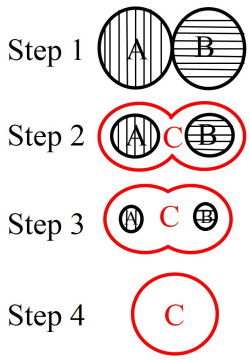

FIGURE 2.1: Schematic representation of solid-state reaction method, modified after [14] (2014, Springer).

In the present investigation, the single-phase materials of NFO and BTO were synthesized by using the SSR method, and then the stable single-phase materials were further co-sintered to form the composites of NFO and BTO. The complete details of the preparation method are given in chapter 3.

2.2 Characterization

Characterization of the prepared materials is very important to ascertain the quality of the samples. The quality of the materials can be known by employing several characterization techniques. Before proceeding to any of the physical properties, one needs to know the basic information about the structure of the material, elemental composition, morphology, and microstructure of the samples. The commonly employed characterization and analysis techniques for the particulate composites are

XRD, Rietveld refinement, field emission scanning electron microscope (FESEM), and energy dispersive x-ray spectroscopy (EDXS).

2.2.1 X-ray diffraction

Rontgen discovered x-rays in 1895, and these are a part of electromagnetic radiation, having the wavelength range 1-100 Å with energies 100 eV-1000 keV. The x-rays with energy range 1-120 keV comes under hard x-rays and mostly used for diffraction studies. In order to study the structure, composition, and physical properties of the solid materials, x- rays are used extensively. When the incident beam of x-rays interacts with any material, a part of it gets transmitted, some part of it scattered, and a part of it gives rise to fluorescence. If the material is crystalline, the x-rays scatter from different sets of planes. The scattered wave undergoes either constructive or destructive interference based on the path difference of the interfering waves. If θ is the incidence angle of the x-rays concerning the plane of the crystal and d is inter-planar spacing, constructive interference occurs when the path difference

$$n\lambda = 2dsin\theta \tag{2.3}$$

W. L Bragg first formulated this relation and known as Bragg's law [15]. Since sinθ cannot exceed 1, then the above equation can be written as

$$\frac{n\lambda}{2d} = sin\theta < 1 \tag{2.4}$$

The above equation clearly states that $n\lambda$ must be less than $2d$. Here the possible lowest value of n for the occurrence of diffraction is 1, then equation becomes

$$\lambda < 2d \tag{2.5}$$

For the most set of crystal planes, d is the order of 3 Å. This clearly indicates that λ cannot exceed the order of 6 Å.

The photograph of x-ray diffractometer is shown in Fig. 2.2, the x- rays emitted from the source are directed to the sample mounted on the sample stage or holder. The x-rays, which are scattered from the different planes of the sample, are detected with the x-ray detector. An electronic system which converts the charge into voltage pulse is attached to the detector. A voltage pulse is proportional to the intensity of the diffracted beam. Each peak in the XRD pattern corresponds to one set of parallel planes. In general, each set of parallel planes will be indicated above the peak with their corresponding Miller indices.

The XRD characterization was carried out in the powder method at room temperature on pelletized samples in 2θ range from 10° to 90° and step size of 0.02° with scan rate 0.7°/min. by using a Bruker D8 Advance diffractometer.

FIGURE 2.2: Photograph of x-ray diffractometer.

2.2.2 Rietveld refinement

The Rietveld refinement was developed by H. M. Rietveld to refine the magnetic and crystal structure from powder neutron diffraction data in the year 1967 [16] and it was improved further in 1969 to accomplish for XRD data [17]. Rietveld refinement makes us refine the structural parameters such as atomic position, bond-length, bond-angle, lattice parameters, and angles. Rietveld refinement of XRD pattern can be done using different software Fullprof, MAUD, Rietica, GSAS, BGMN, BRASS, High score plus, Topas, Autoquan, PDXL, and JADE, etc. The best fits were decided based on the fitting parameters of "profile" factor (R_P), "weighted profile" factor (R_{WP}), "expected weighted profile" factor (R_{exp}), and "goodness of fit" (GOF), the equations corresponding to these parameters are given in equations 2.6, 2.7, 2.8 and 2.10 respectively.

$$R_p = \frac{\Sigma|y_i^{obs} - y_i^{cal}|}{\Sigma y_i^{obs}} \tag{2.6}$$

$$R_{wp} = \sqrt{\frac{\Sigma(y_i^{obs} - y_i^{cal})^2 w_i}{\Sigma w_i (y_i^{obs})^2}} \tag{2.7}$$

$$R_{exp} = \sqrt{\frac{N - P}{\Sigma w_i (y_i^{obs})^2}} \tag{2.8}$$

where, w_i represents the statistical weight of the i^{th} point, y^{obs} refers the whole obtained i^{th} point intensity. The N and P represent the total number of points in the patterns and refined parameters, respectively. The final evaluated intensity,

$$y_i^{cal} = A \cdot p \cdot s \cdot \eta \sum P_{hkl} \cdot L_{hkl} \cdot {F_{hkl}}^2 \cdot profile \cdot 2(\theta_{hkl} - \theta_i) + B \tag{2.9}$$

here, A, B, s, p, and η are representing the "absorption", "background noise", "scale-factor", "polarization", and "extinction" of the experiment, respectively. The L_{hkl} and P_{hkl} represent the "geometry" and "preferred orientation" parameters. While refining, all these parameters may vary consistently in order to obtain the synergy between calculated and experimental diffraction patterns. In the process of evaluation, several numerical parameters can be taken into account to judge the GOF. In the process of fitting, several parameters viz., "unit cell", "background", "peak-profiles", "scale", "full-width at half maxima" (FWHM), "occupancies", "shape", and "atomic positions" are changed systematically by employing successive iterations, until the best possible fit is arrived. The best-fit patterns are affirmed by "GOF" (χ^2), and the corresponding best-fit term is given as

$$GOF = \frac{R_{wp}}{R_{exp}} \tag{2.10}$$

Ideally, the GOF value is 1. If the GOF value is less than 1, standard uncertainties are overestimated, and more parameters are introduced to fit the data while refining. If GOF value is large (GOF$\gg$ 1) indicates the bad fitting. Acceptable value for GOF is less than 5 [18]. The most important thing is that difference should be less between observed data and calculated data, which is given by

$$S_y = \sum (y_i^{obs} - y_i^{cal})^2 w_i \tag{2.11}$$

In the present investigation, *High score plus* software was used for refining the XRD patterns of the prepared samples. While employing the *High score plus* software, the following procedure was followed to refine the single-phase and composite materials.

Step 1 : The background was fitted carefully without affecting the peaks using granularity and bending factors.

Step 2 : Identified all the peaks present in the observed pattern to calculated pattern with peak search option. The identified number of peaks can be modified by

insert/delete peak options.

Step 3 : Profile fitting was done by refining the background parameters manually. Global parameters were refined manually, i.e., zero shift, specimen displacement, and wavelength. The "Pseudo-Voigt" function was used as a profile function, it is a semi function of Gaussian and Lorentzian functions, and this function was considered as the best suited for XRD pattern.

Step 4 : Profile fitting was done in automatic mode by default profile fitting. The repeated fitting were performed until the observed pattern matches with the calculated pattern.

Step 5 : The right side of each peak in the pattern looks like a shoulder; these belong to $K_{\alpha 2}$ peaks. After confirming the profile fitting is perfect, then strip the $K_{\alpha 2}$ wavelength from the pattern.

Step 6 : Select the suitable international centre for diffraction data (ICDD) file, which can match with the measured XRD pattern.

Step 7 : Refine the scale factor and B-overall for each phase in the composite; these parameters are multiplication factor for fitting the calculated and observed data and thermal factor, respectively.

Step 8 : One by one, refine the lattice parameters (i.e., a, b, c) of each phase's unit cell in the composite. Initially, lattice parameters will be taking from the ICDD file, and these parameters were used to modify the relevant data while refining.

Step 9 : Atomic coordinates, B-isotropic, and occupancy were fitted systematically. Here, in the case of atomic coordinates, the integers values were not refined, and decimal numbers were refined.

Step 10 : The FWHM of each peak was fitted by using U, V, and W parameters. Here U and W should be positive while V is negative. The shape parameters were refined separately for better profile fitting.

This procedure was followed by checking the refined parameters and different patterns with each cycle of the fitting. The data was refined in several processes until the GOF value is nearly unity or less than two.

2.2.3 Field emission scanning electron microscopy

In this technique, the electrons are fired from the field emission source. The electrons will reach the sample after passing through several lenses and coils in a high vacuum. These electrons will interact with the sample and scatters. Suppose the scattered electrons are secondary electrons (SE); in that case, these electrons will be detected by the SE detector, and if scattered electrons are backscattered electrons

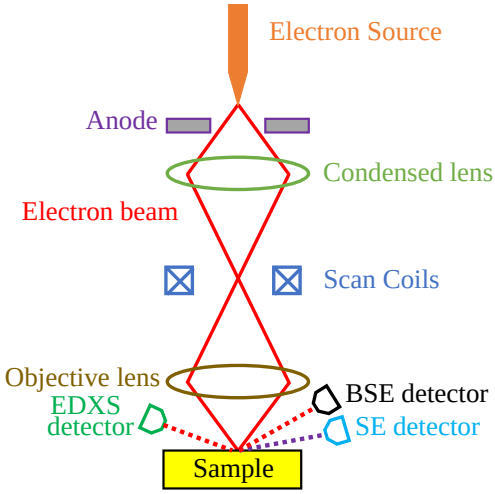

FIGURE 2.3: Representation of basic principle of field emission scanning electron microscope, modified after [19] (1992, Manning publications Co.).

(BSE), then it will be detected by the BSE detector. The schematic representation of the interaction of electrons with the sample is shown in Fig. 2.3.

Since the energy of SE electrons is less than 50 eV, the SE detector will give the sample's surface morphology information. The energy of BSE electrons is more than 50 eV, and the corresponding detector will give the surface morphology and contrast between different phases present in the composite. In BSE images, the heavier (molecular weight) atom may lead to a brighter image, and the lighter (molecular weight) atom may give a dark image. It is because the more significant atomic number of the larger atom has a more cross-sectional area; consequently, the BSE detector will get more electrons and looks brighter in the image [20].

The FESEM is a useful technique to know the surface morphology of the material. It will give information about grain size, grain shape, and contact interface in between grains. Particularly in BSE mode, color contrast may give the information about the phases present in the sample, and the contact interface will be clearly figured. For significant ME coupling, the contact interface should be sharp and large enough. This information can be given only by FESEM in BSE mode. So, it is necessary to characterize the particulate composite with the FESEM technique in BSE mode. The FESEM images of prepared samples were carried out in BSE mode using the Gemini 500 microscope.

2.2.4 Energy dispersive x-ray spectroscopy

The EDXS technique is used for the elemental analysis of grains in the sample. Using the EDXS, it can be label each grain present in the sample. Usually, EDXS is attached to the FESEM instrument, and it will be working based on the principle of FESEM. When bombarding the primary electrons on the sample, these primary electrons will kick out an electron from the K-shell of the atom in the sample, and

one electron vacancy will create in K-shell. An electron jumps from the L-shell for filling the electron vacancy in K-shell by releasing a photon. This released photon will have the characteristics of x-rays, and it is called K_{α} x-rays. The schematic representation of the interaction of the electron with the atom is shown in Fig. 2.4. If an electron will jump from the M-shell to fill the electron vacancy in K-shell with releasing a photon or x-rays (K_{β} x-rays). The released energy of x-rays is unique for each element to characterize the elemental analysis and chemical composition of the sample. The compositional and elemental analysis of prepared samples were done by using EDXS, which was attached to the FESEM.

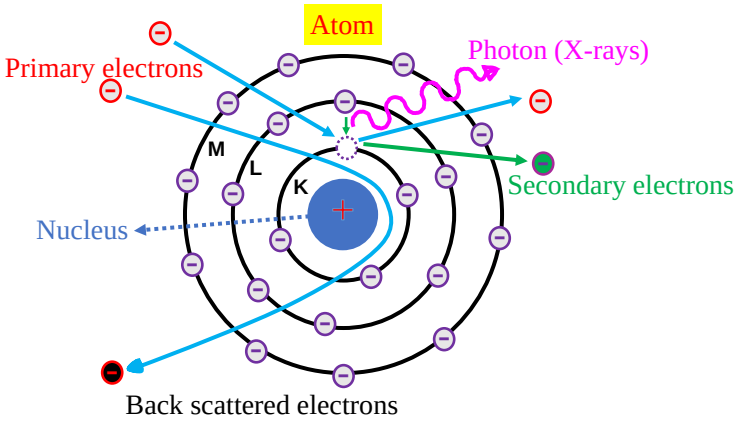

FIGURE 2.4: Schematic representation of electron interaction with the atom, modified after [19] (1992, Manning publications Co.)

2.3 Magnetic Properties

Magnetization and magnetic susceptibility can be measured in several ways: "induction method", "force method", "electrical method", and "magneto-optic" methods. The vibrating sample magnetometer (VSM) comes under the induction method, which is being widely used nowadays. The ME coupling in ferrite and FE composites is done by measuring the magnetic measurements. The magnetic measurements were done by using suitable instruments such as VSM and physical property measurement system (PPMS) for the higher than room temperature and lower than room temperature, respectively.

2.3.1 Vibrating sample magnetometer

The VSM works based on the principles of Faraday's law and Ampere's law. Ampere's law says that electric current (I) flowing in the wire generates the magnetic field (H) around the wire i.e. electromagnet. Electromagnets are used in VSM for generating the magnetic field. Here, sample is magnetized by using electromagnets and magnetized sample is moving in between pick up coils. During the measurement, sample will be vibrating in between pickup coils with a fixed frequency and

amplitude. The electromotive force will induce in the pick up coil based on Faraday's law of induction, given by the equation 2.12 and developed magnetic moment is given by the equation 2.13. The schematic representation of VSM is shown in Fig. 2.5.

$$emf = -N\frac{d\phi}{dt} \tag{2.12}$$

Here, emf, N, ϕ and t are the electromotive force, number of turns, magnetic flux and time, respectively.

$$m = IA \tag{2.13}$$

Here, m, I and A are the magnetic moment, electric current, and area of the coil, respectively.

The VSM is a useful technique to measure the magnetization as a function of temperature and applied magnetic field. It can measure very sensitive and accuracy as 10^{-6}emu. The VSM can be used to measure the magnetization at high temperature and low temperature. The low-temperature setup can measure liquid nitrogen temperature (80 K to 400 K), whereas a high-temperature setup can be used from room-temperature to 1273 K. Maximum error in the temperature scan will be $\pm$0.2 K.

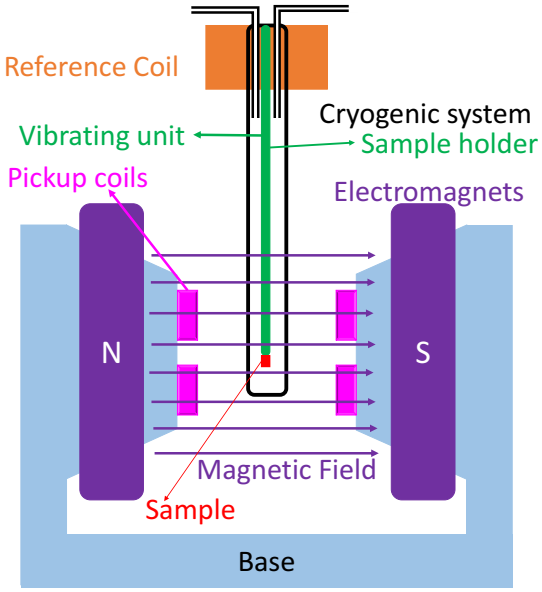

FIGURE 2.5: Schematic representation of vibrating sample magnetometer , modified after [21] (2014, Ijournals).

The Curie temperature (T_C) of nickel ferrite is at 593 °C in the prepared composites. The effect of FE material on Curie temperature of ferrite will be known from the temperature-dependent magnetic measurements of composites with the VSM technique at high temperatures. Magnetic field dependent measurements will give the information of magnetic parameters variations when FE material changes from

"tetragonal" to "cubic" phase. The temperature-dependent magnetic measurements are measured in the range of 30 °C −700 °C at an applied magnetic field of 250 G. Magnetic hysteresis loops are measured in the range of ±12 kG at a ferromagnetic phase of NFO (or cubic phase of BTO), i.e., 300 °C on the cubic shape samples 2×2×2 mm^3 dimensions. These magnetic measurements are done by using a VSM (Lakeshore).

2.3.2 Physical properties measurement system

The PPMS is a powerful system to measure the physical properties such as AC susceptibility, magnetic anisotropy, electric resistivity, Hall effect, I-V characteristic thermal conductivity, Seebeck coefficient, and differential resistance as a function of temperature and magnetic field. It can measure the measurements in the form of thin-film, powder, pellet, and liquid. The PPMS is a unique system for measuring the magnetic properties at lower temperatures, such as at 2 K with sensitive magnetization and high magnetic field ±16 Tesla. The NbTi/Nb_3Sn superconducting magnets are used in the PPMS system; these superconductors generate a magnetic field when they are cooled in liquid helium, which is surrounded by liquid nitrogen. During the measurement, the sample will be vibrating with 40 Hz frequency. Measurements are carried out on the PPMS-VSM system with the help of automated programmable control with auto centering the sample.

FIGURE 2.6: Photograph of physical property measurement system.

The magnetic field dependent measurements will give the information of magnetic parameters, and their variations when FE material varied from "tetragonal"

to "orthorhombic" to "rhombohedral" phase. In the present case, ME coupling phenomena cannot be explained by measuring the ME coupling coefficient (α), due to leakage presence in it. The ME coupling phenomena can be explained by measuring the temperature-dependent magnetic measurements with the PPMS technique. The magnetic measurements are carried out on PPMS system shown in Fig. 2.6 on $2\times2\times2$ mm^3 samples. The temperature-dependent magnetic properties were performed by cooling the system from 330 K to 100 K, and heating 100 K to 330 K at a constant applied magnetic field 250 Oe. The magnetic hysteresis loops were measured in the range ±3 Tesla at three phases of BTO, i.e., 150 K, 230 K, and 300 K.

2.3.3 Electron spin resonance

The "electron spin resonance" (ESR) or "electron paramagnetic resonance" (EPR) is one of the spectroscopic techniques, and Zavoiskii discovered it in 1944 in $MnSO_4$ using 47.60 G dc magnetic field and 133 MHz rf-magnetic field [22]. This technique is an extension of the famous Stern-Gerlach experiment. It is used for studying the materials having unpaired electrons. The ESR concepts are similar to those of nuclear magnetic resonance (NMR) except that in ESR, electron spins are excited. In contrast, in NMR, the spins of atomic nuclei are excited. The ESR spectrometers are made available commercially with wide range of frequency, as shown in Table 2.1. The most common choice of ESR spectrometer is the X-band microwaves with a frequency of 9-10 GHz; the corresponding wavelength is in the range of 3.0-3.3 cm, and in the middle of X-band, the "free electron resonance" is found at 3390 G.

TABLE 2.1: List of frequency, wavelength and magnetic field of various ESR spectrums

Designation	Frequency (GHz)	Wavelength (cm)	Magnetic field (G)
S	3.0	10.0	1070
X	9.5	3.15	3390
K	23.0	1.30	8200
Q	35.0	0.86	12500

2.3.3.1. Origin of the ESR signal

If the electron is in a magnetic field, the degeneracy of spin energy levels of electron will be lifted, which can be represented by spin Hamiltonian [23],

$$H_s = g\mu_B B S_z \tag{2.14}$$

Where, g is the "Lande g-factor" (g = 2.002), and μ_B is the "Bohr magneton", B is the "magnetic field strength", and S_z is the z-component of the "spin angular momentum operator". The energy eigenvalues of the electron spin energy levels can

be calculated by applying H_s to the electron spin eigen functions representing to magnetic component $m_s = \pm\frac{1}{2}$

$$H_s|\pm\frac{1}{2}>=\pm\frac{1}{2}g\mu_B B = E_\pm|\pm\frac{1}{2}> \tag{2.15}$$

From this, energy eigenvalues can be written as

$$E_\pm = \pm\frac{1}{2}g\mu_B B \tag{2.16}$$

Thus, the difference in energy between two levels can be given as

$$\Delta E = E_+ - E_- = g\mu_B B \tag{2.17}$$

The movement of an electron takes place between the two energy levels by either absorption or emission of a photon with energy $h\nu$, where h is the Plank constant, and ν is the photo's frequency .

Hence, the above equation takes the form

$$\Delta E = g\mu_B B = h\nu \tag{2.18}$$

This is the fundamental equation in ESR spectroscopy. The splitting of energy levels in magnetic field are shown in Fig. 2.7.

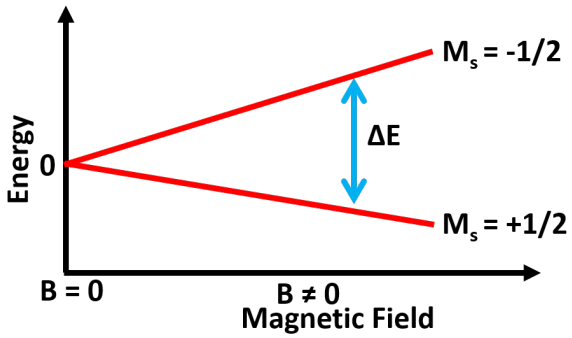

FIGURE 2.7: Schematic representation of splitting of spectral line in the presence of magnetic field, modified after [24] (1967, Springer).

As the ESR sample is consisting of a collection of many paramagnetic species, so that the following equation can write its statistical distribution according to Maxwell-Boltzmann distribution,

$$\frac{N_+}{N_-} = exp(-\frac{E_+ - E_-}{kT}) = exp(-\frac{g\mu_B B}{kT}) = exp(-\frac{h\nu}{kT}) \tag{2.19}$$

In the above equation N_+ and N_- denote the number of paramagnetic centers occupying upper energy state and lower energy state, respectively, k is the "Boltzmann constant" and T is the temperature.

For an X-band ESR spectrometer, the microwave frequency ν = 9.70 GHz is used. The substitution of ν value in the above equation gives $\frac{N_+}{N_-}$= 0.99. This indicates

that the upper state has a lower population than the lower state, which mean the transition from the lower level to the higher level will happen more likely, and this occurs via absorption (Fig. 2.8) of energy.

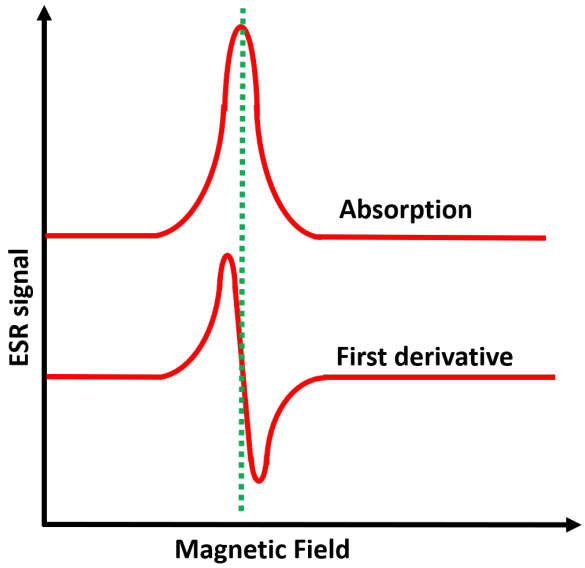

FIGURE 2.8: Schematic representation of ESR signal, modified after [24] (1967, Springer).

As we know that $N_+ = N_- = \frac{N}{2}$, the population difference can be written as

$$N_- - N_+ = \frac{Ng\mu_B B}{2kT} \tag{2.20}$$

This equation gives the information that the ESR sensitivity increases with the total number of spins, N, increasing magnetic field strength, and decreasing temperature. An absorption field is proportional to microwave frequency, which means that the higher frequency band spectrometers have more sensitivity.

FIGURE 2.9: Photograph of electron spin resonance spectrometer.

The photograph of ESR spectrometer is shown in Fig. 2.9. It consists of a microwave source, cavity, magnet, sample holder, and detector diode. The microwaves

are generated by a Klystron oscillator and passthrough a rectangular waveguide to the attenuator. The power level is adjusted with the attenuator. The attenuator transfers its output to the resonator in which the sample is placed. When the radiation from the cavity has reflected the detector containing a diode that covers the microwave power into electric current, it is then amplified and fed to a suitable recorder. The circulator acts as a traffic circle through which microwaves are passed. The magnetic field is swept across the resonance condition by varying the current using the modulation coils mounted on the cavity walls. The amplified ESR signal appeared as absorption and first derivative curves, as shown in Fig. 2.8.

2.4 Dielectric properties

The dielectric spectroscopy is used for the observation of electric dipoles present in the sample. The dielectric spectroscopy can measure the permittivity as a frequency-dependent at constant temperature and temperature-dependent permittivity at a constant frequency. The dielectric spectroscopy is used for the bulk materials, devices, thin-film analysis. These measurements can give information on permittivity, conductivity, impedance, activation energy, and charge mobility. The same information can be obtained from the LCR meter like dielectric spectroscopy, but the frequency range is less, and some advanced parameters can be seen with dielectric spectroscopy. The dielectric materials are basically non-conductors, and these are two kinds that are relaxors and non-relaxors. The dielectric spectroscopy is sensitive to dipolar as well as localized changes in the material; it finds their intensity, kinetics, and interactions. The dielectric measurements will give the accurate transition temperature in the material. The relative permittivity (ε_r or ε') is ratio of permittivity of a material $\varepsilon(\omega)$ to the permittivity of a free space(ε_o).

When applying the voltage to the sample, charges will accumulate at interfaces, current will be measured, and it will convert as capacitance. The relative permittivity will give as output by considering the sample's thickness and area using the mentioned equations 2.21, 2.22, and 2.23.

$$\varepsilon_r = \frac{C}{\varepsilon_o}\frac{d}{A} \tag{2.21}$$

$$C = \frac{q}{V} \tag{2.22}$$

$$I = \frac{q}{t} \tag{2.23}$$

Here, C is the capacitance, d is the thickness of the sample, A is the area of the sample, t is the time, q is the accumulated charges, and V is the voltage applied to the sample.

In the prepared composites, the T_C of FE material is at 120 °C and the variation of ferrite material in FM−FE composites gives its effect on FE, which indirectly explains the ME phenomena in composites. It can be explained by measuring

FIGURE 2.10: Dielectric constant instrument photograph.

the temperature-dependent dielectic constant measurements at high temperatures (range 30 °C - 1200 °C). The frequency dependent dielectric measurements can give the information about the effect of ferrite on dipole moment of FE material.

The frequency dependent dielectric data were collected in the range of 1 Hz - 35 MHz at room temperature. The temperature-dependent dielectric measurements were done in the range of 30 °C - 225 °C while heating, at the frequencies 1 kHz, 10 kHz, 50 kHz, 100 kHz, 500 kHz and 1000 kHz with 1 V applied ac voltage. The dielectric measurements were done by using the *Novocontrol* impedance analyzer, shown in the Fig. 2.10. These measurements were done on the circular shape pellets with two sides painted by silver paste with the 15 mm diameter and 2 mm thickness dimensions.

2.5 Raman Spectroscopy

Sir Chandrashekhara Venkata Raman has discovered Raman spectroscopy in the year 1928. Raman effect occurs when light interacts with a molecule, atoms will

vibrate symmetrically, and light wavelength will change. After interacting with the sample with the laser, if the wavelength increases, then it is called "stokes," and if it decreases, it is called "anti-stokes." Generally, the Raman spectrum measures the stokes in the form of Raman shift $(\frac{1}{\lambda})$ due to the intensity of the stokes is higher than anti-stokes.

$$\frac{1}{\lambda} = \frac{1}{\lambda_{incident}} - \frac{1}{\lambda_{scattered}} \tag{2.24}$$

The number of vibrating modes for linear and nonlinear molecule are 3N-5 and 3N-6, respectively. While the atoms are vibrating in the molecule, if dipole moment changes, then it is an IR active mode, and if polarizability changes, then it is a Raman active mode. The Raman spectrum returns in symmetric vibrations of molecules. In the Raman spectrum, each peak corresponds to one kind of vibration of a molecule in the material.

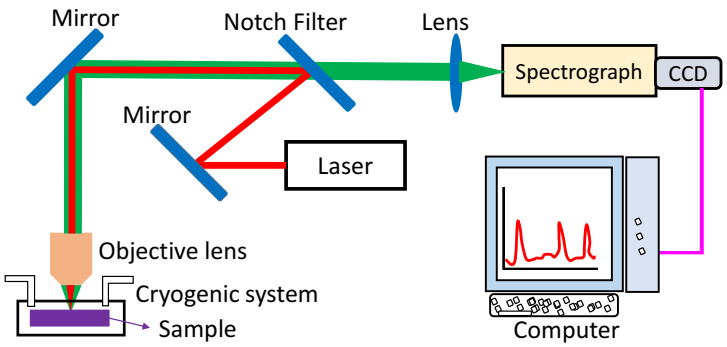

FIGURE 2.11: Schematic representation of Raman spectroscopy, modified after [25] (2003, Elsevier).

The Raman spectroscopy is used to see the molecular structure of a material. In the composites, ferrite material vibrations may be affected by ferroelectric material, and vice versa; these effects will be studied by Raman spectroscopy.

In the present work, the Raman spectrums of single-phase NFO, BTO, and composites were seen using the instrument Scanning Near field Optical Microscopy (SNOM) made by the Renishaw inVia micro-Raman microscope. In the SNOM Nd: YAG, 532 nm laser was used with a back scattering geometry equipped in the confocal Raman microscope spectrometer. The scattered rays were detected with a charge-coupled device (CCD) detector (model alpha 300 of WiTec, Germany) using a 100X objective lens (Olympus). A schematic representation of the Raman instrument is shown in Fig. 2.11.

The Raman measurements were carried out for single-phase and composite samples. The Raman data were collected at different temperatures pertaining to different FE phases of BTO, i.e., "tetragonal" (300 K), "orthorhombic" (230 K), and "rhombohedral" (150 K).

2.6 Ferroelectric properties

It is a well-known fact that FE materials have spontaneous "polarization", and it will be polarized by applying sufficient electric field. While using the electric field, the domain orientation and switching happen in the individual grains of material. A continuous application of the electric field at a specified frequency by measuring the "polarization" will give the electric hysteresis loop. From the hysteresis loop, "remanent polarization" (P_R), "saturation polarization" (P_S), and "coercive electric field" (E_C) parameters were extracted, and these parameters give the information of FE domains, domain boundaries, domain orientation, domain switching, etc.

The polarization versus electric field (P-E) loops were obtained using an advanced FE test system of aixACCT system GmbH, Germany on circular pellets (slabs) of diameter 10 mm thickness 1 mm, approximately. The prepared samples were taken for hysteresis loops by applying the electric field at 1 Hz frequency.

Bibliography

[1] Y. S. Koo, K. M. Song, N. Hur, J. H. Jung, T. H. Jang, H. J. Lee, T. Y. Koo, Y. H. Jeong, J. H. Cho and Y. H. Jo, Appl. Phys. Lett. **94**, 032903 (2009).

[2] M. Veith, S. Mathur, N. Lecerf, V. Huch and T. Decker, J. Sol–Gel Sci. Technol. **15**, 145 (2000).

[3] G. Vaidyanathan, S. Sendhilnathan and R. Arulmurugan, J. Magn. Magn. Mater. **313**, 293 (2007).

[4] M. Deluca, C. A. Vasilescu, A. C. Ianculescu, D. C. Berger, C. E. Ciomaga, L. P. Curecheriu, L. Stoleriu, A. Gajovic, L. Mitoseriu and C. Galassi, J. Eur. Ceram. Soc. **32**, 3551 (2012).

[5] M. P. Pechini, Method of preparing lead and alkaline earth titanates and niobates and coating method using the same for a capacitor, U.S. Patent No. 3330697; (1967).

[6] W. J. Dawson, Am. Ceram. Soc. Bull. **67**, 1673 (1988).

[7] G. H. Haertling, J. Am. Ceram. Soc. **82**, 797 (1999).

[8] Y. Xie, S. Yin, T. Hashimoto, H. Kimura and T. Sato, J. Mater. Sci. **44**, 4834 (2009).

[9] R. M. German, Powder metallurgy and particulate materials processing, 2005.

[10] Y. Liu, Y. Wu, D. Li, Y. Zhang, J. Zhang and J. Yang, J. Mater. Sci.: Mater. Electron. **24**, 1900 (2013).

[11] V. Gorige, R. Kati, D. H. Yoon and P. S. Anil Kumar, J. Phys. D: Appl. Phys. **49**, 405001 (2016).

[12] M. T. Buscaglia, M. Bassoli and V. Buscaglia, J. Am. Ceram. Soc., **88**, 2374 (2005).

[13] Z. Zhang, Y. Liu, G. Yao, G. Zu, X. Zhang and J. Ma, Physica E **45**, 122 (2012).

[14] A. Aytimur, S. Kocyigit and I. Uslu, J. Inorg. Organomet. Polym. **24**, 927 (2014).

[15] M. F. C. Ladd and R. A. Palmar, Structure Determination by X-ray Crystallography, New York: Plenum Press (1985).

[16] H. M. Rietveld, Acta Cryst. **22**, 151 (1967).

[17] H. M. Rietveld, J. Applied Cryst. **2**, 65 (1969).

[18] P. Singh , A. Sil, M. Nath and S. Ray, Physica B **405**, 649(2010).

[19] C. R. Brundle, C. A. Evans and S. Wilson, Encyclopedia of materials characterizations, Manning Publications Co. (1992).

[20] J. Shen, Y. Bai, J. Zhou and L. Li, J. Am. Ceram. Soc. **88**, 3440 (2005).

[21] E. Gupta, R. R. Yadav and M. Sharma, Int. J. Softw. **2**, 124 (2014).

[22] C. S. Sunandana, Bull. Mater. Sci. **21**, 1 (1998).

[23] P. H. Rieger, Electron Spin Resonance: Analysis and Interpretation, The Royal Society of Chemistry, (2007).

[24] T. H. Wilmshurst, Electron spin resonance spectrometers, Springer, (1967).

[25] J. R. Ferraro, K. Nakamoto and C. W. Brown, Introductory Raman spectroscopy, 2^{nd} edition, Elsevier, (2003).

Chapter 3

Preparation and characterization of NFO−BTO composites

The sample's phase purity, density, and microstructure are essential characterizations for observing the promising ME coupling in composites. The physical properties (viz., structural, magnetic, electric, dielectric etc.) of the sample are highly influenced by ME coupling's strength between the two ferroic component materials. The minute impurity may act as a dead layer at the hetero-grain interface and can significantly modify the mentioned physical properties. Therefore, it is essential to characterize the samples structurally by analyzing the phase of the individual components as well as composites. Also, ME coupling strength between magnetic and FE grains will not be promising if porosity is present in the composite. Therefore, ME coupling depends on the microstructure of the composite. Hence, it is necessary to examine the grain growth of the prepared samples. Certainly, the ratio of the constituent phases in the composite and their percolation is also a vital issue to ascertain the ME coupling.

In this chapter, the preparation of the single-phase materials and composites was discussed. The prepared samples were characterized by XRD to know the phase purity of the single-phase as well as composites. The refinement was done for the XRD patterns to see the variation in structural parameters in the composites. The density of the prepared samples was measured. The morphological characterizations were carried out using FESEM in the BSE mode to know the phase separation in composites. The variation in the lattice parameters, density, and grain size was observed and underlying mechanisms behind the variation of these parameters as a function of phase content was explained.

3.1 Sample preparation

The polycrystalline single-phase NFO and BTO were prepared by the standard SSR technique using ("Sigma Aldrich chemicals") NiO (99.99% purity), Fe_2O_3 (99.98%), $BaCO_3$ (99.98%),and TiO_2 (99.99%) respective components as starting compounds. The ingredients of BTO and NFO were mixed separately with the stoichiometric ratios. The mixed constituent powders were ground for several hours and measured

the thermal gravimetric analysis (TGA) to know the reaction temperatures of the ingredients.

Figure 3.1 shows the TGA plots of mixed NFO and BTO ingredients, measured in the range of 50 °C to 950 °C. In the mixed powders, ingredients will react and form the NFO and BTO phases, shown in the chemical equations 3.1 and 3.2. In these plots, it was observed that decreasing the weight of the sample with respective temperatures. It indicates that some chemical reaction between ingredients took place. In the case of NFO ingredients, the chemical reaction taking place starting from room temperature and becoming constant beyond 700 °C. It indicates the formation of NFO at 700 °C. The NFO will form from the ingredients without any gas evaporation [1]. In the case of BTO ingredients, a hump was observed at 700 °C. The hump in the TGA plots indicates weight loss in the constituents [2]. The chemical reaction was taking place in the BTO, starting from room temperature, and the hump is observed at 700 °C, which corresponds to the carbon dioxide gas release. In the case of BTO, decrement in the weight is continuing till 950 °C. It was confirmed that it is necessary to heat the sample beyond 950 °C to form the single phase BTO.

$$BaCO_3 + TiO_2 \longrightarrow BaTiO_3 + CO_2 \uparrow \tag{3.1}$$

$$Fe_2O_3 + NiO \longrightarrow NiFe_2O_4 \tag{3.2}$$

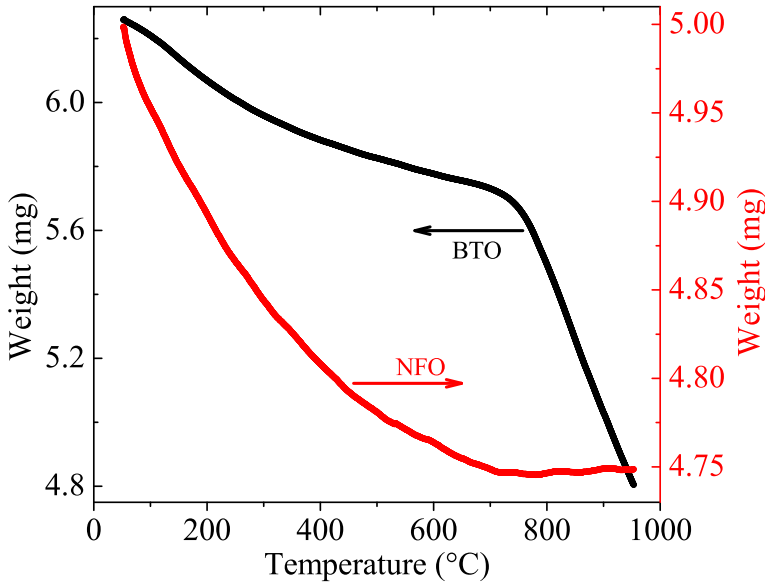

FIGURE 3.1: The thermal gravimetric analysis plot of NFO and BTO compounds.

The mixed component powders were ground for several hours and then made subsequent calcinations at various temperatures starting from 1000 °C to 1250 °C. At each intermediate grinding and heating, the samples were characterized by the XRD

to know the phase formation. Finally, BTO and NFO single-phase materials were obtained at 1200 °C for 8 hours and 1100 °C for 4 hours annealing, respectively. These single-phase materials were further ground and heated at higher temperatures 1250 °C, and 1300 °C for better purity and density. The preparation process of single-phase materials was shown in Fig. 3.2 as a flowchart.

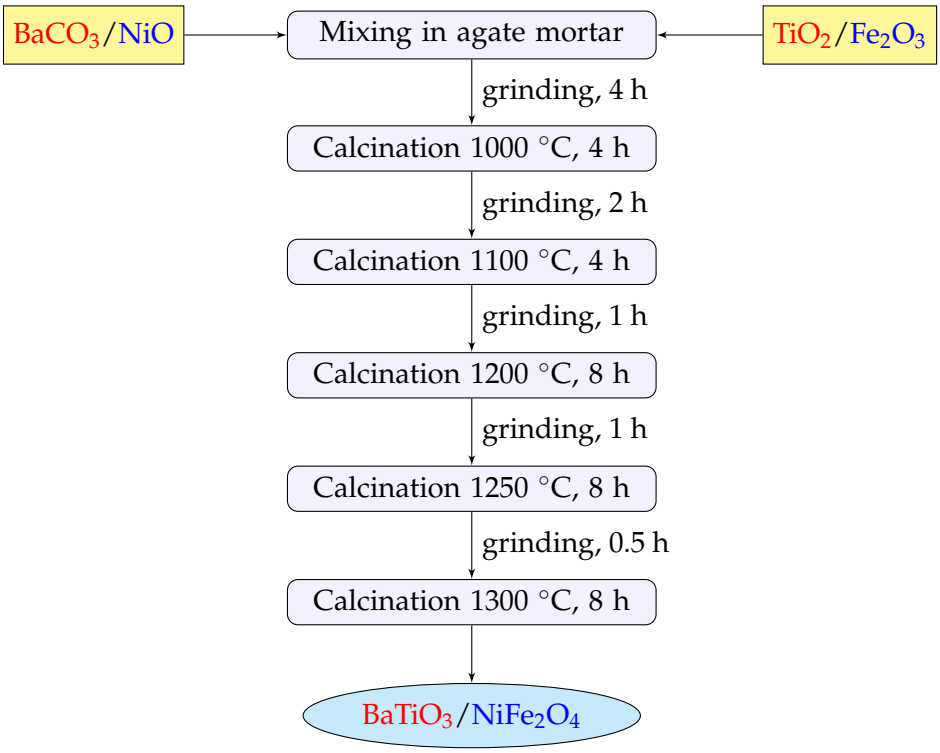

FIGURE 3.2: A flow chart for the preparation of single phase BTO and NFO samples.

After confirming the single-phase materials by XRD, composites were prepared by considering the single-phase materials as per (x)NFO + (1-x)BTO; x = 0 to 1 with 0.1 difference (here, x is a molecular weight ratio). The samples were made into circular shape pellets by applying 2.5 tons pressure for 5 minutes and sintered at 1350 °C. Before pelletizing the samples, 2% polyvinyl alcohol, a binding reagent, was added to the powders. After pelletizing, the samples were heated at 300° for 20 minutes to evaporate the binder. The preparation process of composite samples was shown in Fig. 3.3 as a flowchart. The prepared pellets of x = 0 to 1 composite samples sintered at 1350 °C is shown in Fig. 3.4. The characterization of composites is given in the next section.

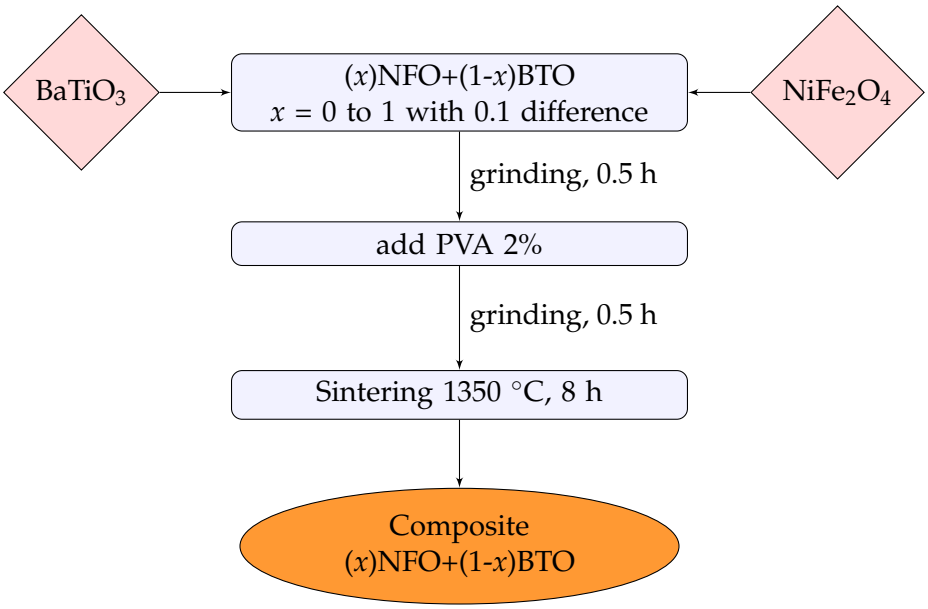

FIGURE 3.3: A flow chart for the preparation of composite (*x*)NFO+(1-*x*) BTO composite materials.

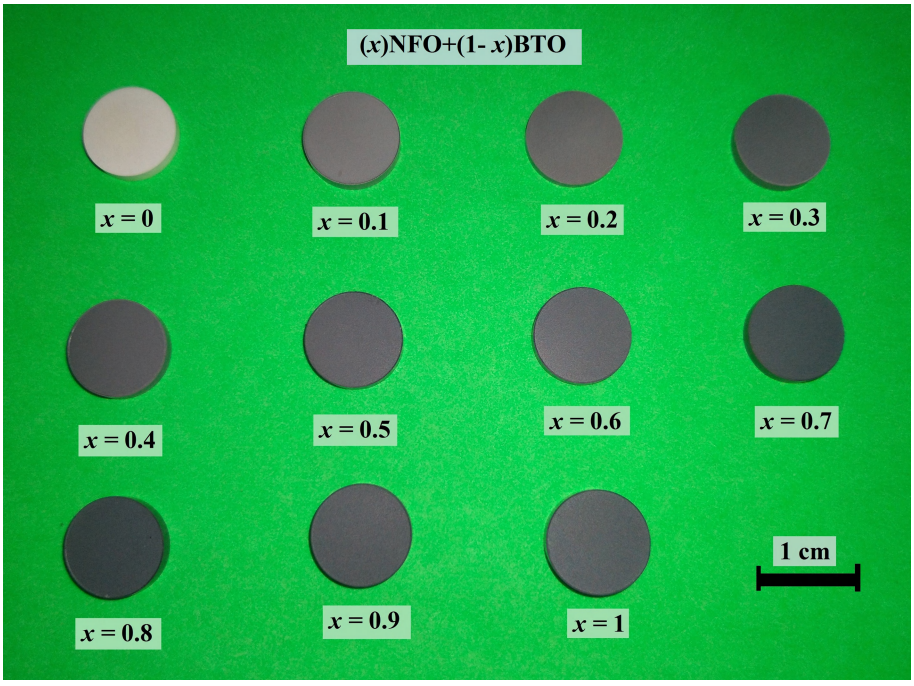

FIGURE 3.4: The pellets of NFO−BTO composites for $x = 0$ to 1, sintered at 1350 °C.

3.2 X-ray diffraction

Figures 3.5 show the XRD patterns of NFO and BTO samples, annealed at 1000 °C, 1100 °C, 1200 °C, 1250 °C and 1300 °C temperatures. While preparing the single-phase materials, characterization was done at each intermediate heating. It was observed that peaks corresponding to ingredients phases gradually found to decrease

and completely disappear at certain heating temperatures; finally, the peaks corresponding to the single-phase were present. The single-phase NFO and BTO are formed at heating temperatures of 1100 °C and 1200 °C, respectively, from the respective ingredients. The single-phase of compounds were confirmed from the XRD pattern without any secondary phase peaks. Basically, XRD can measure the 95% phase purity of the sample. The single-phase materials (heated 1200 °C) were reacting in composites, which means that the ingredients do not react completely to form the single-phase materials. This problem was overcomed by heating the single materials at higher sintering temperatures. Also, the sample heated at higher temperatures will give a higher density. For the observation of ME coupling phenomena in the composites, it is necessary to have single-phase materials without any reaction between them.

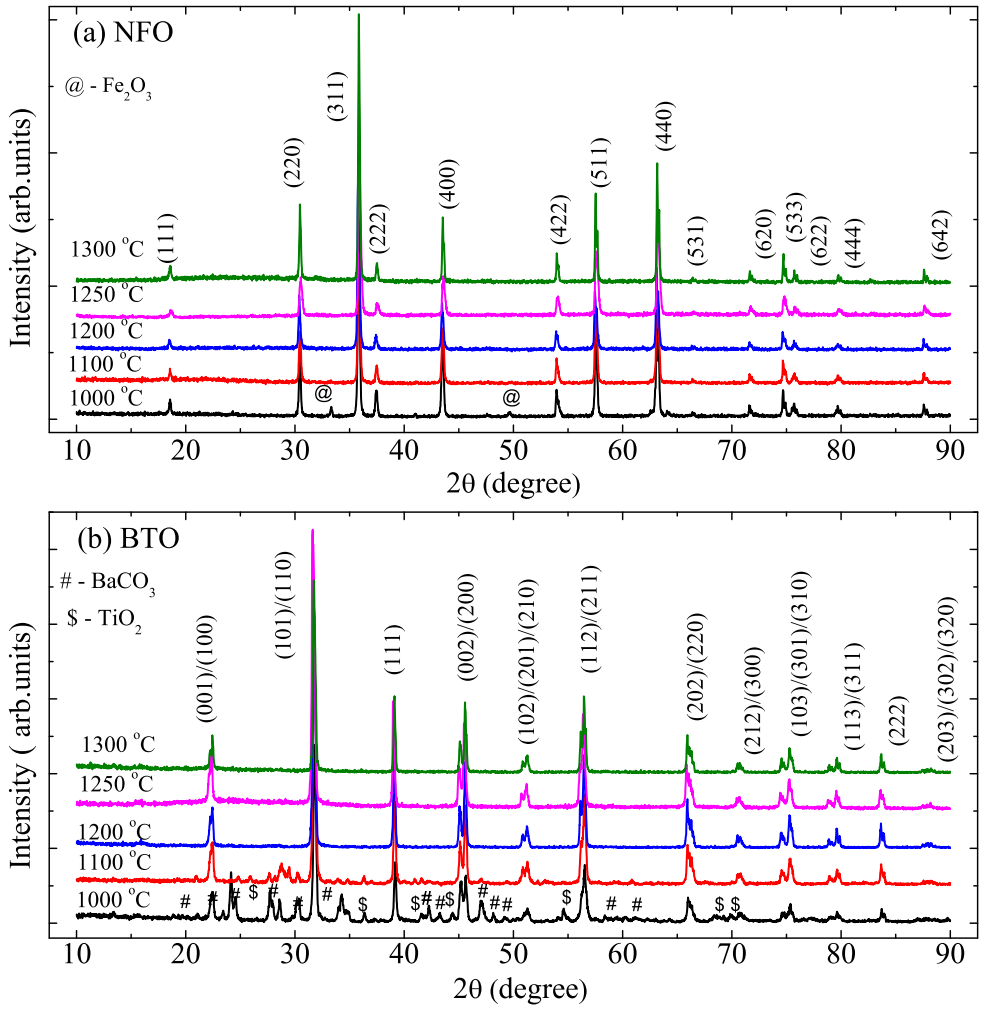

FIGURE 3.5: The x-ray diffraction patterns of (a) NFO and (b) BTO annealed at different temperatures.

The XRD patterns are shown in Fig. 3.6 of NFO−BTO composites, which are sintered at 1350 °C, these measurements were carried out on a circular shape pellets at room temperature. The data were collected by taking the ratio of FWHM of the diffraction peak and step-size. This ratio is found to be 5, which is an agreement

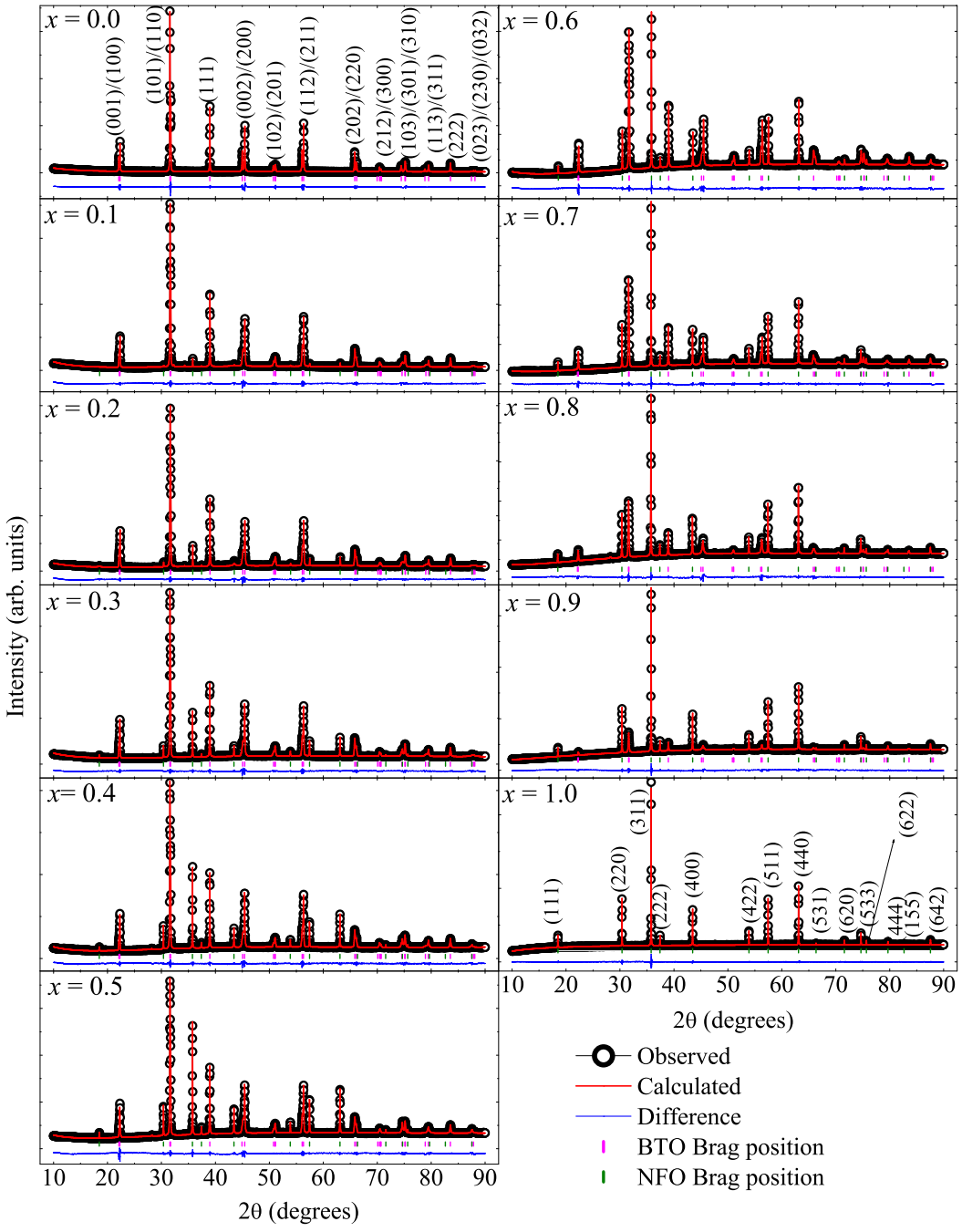

FIGURE 3.6: X-ray diffraction patterns of NFO - BTO composite samples.

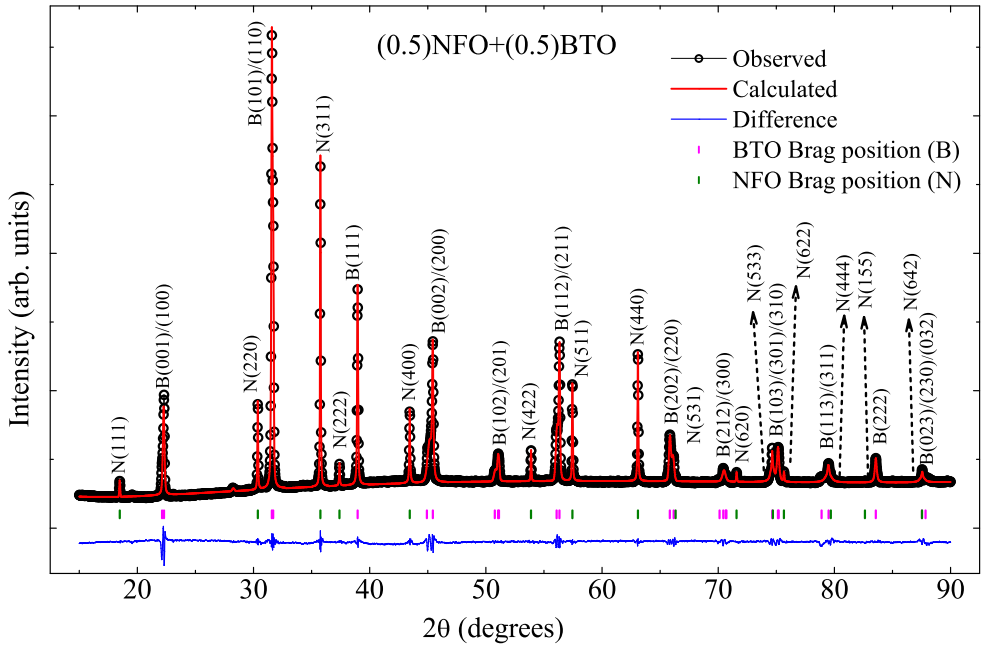

FIGURE 3.7: The x-ray diffraction (experimental, Rietveld refined) patterns of a typical (x = 0.5) composite sample.

parameter for quality data acquisition by any diffractometer. Nevertheless, in composites, the third phase's scope is certainly possible. Also, a systematic variation of intensity of the XRD peaks of individual with increasing NFO content (x) ensures the existence of clear phase separation between constituent phases. The single-phase BTO crystallizes $P4mm$ space group with perovskite "tetragonal" crystal structure and was confirmed when it is compared with ICDD file No. 98-015-4343. In the single-phase BTO, all the diffraction peaks were splitted into doublets other than (111) and (222) peaks. These doublets in the "tetragonal" structure of BTO are corresponding to the $a, c-$ domains. The single-phase NFO crystallizes $Fd\bar{3}c$ space group with inverse spinel cubic crystal structure and was confirmed when it is compared with ICDD file No. 98-019-5820. In the single-phase NFO and BTO, all peaks correspond to the NFO and BTO, respectively, and there is no third phase peak, and all corresponding phase diffraction peaks are represented with (hkl) planes. In the composites, ratios between unknown peak intensities and the known phase's maximum peak intensity are less than 1%. Therefore, it confirms that there is no third phase exists in the composites.

3.2.1 Rietveld Refinement

Rietveld refinement was employed to refine all the samples XRD data using the *High score plus* software. The pseudo-Voigt profile fitting function was used to fit the peaks. The GOF and weight profile (R_{wp}) parameter values for all the samples was found to be less than 2 and 10, respectively, which are acceptable ranges for a good profile fitting. The refined parameters were given in Table 3.1.

TABLE 3.1: Refined crystallographic parameters of single phase (NFO, BTO) and NFO - BTO composite samples.

x	BTO			NFO		R_{exp}	R_p	R_{wp}	GOF
	$a = b$ (Å)	c (Å)	Volume (Å)^3	$a = b = c$ (Å)	Volume (Å)^3				
0.0	3.9938	4.0330	64.33	-	-	5.59	6.53	8.04	1.4
0.1	3.9964	4.0267	64.31	8.3330	578.71	4.70	4.29	5.79	1.2
0.2	3.9965	4.0267	64.31	8.3330	578.81	2.96	4.17	5.58	1.9
0.3	3.9962	4.0268	64.31	8.3348	579.02	2.23	2.96	3.86	1.7
0.4	3.9965	4.0264	64.31	8.3358	579.24	1.87	2.40	3.26	1.8
0.5	3.9966	4.0254	64.30	8.3358	579.23	1.70	2.14	3.04	1.8
0.6	3.9966	4.0258	64.31	8.3358	579.24	1.59	2.12	2.85	1.8
0.7	3.9967	4.0255	64.31	8.3358	579.24	1.42	1.57	2.11	1.5
0.8	3.9977	4.0240	64.32	8.3361	579.29	1.27	1.29	1.82	1.4
0.9	3.9972	4.0240	64.31	8.3360	579.26	1.13	1.33	1.69	1.5
1.0	-	-	-	8.3357	579.21	1.05	0.85	1.33	1.3

3.2.2 Lattice parameters

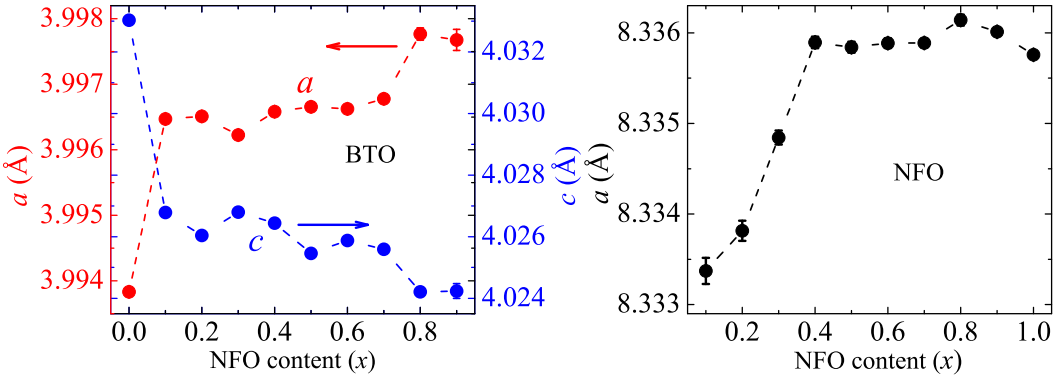

FIGURE 3.8: The variation of lattice parameters of NFO and BTO phases in composites as a function of NFO content (x) (dotted line is the guide to eye).

The single-phase material's lattice parameters are found to be $a = b = 3.9938$ Å, $c = 4.0330$ Å and $a = b = c = 8.3357$ Å for BTO and NFO, respectively. The obtained values are found to match well with reported values [3, 4]. The variation in the lattice parameters as a function x are shown in Fig. 3.8 and are tabulated in Table 3.1. The unit cell of the BTO was found to be expanding along a, b directions and reduction in c direction. Ultimately, the tetragonality (c/a ratio) of BTO was suppressed with ferrite phase increment in composites as shown in Fig. 3.9, whereas Verma et al [5] showed the enhancement in tetragonality with ferrite phase. The unit cell of the NFO was found to expand in all directions. Finally, it is clear for 3.10 the volume of BTO was decreased, and the volume of NFO was enhanced. While NFO content is increasing in composite, NFO unit cell is expanding by suppressing the BTO unit cell.

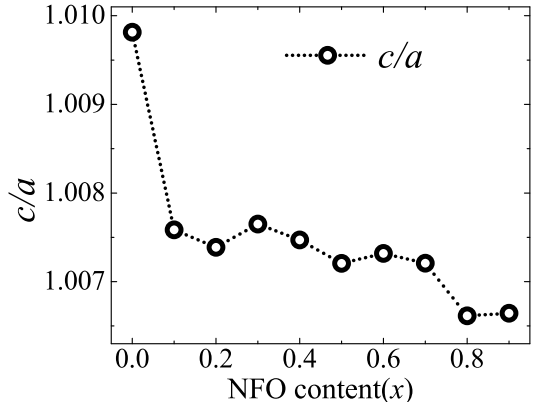

FIGURE 3.9: The variation in tetragonality of BTO phases in composites as a function of NFO content (x) (dotted line is the guide to eye).

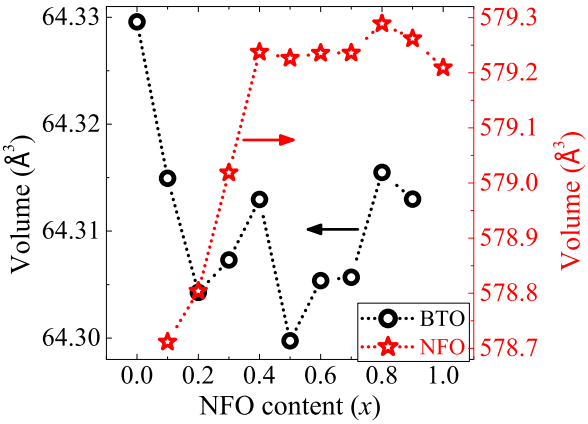

FIGURE 3.10: Volume of BTO and NFO in NFO−BTO composites (dotted line is the guide to eye).

The lattice mismatch values between NFO and BTO grains at the grain interface, when c, $c+a$ and a-domains were found to be 3.2%, 3.7% and 4.2%, respectively. Since the BTO changes its structure from "tetragonal" to "cubic" at 120 °C and contains only "a-domains" in cubic phase. Above 120 °C, the lattice mismatch between NFO and BTO grains is found to be around 1.1%. Therefore, the lattice mismatch between NFO and BTO cannot exceed 4.2% in any case. This lattice mismatch value is found to be sufficiently small for an efficient strain transfer across the hetero-grain interface [6].

3.2.3 Phase percentage

The phase fractions in the composites were calculated by considering the maximum intensity peaks of each phase, i.e. (101) and (311) planes for BTO and NFO, respectively, using the equations 3.3 and 3.4 [5];

$$P_B\% = \left[\frac{I^B_{101}}{I^B_{101} + I^N_{311}}\right] \times 100 \tag{3.3}$$

$$P_N\% = \left[\frac{I^N_{311}}{I^B_{101} + I^N_{311}}\right] \times 100 \tag{3.4}$$

where, P_B and P_N are the percentage of phases in composites. The I^B_{101}, I^N_{311} are the intensities of the BTO (101) and NFO (311) diffraction peaks, respectively. The calculated phase percentages are given in Table 3.2. The calculated phase percentages for the BTO and NFO were found to almost in agreement with the nominal phase percentages. This further confirms the phase purity and accuracy in maintaining the percentage of constituent phases in the composites of the present investigation.

TABLE 3.2: The phase percentage (P_B,P_N), x-ray density (ρ_{xrd}), experimental density (ρ_{exp}), percentage of density (ρ%) and percentage of porosity (P%) values of NFO - BTO composites for different x values.

x	P_B(%)	P_N(%)	ρ_{xrd} (g/cm^3)	ρ_{exp}(g/cm^3)	density(%)	porosity(%)
0	100	0	6.019	5.283	87.8	12.2
0.1	95	5	5.957	5.510	92.5	7.5
0.2	86	14	5.893	5.437	92.3	7.7
0.3	76	24	5.828	5.305	91.0	9.0
0.4	67	33	5.763	5.229	90.7	9.3
0.5	55	45	5.700	5.014	88.0	12.0
0.6	46	54	5.634	5.056	99.7	10.3
0.7	31	69	5.569	5.046	90.6	9.4
0.8	25	75	5.504	5.057	91.9	8.1
0.9	10	90	5.440	4.973	91.4	8.6
1	0	100	5.376	4.898	91.1	8.9

3.3 Density

The density of the samples will depend on the preparation method and sintering temperature used. For ME composites, the quality of the samples is to be at least 85% [7, 8]. The density of the prepared samples was in the acceptable range, and hence the transfer of the strain between heterograins is expected and resulting in a promising ME coupling. Additionally, the dielectric property is also required adequate density for the samples.

3.3.1 The theoretical x-ray density

The theoretical x-ray density (ρ_{xrd}) was calculated using the formula,

$$\rho_{xrd} = \frac{m_w \times N_m}{V \times N_A} \tag{3.5}$$

here, m_w, N_m, V and N_A are the molecular weight, number of molecules per unit cell, volume of the unit cell and Avagadro's number, respectively. The calculated ρ_{xrd} values are given in Table. 3.2. It is interesting to know that the density value of BTO and NFO were found to be in agreement with the data mentioned in ICDD files (BTO :98-015-4343) and (NFO : 98-019-5820), respectively [9, 10]. The values were found to decrease with increase of NFO content (x) in the composites, which is quite logical and expected based on the density values of BTO and NFO.

3.3.2 The experimental (bulk) density

The experimental density (ρ_{exp}) of the samples are measured by the Archimede's principle,

$$\rho_{exp} = \left[\frac{W_{dry}}{W_{dry} - W_{wet}}\right] \times \rho_l \tag{3.6}$$

here, W_{dry} and W_{wet} are the weights of the sample in air and water, respectively. The room temperature water density (ρ_l) is taken as 0.994 g/cm^3 [11]. The measured ρ_{exp} values are given in Table. 3.2 and these values were found to be decrease with increment of NFO content (x) in the composites. The measured bulk density variation with x was found to be in agreement with the x-ray density values. The values of ρ_{exp} were found to be less compared to ρ_{xrd}. It gives a hint that the porosity is existing in the samples.

3.3.3 The percentage of density

The percentage of density (ρ%) was calculated by the formula given below,

$$\rho\% = \frac{\rho_{exp}}{\rho_{xrd}} \times 100 \tag{3.7}$$

The calculated ρ% values are given in Table. 3.2 and these values are found to vary randomly with increment of NFO content (x) in the composites. However, ρ% values of the prepared samples were found to be approximately 90% to theoretical density.

3.3.4 The percentage of the porosity

The percentage of the porosity (P %) was calculated by the equation,

$$P\% = \left[\frac{\rho_{xrd} - \rho_{exp}}{\rho_{xrd}}\right] \times 100 \tag{3.8}$$

The calculated P% values are shown in Table. 3.2. The prepared samples have pores in between the grains, and the porosity was found to be approximately 10%. This porosity was also evidenced by the FESEM images, will be discussed in the next section.

3.4 Scanning electron microscopy analysis

The surface morphology, microstructure, and composition of the samples will be investigated by FESEM in the BSE mode. Figure 3.11 shows the BSE images of all the composites. In the BSE images, FE material grains were seen as bright, and FM material grains are dark. In the previous reports [12, 13], the FESEM images were taken in BSE mode for ferrite−FE composites to know the distribution of individual grains in composites. The atomic number of Ba atom in the FE material is 56; the atomic number of Ni and Fe atoms present in the FM material is 26 and 28, respectively. A well-known fact that the number of backscattered electrons reaching to the detector is proportional to the atomic number [12]. Ultimately, BTO shows bright and NFO revealing a dark contrast difference in the prepared NFO−BTO composite samples. The NFO grains were agglomerated forming clusters in composites. The BTO grains were found to be well separated and smaller in size compared to NFO grains.

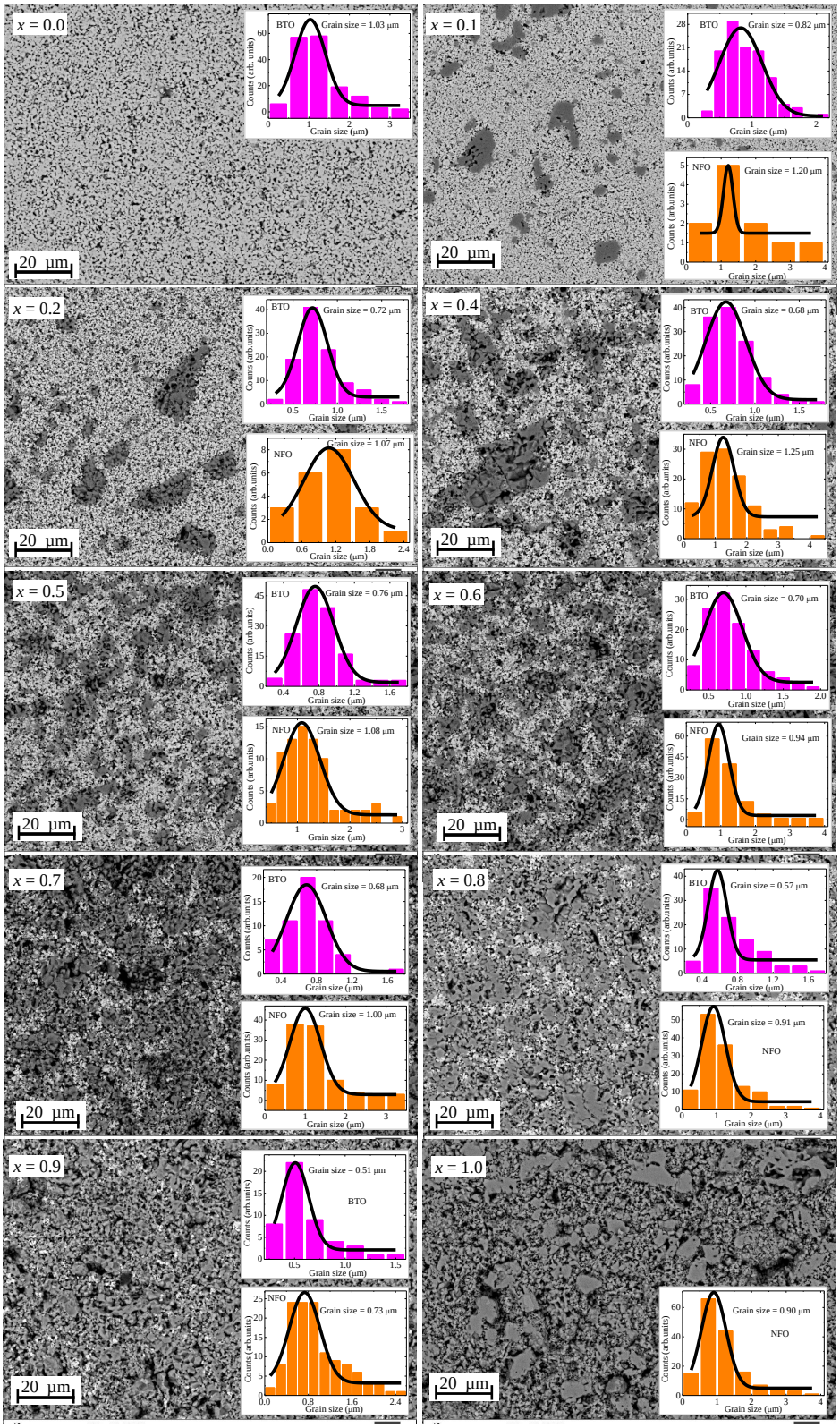

FIGURE 3.11: The back scattered scanning electron micrographs of NFO - BTO composite samples for different x (=0-1). The inset shows the grain size distribution histogram and the solid curve represents Gaussian fit to the data.

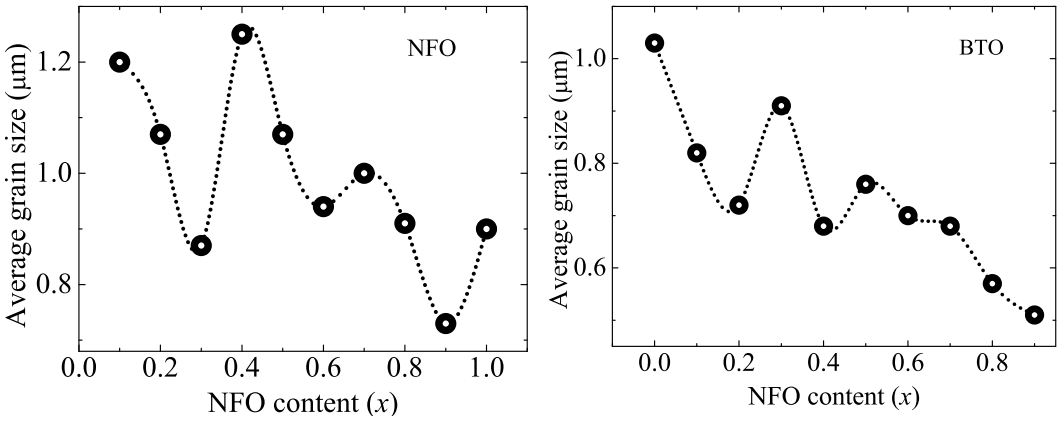

FIGURE 3.12: The average grain size values of NFO and BTO in composites (dotted line is the guide to eye).

In x = 0.1 to 0.4 composites, NFO clusters are surrounded by BTO grains, that means NFO clusters and BTO grains are connected with 0-3 connectivity in composites. The average grain sizes of BTO and NFO were calculated in composites, including single-phase materials. The average grain sizes were taken from fitting of Gaussian function to the histogram of grain size values. These values were found to be 1.5 to 0.8 μm and 1 to 0.5 μm of NFO and BTO, respectively. The grain size values found to be decreasing with an increment of NFO content in composites, shown in Fig. 3.12. This is due to lighter constituent atoms of NFO than BTO, thereby hindering its grain growth. Moreover, increasing NFO content in the composite may obstruct the atoms of BTO to form larger grains. The clustering ability of the NFO is also increasing with the increment of NFO in composites. In the composites, a clear contact interface between NFO and BTO hetero-grains was observed. This confirms that there is no chemical reaction between NFO and BTO grains in composites during the sintering. It enables us to observe the promising ME coupling effect on composites' structural, magnetic, and electric properties thereby transferring strain from BTO to NFO.

3.4.1 Energy dispersive x-ray analysis

It was confirmed from EDXS measurements that brighter grains correspond to BTO, and darker grains represents the NFO. A typical plot in the case of x = 0.5 composite is shown in Fig. 3.13. The EDXS gives the information that measured atomic weight percentages are in close agreement with nominal atomic weight percentages of NFO and BTO phases in composites and single phases.

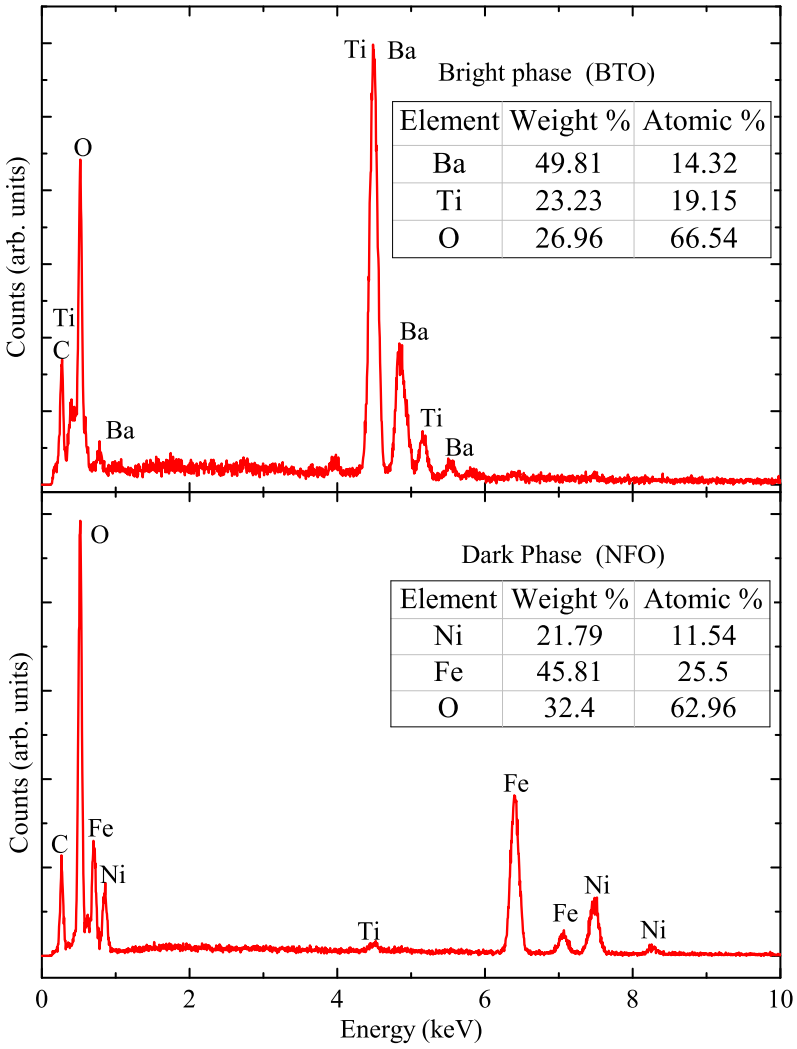

FIGURE 3.13: The EDXS spectrum of BTO (bright) phase and NFO (dark) phase in the 0.5NFO+0.5BTO composite.

3.5 Chapter summary

The single-phase BTO and NFO samples were prepared successfully without any impurity phases by heating at 1200 °C. The BTO and NFO phase formation was started from 700 °C onwards. The XRD data confirms that the composite samples are having no extra peak other than BTO and NFO. The composite samples were prepared successfully with a negligible chemical reaction between them. A systematic lattice parameter variation was observed with NFO/BTO content variation in composites. The bulk density values of the samples were found to be 90%. There is a clear contact interface between NFO and BTO phases, which was confirmed by FESEM measurements. The negligible chemical reaction, less lattice mismatch, clear contact interface, and no dead layer between grains were established from the present investigation to ensure the ME coupling phenomena in composites.

Bibliography

[1] Z. Zhang, Y. Liu, G. Yao, G. Zu, X. Zhang and J. Ma, Physica E **45**, 122 (2012).

[2] V. Berbenni, A. Marini and G. Bruni, Thermochim. Acta, **374**, 151 (2001).

[3] R. Clarke, J. Appl. Crystallogr. **9**, 335 (1976).

[4] A. Ahlawat and V. G. Sathe, J. Raman Spectrosc. **42**, 1087 (2011).

[5] K. C. Verma, M. Singh, R. K. Kotnala and N. Goyal, J. Magn. Magn. Mater. **469**, 483 (2019).

[6] P. Bongurala and V. Gorige, J. Magn. Magn. Mater. **477**, 350 (2019).

[7] A. Kumar, K. C. James Raju and A. R. James, J. Mater. Sci.: Mater. Electron. **29**, 13483 (2018).

[8] T. Santhosh Kumar, A. Kumar, A. R. James and D. Pamu, J. Aust. Ceram. Soc. **47**, 44 (2011).

[9] W. G. Marshall, K. R. Whittle, M. G. Tucker, H. J. Stone, S. A. Redfern and S. A. Hayward, Zeitschrift fuer Kristallographie **220**, 735 (2005).

[10] Y. Al-Douri, A. Zanoun, A. Addou, K. Taibi and A. Rais, Ceram. Int. **40**, 14413 (2014).

[11] L. W. Tilton and J. K. Taylor, J. Res. Natl. Bur. Stand. **18**, 205 (1937).

[12] J. Shen, Y. Bai, J. Zhou and L. Li, J. Am. Ceram. Soc. **88**, 3440 (2005).

[13] Y. Bai, J. Zhou, Y. Sun, B. Li, Z. Yue, Z. Gui and L. Li, Appl. Phys. Lett. **89**, 112907 (2006).

Chapter 4

Structural properties of NFO−BTO composites

The BTO has three different structures in FE phase with transitions from "rhombohedral" to "orthorhombic" to "tetragonal" to "cubic" at 190 K, 280 K, and 393 K, respectively [1]. The change in the structure of BTO in the FE phase will have an influence on the NFO structural parameters and vice versa. These interdisciplinary structural changes of the constituent phase, on the other, can be experimentally observed by the XRD and Raman spectroscopy techniques by varying the temperature.

In this chapter, XRD and Raman measurements were carried out in different structural phases of BTO. It was observed that changes in the structure of BTO induce the lattice strain on the NFO structural parameters, cation distribution, and magnetic properties, and the underlying mechanism was discussed.

4.1 Temperature-dependent x-ray diffraction

4.1.1 $BaTiO_3$

The XRD measurements were carried out for single-phase BTO ($x = 0$) at four different temperatures of BTO, viz., 150 K, 230 K, 300 K, and 570 K for "rhombohedral", "orthorhombic", "tetragonal", and "cubic" structures, respectively. The XRD patterns corresponding to the mentioned phases of BTO are shown in Fig. 4.1. At first, the measured XRD data and peak positions at different temperatures were compared with ICDD files. Remarkably, it was found that all the diffraction patterns were found to match well with the corresponding phase ICDD files (with Nos: 98 - 009 - 5437, 98 - 007 - 3646, 98 - 006 - 6482, and 98 - 031 - 0174, respectively for "cubic", "tetragonal", "orthorhombic" and "rhombohedral" phases of BTO). It is also clear from the patterns that except 150 K (rhombohedral) data, no other XRD patterns show secondary peaks. The XRD pattern measured at 150 K consist of additional peaks other than BTO peaks and were marked with the # symbol in Fig. 4.1. The identified second phase corresponds to the crystalline ice (H_2O) formed at low-temperature (< 200 K). The secondary phase peaks were well analyzed by comparing the reported literature [2]. In the present investigation, the mentioned phase arises due to vacuum-related issues in the instrument's measurement chamber.

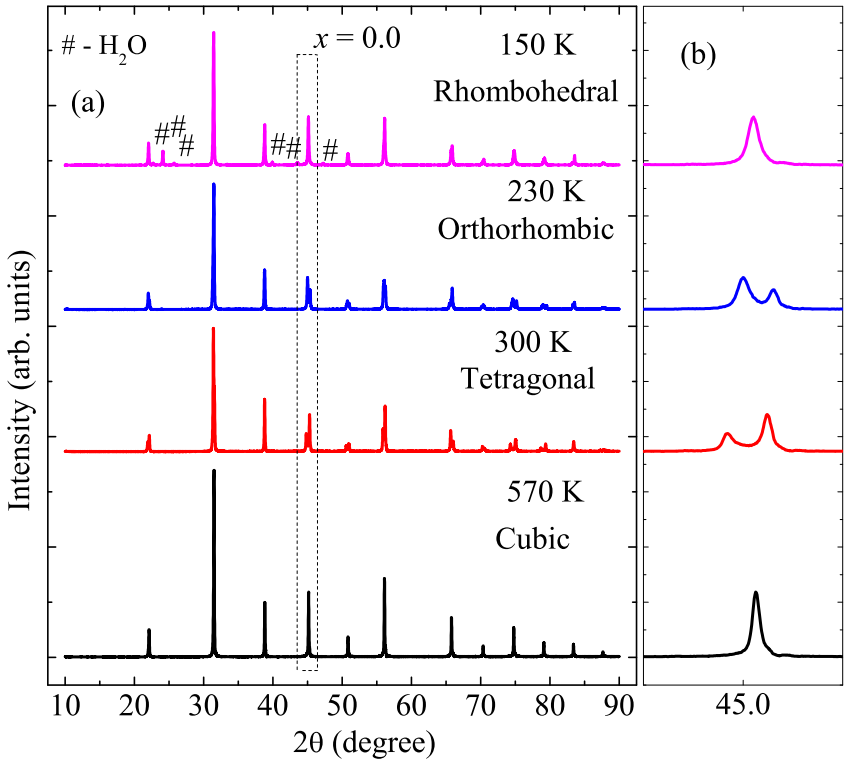

FIGURE 4.1: (a) XRD patterns of BTO measured at 150, 230, 300 and 570 K temperatures and (b) enlarged view of the peak present at $2\theta \sim 45°$.

A careful observation of Fig. 4.1(b) reveals that the splitting of diffraction peaks observed for the "tetragonal" and "orthorhombic" phase of BTO. The observation clearly indicates the coexistence of lattice domains with different orientations (eg., *a*-domain and *c*-domains in tetragonal phase) [3].

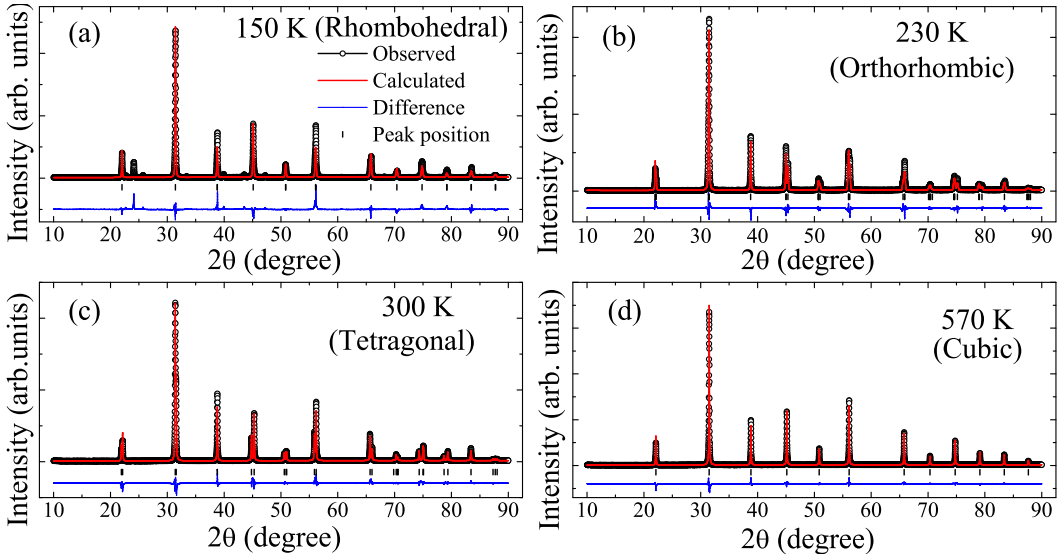

FIGURE 4.2: The Rietveld refinement XRD patterns of BTO ($x = 0$) at four different structural phases.

The Rietveld refinement was done for the measured XRD patterns of BTO by

using *High score plus* software, and the refined patterns are shown in Fig. 4.2. The refined structural parameters are given in Table 4.1. The refinement was done by assuming $Pm\bar{3}m$, $P4mm$, $Pmm2$ and $R\bar{3}m$ space groups for the data measured at temperatures 570 K, 300 K, 230 K, and 150 K, respectively. Residual indices and the factor χ^2, which is an indication of how good the fitted model accounts for the experimental data, are found to well within the acceptable range. The refined lattice parameters from XRD analysis are shown in Fig. 4.3. The lattice parameters in the four phases are in good agreement with literature [4, 5]. While cooling the sample from above room temperature (570 K) to lower temperatures, cubic ($a = b = c$) BTO structure undergoes structural change at 393 K thereby transforming into tetragonal structure by elongating in $c-$direction and suppressing in $a, b-$directions, resulting in $a = b \neq c$. On further cooling the sample, the tetragonal structure undergoes an orthorhombic structure as per the relation between the lattice parameters $a \neq b \neq c$. Further cooling, makes the sample to transform from orthorhombic structure to rhombohedral structure with $a = b = c$ and $\alpha = \beta = \gamma \neq 90°$.

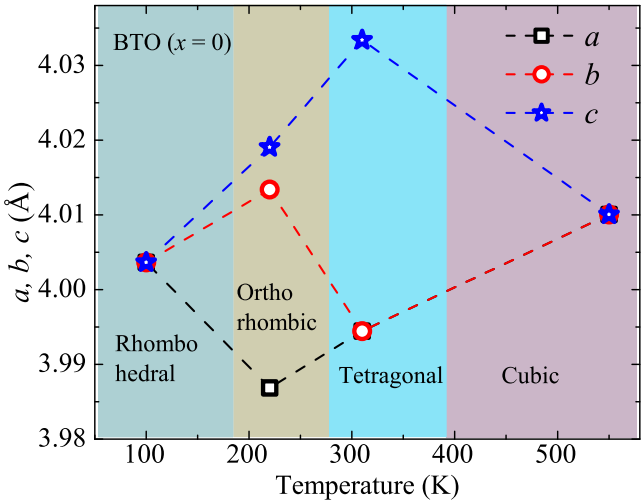

FIGURE 4.3: The variation lattice parameters of BTO with respective temperature (dotted line is the guide to eye).

TABLE 4.1: The Rietveld refined crystallographic parameters of BTO.

Temp.(K)	a (Å)	b (Å)	c (Å)	R_{exp}	R_p	R_{wp}	GOF
150	4.00364	4.00364	4.00364	5.49	17.19	24.93	4.5
230	3.98685	4.01339	4.01904	5.61	11.69	15.51	2.8
300	3.99445	3.99445	4.03339	9.83	10.22	13.23	1.4
570	4.01005	4.01005	4.01005	9.28	08.90	10.90	1.2

4.1.2 $NiFe_2O_4$

The XRD measurements were carried out for single-phase NFO (x = 1) at four different temperatures viz., 150 K, 230 K, 300 K, and 570 K for "rhombohedral", "orthorhombic", "tetragonal", and "cubic" structures, respectively. The XRD patterns corresponding to the mentioned phases of BTO are shown in Fig. 4.4. The XRD pattern was measured at different temperatures, and their peak positions were compared with the ICDD file with number 98-024-6894. It was found that the measured XRD data matches well with the cubic in structure. There are no secondary peaks other than corresponding NFO peaks. The XRD patterns measured at 150 K consist of secondary peaks corresponding to crystalline ice and are marked with the # symbol in Fig. 4.4. The Rietveld refinement of the XRD data was done for the NFO sample, and corresponding plots are shown in Fig. 4.6. The refined structural parameters are given in Table 4.2. The NFO crystallizes in "cubic" structure with $Fd\bar{3}m$ space group. The variation of the lattice parameter of NFO with increasing temperature is shown in Fig. 4.5, and it was found that the lattice parameter increases with an increase in temperature. The increase in lattice parameters with an increment of temperature is attributed to tensile stress [6, 7, 8]. The obtained lattice parameter values are in concurrence with the reported values [5].

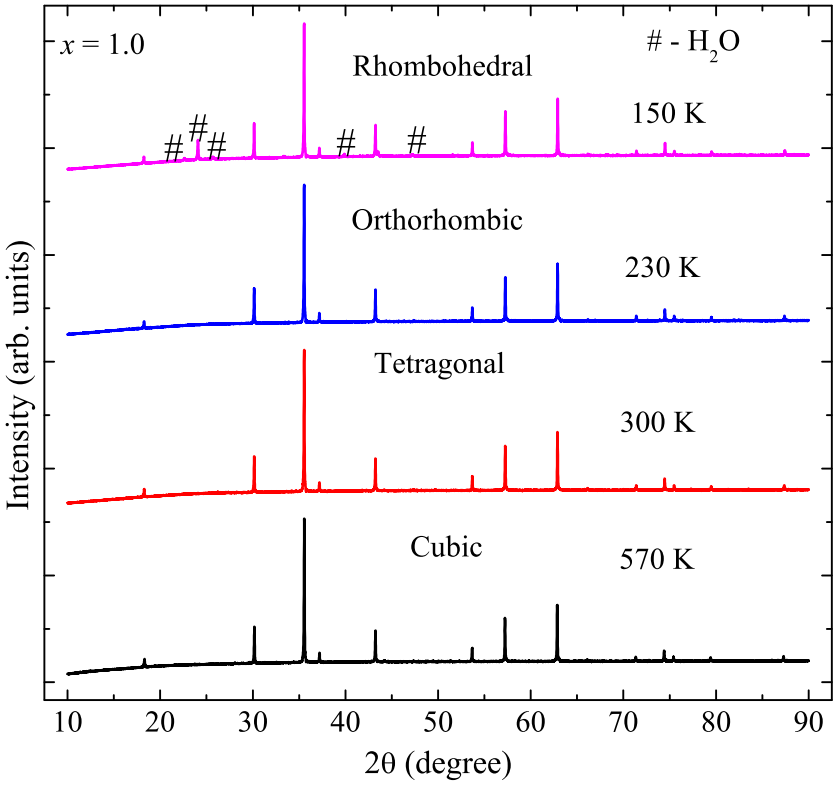

FIGURE 4.4: The XRD patterns of NFO at obtained 150, 230, 300 and 570 K temperatures.

TABLE 4.2: The Rietveld refined crystallographic parameters of NFO sample at different temperatures.

Temp.(K)	a (Å)	R_{exp}	R_p	R_{wp}	GOF
570	8.34738	2.57	1.62	3.38	1.31
300	8.33744	2.59	1.83	3.38	1.30
230	8.33478	2.60	1.79	2.78	1.1
150	8.33103	1.39	1.90	3.77	2.7

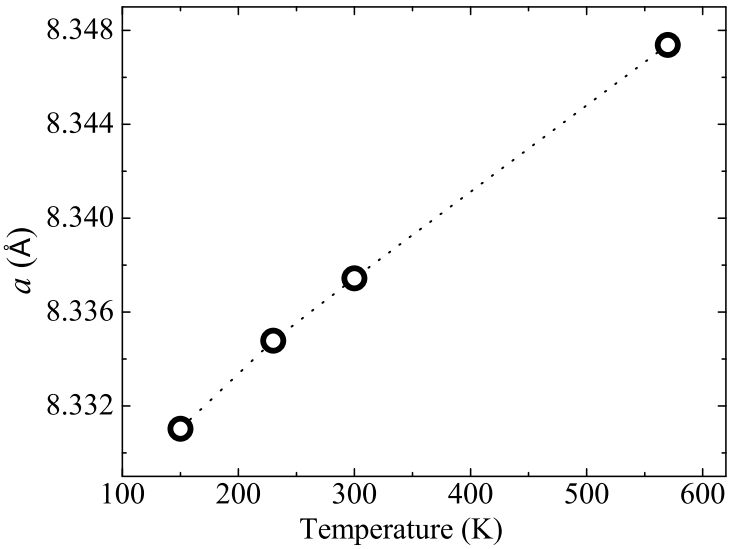

FIGURE 4.5: The variation of lattice parameter of NFO with temperature (dotted line is the guide to eye).

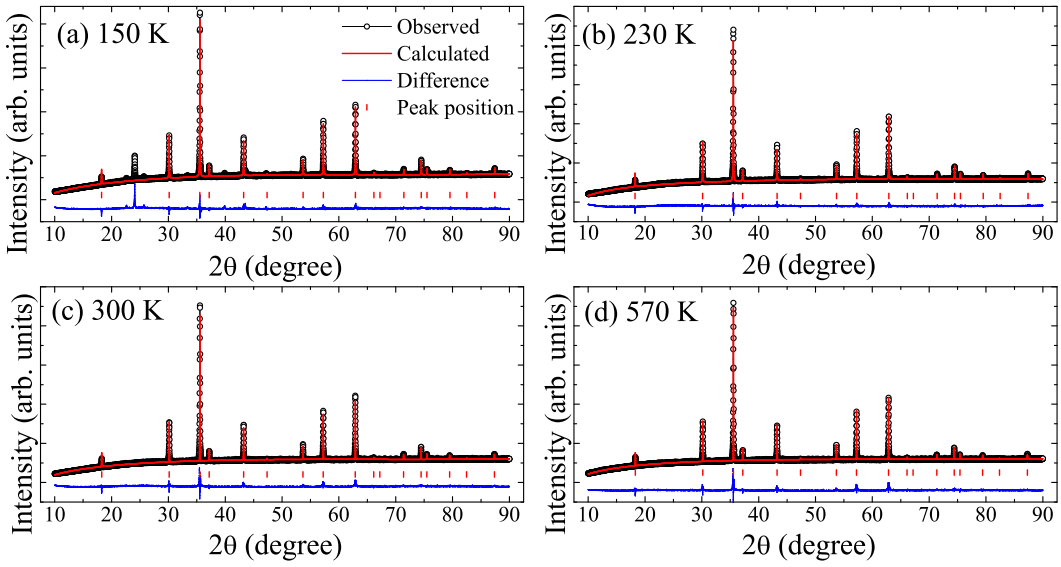

FIGURE 4.6: The Rietveld refinement patterns of NFO (x = 1) at measured different temperatures.

4.1.3 $BaTiO_3 - NiFe_2O_4$ composites

The XRD measurements of x = 0.2, 0.4, 0.6 and 0.8 composites were carried out at four temperatures viz., 150 K, 230 K, 300 K and 570 K. The obtained patterns are shown in Fig. 4.7. No diffraction peaks other than BTO and NFO were detected in the patterns. With a view to obtaining more structural and lattice strain information of these composites, the data were refined by using *High score plus* software. The refined patterns are shown in Figs. 4.8 and 4.9 and the refined crystal parameters are given in Table 4.3. The values of residual parameters were found to be within the acceptable limit. The refined lattice parameters for BTO and NFO phases in composites at four different temperatures were obtained and are tabulated in Table 4.3. The lattice parameters of BTO and NFO in composites were found to be higher compared to end compounds (individual phases). The lattice parameters were found to increase with an increase in temperature for both BTO and NFO phases in composites. The observed behavior may be attributed to the enhanced tensile stress in the samples [6, 7, 8]. In fact, due to the same reason, the unit cell volume of these phases is increasing.

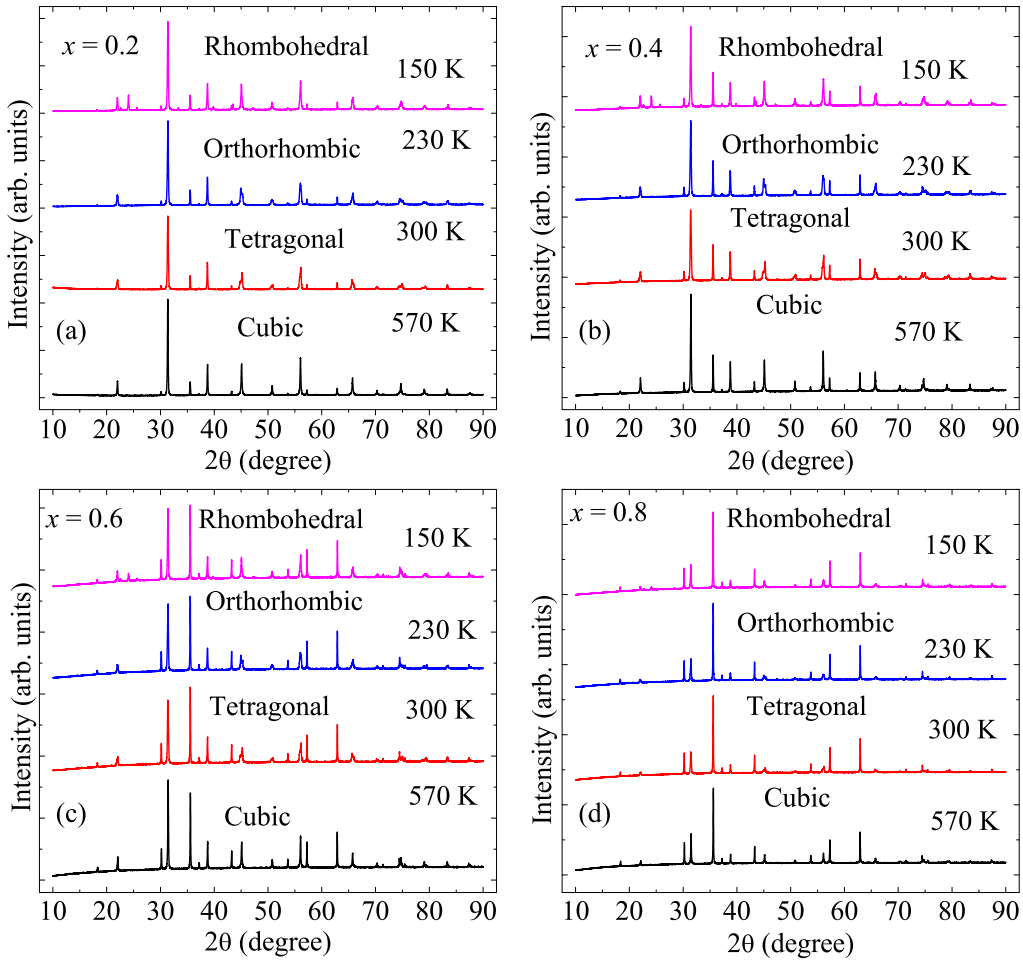

FIGURE 4.7: The XRD patterns of NFO −BTO for x= 0.2, 0.4, 0.6 and 0.8 composites at 150 K, 230 K, 300 K and 570 K temperatures.

TABLE 4.3: The Rietveld refined crystallographic parameters of NFO −BTO composites for x = 0.2, 0.4, 0.6 and 0.8 at different temperatures.

x	T(K)	BTO			NFO	R_{exp}	R_p	R_{wp}	GOF
		a (Å)	b (Å)	c (Å)	a (Å)				
0.2	570	4.0107	4.0107	4.0107	8.3459	6.84	6.59	9.97	1.5
	300	3.9985	3.9985	4.0264	8.338	7.20	4.84	7.10	1.1
	230	3.9901	4.0086	4.0194	8.3340	3.74	6.22	8.49	2.3
	150	4.0049	4.0049	4.0049	8.3319	3.73	7.18	13.24	3.5
0.4	570	4.0111	4.0111	4.0111	8.3467	5.62	4.86	7.16	1.3
	300	3.9981	3.9981	4.0284	8.3389	5.71	4.25	6.40	1.1
	230	3.9903	4.0102	4.0201	8.3361	3.01	4.01	5.70	1.9
	150	4.0057	4.0057	4.0057	8.3337	3.02	6.25	11.15	3.7
0.6	570	4.0105	4.0105	4.0105	8.3449	4.27	3.06	4.93	1.2
	300	3.9978	3.9978	4.0275	8.3374	4.31	2.94	4.62	1.1
	230	3.9904	4.0100	4.0193	8.3348	2.27	2.60	3.71	1.6
	150	4.0047	4.0047	4.0047	8.3318	2.29	4.42	7.91	3.4
0.8	570	4.0108	4.0108	4.0108	8.3452	3.32	2.12	3.67	1.1
	300	3.9985	3.9985	4.0275	8.3378	3.34	2.17	3.75	1.2
	230	3.9909	4.0106	4.0192	8.3350	1.76	1.78	2.52	1.4
	150	4.0051	4.0051	4.0051	8.3321	1.77	2.25	3.53	2.0

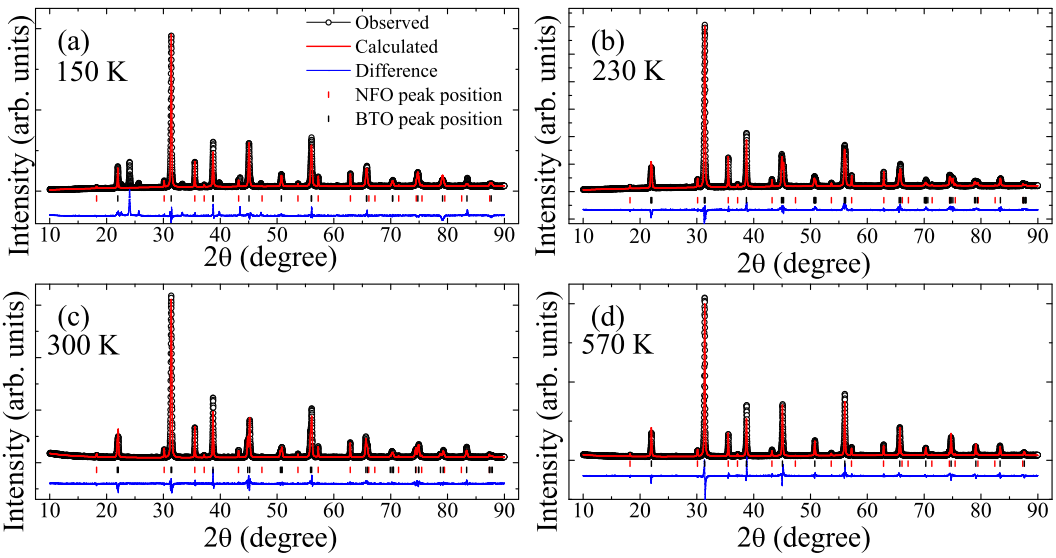

FIGURE 4.8: Rietveld refined XRD patterns of NFO−BTO for x = 0.2 composite at different temperatures.

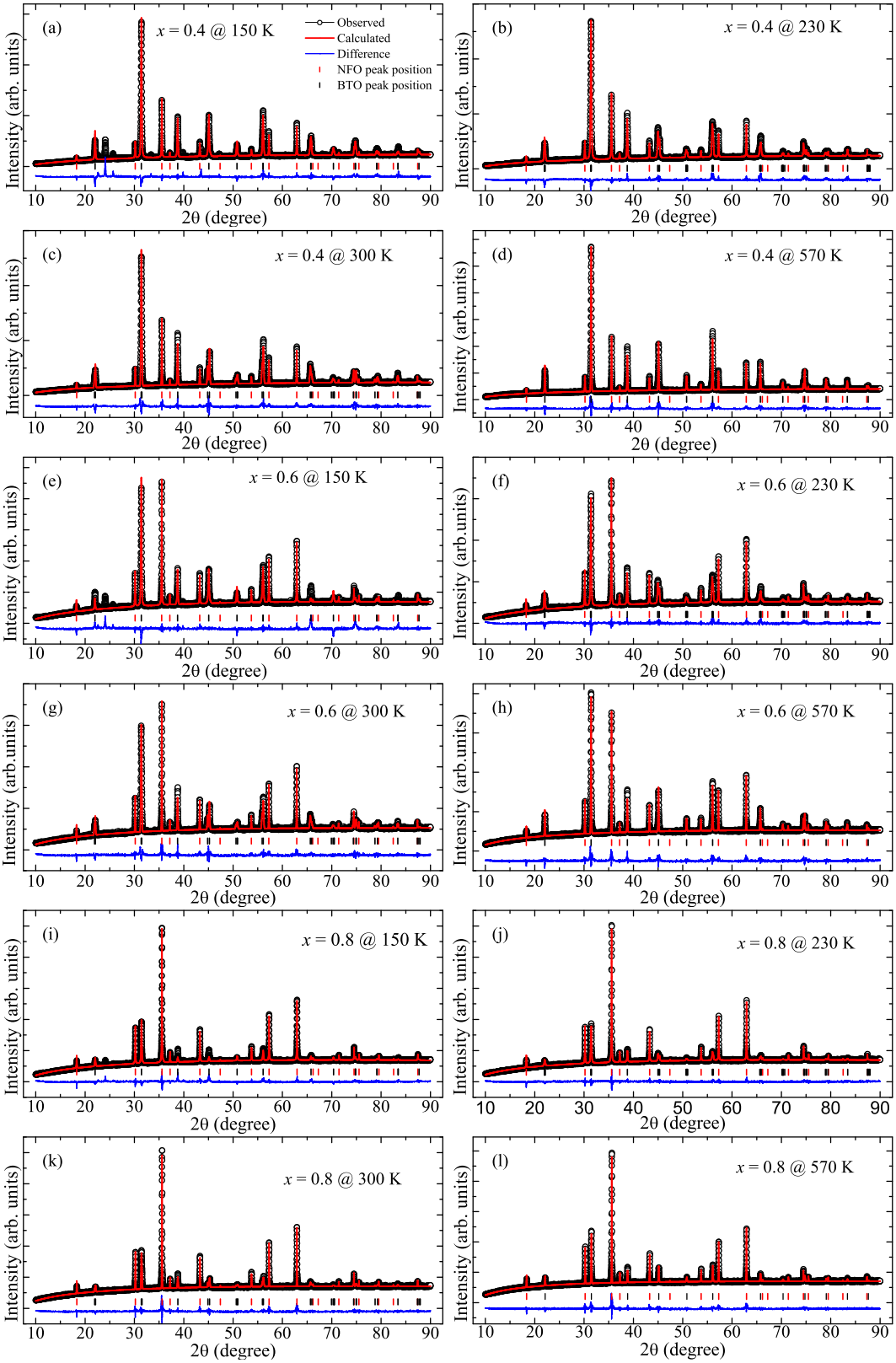

FIGURE 4.9: The Rietveld refined XRD patterns of NFO −BTO for x = 0.4, 0.6 and 0.8 composite at different temperatures.

4.1.4 Lattice strain

With a view to invest the effect of lattice strain from BTO on the NFO phase, the volume strain of the BTO and NFO was calculated by using unit cell volumes for the distinct structural phases of BTO. The V_c, V_T, V_O, and V_R are the unit cell volumes in "cubic", "tetragonal", "orthorhombic", and "rhombohedral" phases of BTO, respectively. The following formula gives the percentage of volume strain,

$$Strain\% = \frac{\Delta V}{V_c} = \frac{V_c - V}{V_c} \times 100 \tag{4.1}$$

The calculated strain values in percentage were given in Table 4.4. The percentage of strain generated in BTO was found to increase with a decrease in temperature, i.e., the structure of BTO changes from "cubic" to "tetragonal" to "orthorhombic" to "rhombohedral". The percentage of lattice strain in BTO is small compared to the NFO phase. That means, a considerable strain from BTO influences the NFO lattice and hence considerable change in physical properties of NFO are expected.

TABLE 4.4: The lattice strain ($\times 10^{-4}$) values of NFO−BTO composites for x = 0, 0.2, 0.4, 0.6, 0.8 and 1 samples at different temperatures, corresponding to different ferroelectric phases of BTO.

T(K) \ x	0	0.2		0.4		0.6		0.8		1
	BTO	BTO	NFO	BTO	NFO	BTO	NFO	BTO	NFO	NFO
150	16.0	14.5	16.8	13.6	15.6	14.0	15.9	14.3	15.7	19.6
230	9.1	11.5	14.2	10.6	12.6	9.4	12.0	9.9	12.2	15.1
300	6.5	7.2	9.5	7.3	9.3	6.6	9.0	6.7	8.8	11.9

4.1.5 Cation distribution

To understand the effect of the lattice strain of BTO on the physical properties of NFO, the cationic arrangement between "tetrahedral" and "octahedral" sites of NFO is crucial. Therefore, the cation distribution of NFO has been estimated from the intensities of the XRD pattern of the selected reflections. In this case, (220), (400), and (440) planes were considered to calculate the cation arrangement in NFO [9]. These planes' intensity ratios were calculated theoretically and compared with experimentally measured intensity ratios based on the following relation.

$$\frac{I^{exp}_{hkl}}{I^{exp}_{h'k'l'}} = \frac{I^{cal}_{hkl}}{I^{cal}_{h'k'l'}} \tag{4.2}$$

Here, I^{exp}_{hkl}, I^{cal}_{hkl} are the experimental and theoretical intensities of corresponding (hkl) plane. Theoretical intensities were calculated by following procedure [9, 10, 11].

$$I^{cal}_{hkl} = |F_{hkl}|^2 N L_p \tag{4.3}$$

Here, $|F_{hkl}|, N$ and L_p are the "structure factor", "multiplicity factor" and "Lorentz polarization factor". The multiplicity factor values were taken from the literature [12]. Lorentz polarization factor was defined as

$$L_p = \frac{1 + cos^2 2\theta_{hkl}}{sin^2\theta_{hkl} cos\theta_{hkl}} \tag{4.4}$$

Here, θ_{hkl} is XRD angle of corresponding (hkl) plane. The structure factor can be define as

$$F_{hkl} = \sum f.e^{-M} \tag{4.5}$$

Here, e^{-M} is the Debye–Waller factor, f is the scattering factor and it is defined as

$$\sum f = \sum_{i=1}^{3} a_i e^{\frac{-b_i sin^2\theta_{hkl}}{\lambda^2}} + c \tag{4.6}$$

Here, a, b and c are considered from the international crystallographic tables [13]. λ is a wave length of x-rays. In the Debye−waller factor, M can be defined as

$$M = \frac{6h^2T}{mk\theta_D^2}[\psi(x) + \frac{x}{4}]\frac{sin^2\theta}{\lambda^2} \tag{4.7}$$

Here, h, T, k, θ_D, x, are the Plank's constant, temperature at which the measurement is made, Boltzmann constant, Debye temperature and $x = \frac{\theta_D}{T}$, respectively. The m can be defined $m = \frac{A}{N_A}$, A, N_A are atomic weight and Avagadro's number, respectively. In the above equation, $\psi(x) + \frac{x}{4}$ was calculated by using the procedure given by James in his book [10]. The Debye temperature values were taken as 378 K and 357 K for A and B sites, respectively [14].

The cation distribution (y) of the prepared samples was calculated using the measured XRD data at different temperatures [9, 10, 14]. It was found that the value of y is found to be zero. It indicates that the Ni ion percentage in the tetrahedral site found to be zero in the NFO crystal structure. That means the Ni ions are present only in the octahedral site.

$$[Ni_yFe_{1-y}]_T[Ni_{1-y}Fe_{1+y}]_OO_4 \tag{4.8}$$

Ni ion percentage at tetrahedral site has zero (i.e. y = 0)

$$[Ni_0Fe_{1-0}]_T[Ni_{1-0}Fe_{1+0}]_OO_4 \tag{4.9}$$

$$[Fe]_T[NiFe]_OO_4 \tag{4.10}$$

The calculated magnetic moment based on the above cation distribution is 2 $\mu_B/f.u.$, which is in concurrence with reported in the literature [9]. The magnetic moment value calculated from XRD will be compared with the magnetic moment calculated from magnetization measurements in the next chapter of the thesis.

4.2 Raman spectroscopy

4.2.1 $BaTiO_3$

The Raman spectroscopic analysis is an excellent technique to study the structural and vibrational phononic information of atoms, thereby predicting the nature of the physical properties. The single-phase BTO exhibits fifteen Raman vibrational modes. Seven vibrations are infrared active ($3A_1 + 4E$) and eight vibrations are Raman active ($3A_1 + B_1 + 4E$) [15]. In the present investigation, the possible Raman modes are schematically represented and are shown in Fig. 4.10.

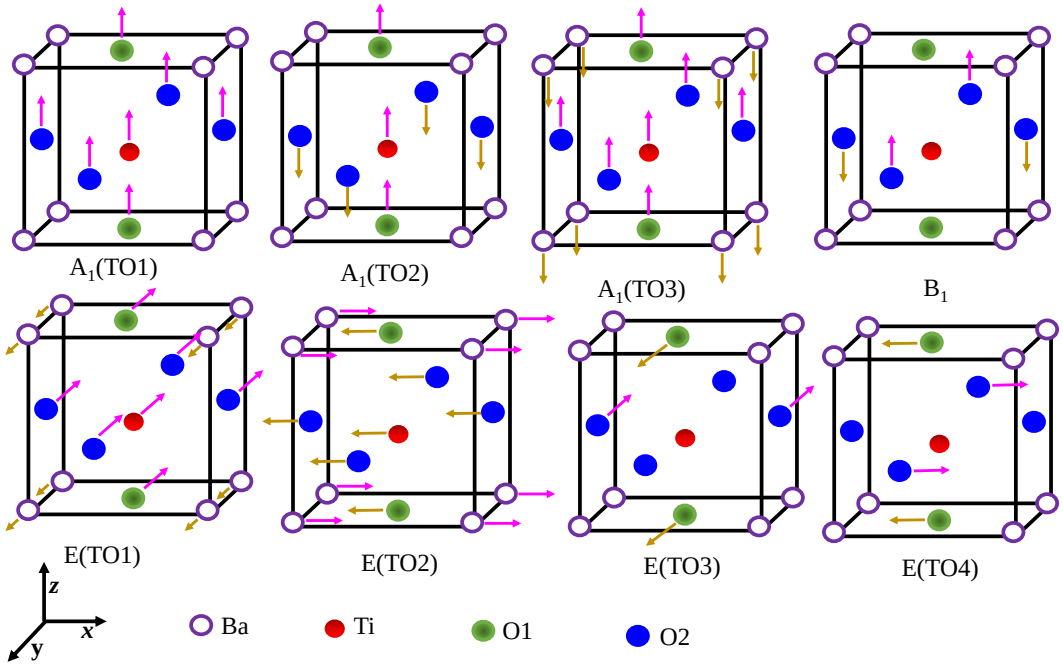

FIGURE 4.10: The schematic representations of possible vibrational Raman modes of atoms in BTO, modified after[15](2015, Chinese Chemical Society).

The A_1(TO1), B_1 modes represent the atomic vibrations in $z-$direction and E mode represents in $x, y-$directions. The A_1(TO1) mode refers that the Raman shift arising due to the vibration of six oxygen atoms and titanium atom when the barium is fixed [15]. The A_1(TO2) mode refers to the Raman shift arising due to O1 atom and titanium atom vibrations with respect to O2 atoms [15]. The A_1(TO3) mode refers to the Raman shift arising due to the vibration of six oxygen atoms; titanium atom is vibrating opposite to the barium atoms [15]. The B_1 mode refers to the perpendicular plane of O2 atoms are vibrating against each other [15]. The E(TO1) mode refers to the Raman shift arising due to six oxygen atoms, and the titanium atom is vibrating opposite to the barium atoms in $y-$direction [15]. The E(TO2) mode represents the Raman shift due to oxygen atoms and titanium atom vibrating opposite to the barium atoms in the $x-$direction. The E(TO3) and E(TO4) modes arise due to

two of the O2 atoms that are vibrating concerning O1 atoms in the $y, x-$directions, respectively [15].

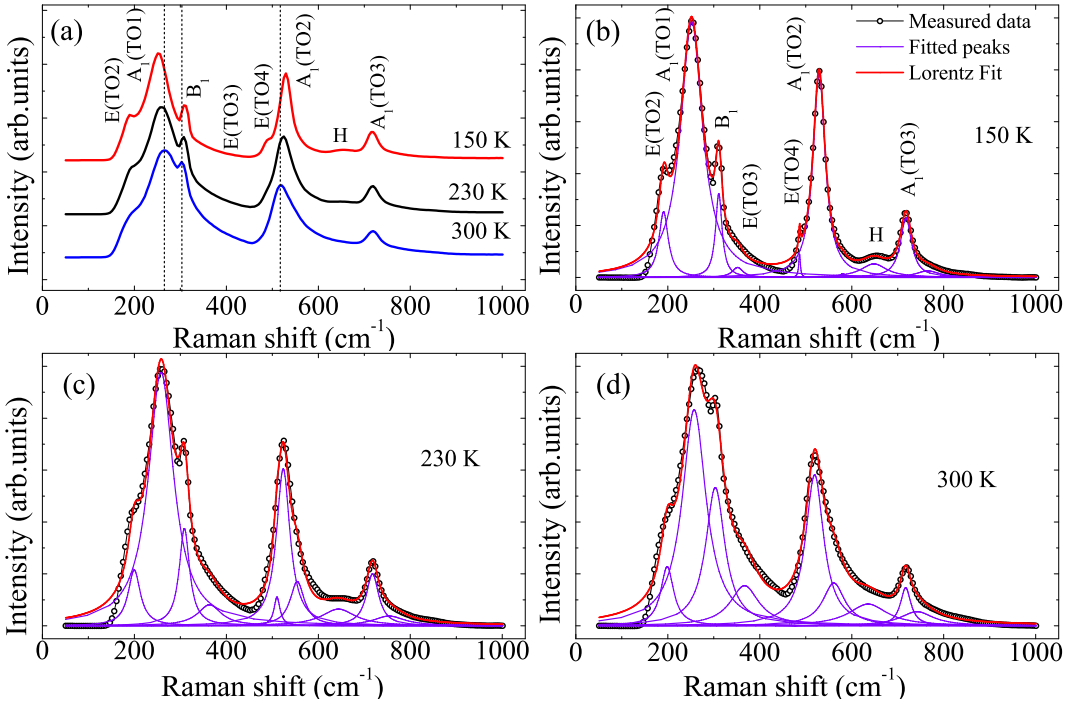

FIGURE 4.11: The vibrational Raman spectrum of BTO ($x = 0$) sample at different temperatures and the solid red line represents the deconvoluted specral peaks fitted with Lorentzian curve.

In the present investigation, the Raman spectrum of BTO was obtained at three different FE phases of BTO at the temperatures 150, 230, and 300 K, shown in Fig. 4.11a. The single-phase BTO exhibits the seven Raman active modes, which are E(TO2), A_1(TO1), B_1, E(TO3), E(TO4), A_1(TO2) and A_1(TO3) at 190, 251, 310, 351, 486, 529 and 717 cm^{-1} respectively. The observed peak positions of the Raman modes are in concurrence with the earlier reported data [16]. Generally, the peak position represents the energy associated with the vibrating atom with corresponding frequency (Raman shift), which is supplied here in the form of photon energy [17]. The A_1(TO1) mode is showing a shift in the frequency towards the lower frequency side with decreasing the temperature, which indicates the decrease in tensile stress in the mode direction [18, 19]. The B_1 and A_1(TO2) modes are showing a shift in the frequency for the higher frequency with decreasing the temperature, which attributes the compressive stress in the mode direction. In the E(TO2), E(TO4), and A_1(TO3) modes, there is no significant shift in frequency with temperature. The E(TO4) mode is not present in the Raman spectrum measured at 300 K; however, it appears for 230 K and 150 K temperatures. This observation is signifying a clear structural change in the BTO with a change in temperature [20].

A small and broad peak observed at 650 cm^{-1} originates from the hexagonal phase of BTO, which was observed at the 230 K and 150 K temperature. It becomes significant with the decrease in temperature [20, 21]. A negligible percentage of the

TABLE 4.5: The possible Raman mode positions (cm^{-1}) of BTO in NFO−BTO composites at different temperatures.

x	Temp.(K)	E(TO2)	A_1(TO1)	B_1	E(TO3)	E(TO4)	A_1(TO2)		H	A_1(TO3)	
0	150	190.88	251.71	310.90	351.80	486.42	529.04	560.34	648.23	717.87	765.24
	230	199.70	258.06	308.82	363.50	510.11	523.71	554.22	643.93	717.77	753.97
	300	198.70	257.37	303.25	366.93	476.99	519.29	561.05	635.47	717.24	741.53
0.1	150	194.30	256.39	308.64	352.29	489.24	524.73	559.27	645.88	716.62	744.02
	230	199.33	253.34	302.27	362.42	485.82	518.83	563.50	637.86	716.03	757.50
	300	193.03	250.74	302.82	369.28	483.19	510.86	551.38	627.11	711.32	738.20
0.2	150	198.57	256.08	308.63	390.91	480.00	522.02	552.47	649.34	715.13	739.30
	230	197.71	254.72	302.31	360.67	504.27	521.79	553.76	635.21	716.53	744.69
	300	199.58	252.76	303.27	380.91	497.86	514.74	568.81	639.92	713.18	740.96
0.3	150	190.61	257.52	304.33	367.63	486.21	525.64	557.15	648.23	711.63	741.75
	230	221.34	260.41	301.11	343.30	490.18	518.89	551.04	650.00	706.88	721.69
	300	191.28	252.67	300.72	354.99	488.36	515.73	555.47	632.01	702.88	719.11
0.4	150	202.43	258.56	307.07	364.20	501.90	525.14	554.12	616.28	719.01	816.99
	230	205.98	258.32	306.05	362.79	481.77	517.50	559.77	627.37	714.45	734.63
	300	202.82	253.92	303.28	362.53	472.70	508.94	560.18	651.87	702.40	718.91
0.5	150	203.39	257.35	305.69	365.22	489.19	523.83	567.61	662.92	702.76	720.92
	230	198.07	259.69	307.61	363.74	495.75	520.77	580.50	658.82	711.01	733.23
	300	213.75	255.91	302.95	366.13	496.44	514.97	570.72	647.50	706.12	733.42
0.6	150	189.01	256.07	310.05	342.60	497.42	530.78	584.79	663.39	713.81	739.02
	230	194.89	257.56	305.80	351.01	489.54	523.60	574.74	653.12	709.26	726.78
	300	195.99	249.72	299.74	352.35	424.70	500.99	566.10	645.92	697.07	715.80
0.8	150	191.98	254.11	306.05	-	-	523.94	-	-	-	-
	230	196.93	257.21	304.28	-	-	-	-	-	-	-
	300	201.17	255.40	299.39	-	-	-	-	-	-	-
0.9	150	199.11	260.20	308.40	-	-	528.41	-	-	-	-
	230	-	-	305.02	-	-	-	-	-	-	-
	300	203.33	255.14	298.33	-	-	-	-	-	-	-

TABLE 4.6: The FWHM (cm^{-1}) of BTO in NFO−BTO composites at different temperatures.

x	Temp.(K)	E(TO2)	A_1(TO1)	B_1	E(TO3)	E(TO4)	A_1(TO2)		H	A_1(TO3)	
0	150	24.66	58.16	17.25	28.58	4.37	32.42	15.10	68.47	29.32	61.30
	230	32.15	66.68	27.21	62.07	15.79	35.94	37.25	89.69	32.91	83.50
	300	34.12	63.02	50.81	75.65	0.1	47.75	58.55	101.60	27.84	87.27
0.1	150	21.83	70.73	18.92	44.67	9.16	35.30	48.36	58.12	31.24	18.97
	230	30.54	61.73	47.09	84.11	10.07	53.45	59.45	95.05	35.18	54.34
	300	26.65	73.18	58.423	107.80	36.73	47.35	84.11	86.86	46.80	58.04
0.2	150	29.27	61.06	65.52	117.12	28.31	46.44	94.22	77.44	25.89	10.02
	230	27.96	60.22	50.21	121.66	48.52	56.64	112.88	102.62	32.01	7.85
	300	34.48	55.99	75.31	62.11	28.32	78.18	80.63	80.07	41.05	20.32
0.3	150	16.70	65.10	41.73	51.28	20.03	34.37	44.99	80.48	33.27	10.42
	230	63.28	47.21	41.87	89.73	21.78	34.83	52.65	100.64	31.44	28.34
	300	22.85	67.88	48.78	79.48	18.91	46.96	56.61	87.19	35.67	26.55
0.4	150	33.98	60.06	46.93	76.70	26.16	40.42	51.84	96.91	31.71	261.24
	230	32.07	61.45	51.79	82.82	135.41	49.32	61.52	79.05	34.63	6.10
	300	29.92	58.47	62.13	91.70	93.05	52.74	78.99	63.30	30.66	23.05
0.5	150	32.38	54.03	47.51	81.56	31.02	43.22	55.72	79.71	23.57	26.43
	230	13.68	71.27	42.57	74.92	18.44	64.46	55.65	70.23	34.56	22.53
	300	31.71	51.47	65.96	97.32	119.23	61.88	72.80	70.38	41.43	53.37
0.6	150	23.10	51.07	18.39	72.42	46.62	29.32	53.13	44.54	29.14	8.25
	230	26.56	62.42	47.92	83.67	10.75	52.48	57.20	49.57	33.78	10.64
	300	31.99	56.90	63.86	85.25	100.80	76.99	68.31	53.71	46.51	20.84
0.8	150	25.19	61.33	28.88	-	-	37.83	-	-	-	-
	230	26.77	62.81	32.46	-	-	-	-	-	-	-
	300	32.29	59.22	45.68	-	-	-	-	-	-	-
0.9	150	28.11	58.45	44.04	-	-	37.22	-	-	-	-
	230	-	-	25.97	-	-	-	-	-	-	-
	300	32.28	54.26	52.88	-	-	-	-	-	-	-

BTO has the hexagonal structure; high sensitivity Raman spectroscopy detects the small percentage hexagonal structure of BTO.

With a view to understand the different vibrational modes in different FE phases of BTO, Raman spectrums of BTO are deconvoluted with the Lorentzian curve fitting. The best-fit curves for the data measured at 150 K, 230 K, and 300 K are presented in Figs. 4.11b, c, and d, respectively. The best-fit parameters, such as mode frequency and FWHM are given in Tables 4.5 and 4.6, respectively. The FWHM of a mode represents phonon lifetime, i.e., FWHM varies inversely with the phonon lifetime [22]. The FWHM of E(TO2), A_1(TO1), B_1, E(TO3), and A_1(TO2) modes are decreasing with cooling the sample to the "rhombohedral" phase. There is no significant change in FWHM of A_1(TO3) mode with varying the temperature. A_1(TO2) and A_1(TO3) modes are splitting, and these splitted peaks have a slightly higher frequency than original modes. These splittings are because of local symmetry breaking due to strain at the domain boundaries [23].

4.2.2 $NiFe_2O_4$

The single-phase NFO exhibits the ten different modes of atomic vibrations. Five vibrations are infrared active ($5T_{1u}$) and remaining five are Raman active (A_g+E_g+$3T_{2g}$) [24]. The A_g mode refers to the "symmetric" stretching of oxygen atoms along Fe-O in the "tetrahedral" site [25]. The E_g refers to the "symmetric" bending of oxygen ions in the "tetrahedral" site [25]. The $3T_{2g}(1)$ mode refers to the translational motion of metal atom along with oxygens in "tetrahedral" sites. The $3T_{2g}(2)$ mode refers to the "symmetric" stretching of oxygen atoms along Fe-O in the "octahedral" site. Finally, the $3T_{2g}(3)$ mode refers to the symmetric bending of oxygen atoms in the "octahedral" site. The schematic representations of these modes and corresponding atomic vibrations in NFO are shown in Fig. 4.12 [25, 26].

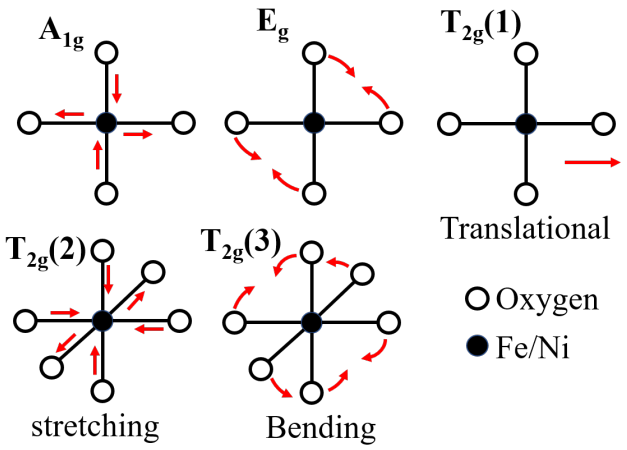

FIGURE 4.12: The schematic representation of the possible Raman mode vibrations of single phase NFO, idea adapted from [25] (2012, International Institute for the Science of Sintering).

In the present investigation, the Raman spectrum of NFO was measured at three different structural (FE) phases of BTO at 150 K, 230 K, and 300 K, to follow the same protocol as it was done for BTO to compare the BTO and NFO−BTO composites data, shown in Fig. 4.13a. The single-phase NFO exhibit five Raman active modes, which are $T_{2g}(1)$, E_g, $T_{2g}(2)$, $T_{2g}(3)$ and A_{1g} at 271, 332, 486, 576 and 703 cm^{-1}, respectively. The Raman spectra of NFO at different phases of BTO were deconvoluted by Lorentzian fitting [27], and best-fitted curves are shown in Figs. 4.13b, c, and d, respectively. The best-fit Raman mode positions and FWHM values are given in Table 4.7. In the single-phase NFO, FWHM and peak position was not varying significantly. However, the $T_{2g}(2)$, E_g and A_{1g} modes are showing a shift to a higher frequency with cooling the sample, which corresponds to the compressive stress. Some of the researchers explored similar behavior in nanoparticles and bulk NFO [28]. The shoulder like behavior in (left side) $T_{2g}(2)$, A_{1g} modes and in (right side) E_g mode were attributed to the "octahedral" site occupancy of Ni^{2+} and Fe^{3+} ions [25].

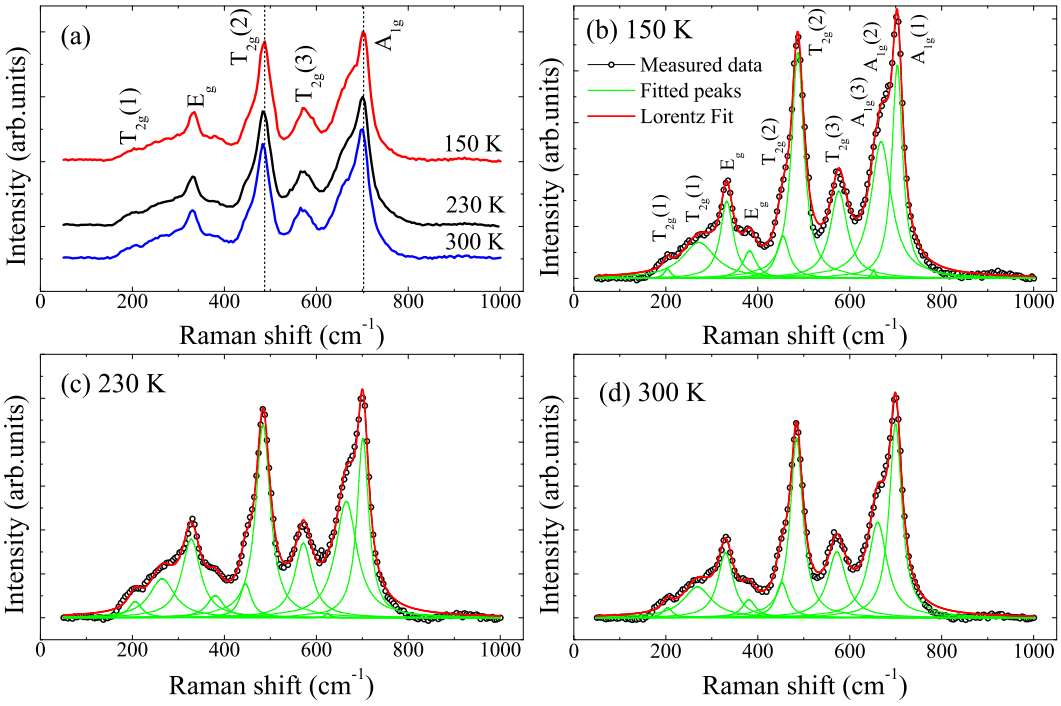

FIGURE 4.13: The Raman spectrum of NFO ($x = 1$) sample at different temperatures and peak fittings are done with Lorentz curve.

4.2.3 $BaTiO_3 - NiFe_2O_4$ composites

The Raman spectra of composites were obtained for different FE phases of BTO and the corresponding plots are shown in Fig. 4.14. It was found that up to $x = 0.6$, the Raman peaks corresponding to the NFO phase were not visible, and for $x = 0.8$ and 0.9, the Raman peaks corresponding to both NFO and BTO phases are visible. With a view to know more insight into these measurements, the data were fitted with

Lorentzian function, and best-fit curves for the compositions (x = 0.2, 0.8) are shown in Fig. 4.15.

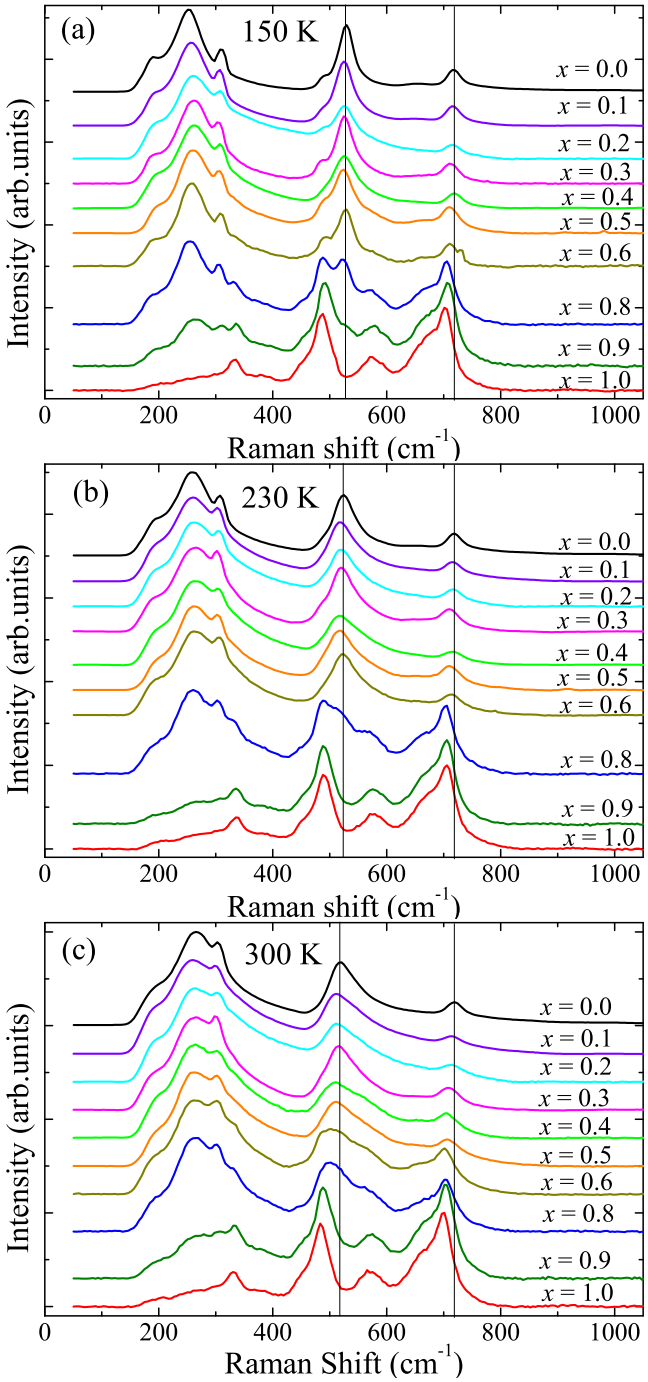

FIGURE 4.14: Raman spectra of NFO − BTO composites at 150 K, 230 K and 300 K.

TABLE 4.7: The Raman mode position and FWHM of the NFO in NFO−BTO composites at different temperatures.

		Peak position (cm^{-1})									
x	Temp.(K)	$T_{2g}(1)$		E_g			$T_{2g}(2)$	$T_{2g}(3)$	$A_{1g}(3)$	$A_{1g}(2)$	$A_{1g}(1)$
0.8	150	-	-	335.77	376.93	450.38	487.43	575.32	652.88	666.11	705.66
	230	-	-	333.98	374.99	449.11	489.37	572.16	652.77	667.52	704.14
	300	-	-	332.96	378.81	447.51	488.60	570.30	648.33	662.69	701.67
0.9	150	-	-	338.35	383.54	454.13	491.49	578.76	655.70	678.78	709.58
	230	207.98	263.10	335.75	383.86	453.72	490.07	577.67	651.13	667.81	705.38
	300	-	-	334.35	383.18	450.18	489.48	574.25	655.42	666.57	704.57
1	150	203.74	271.93	332.65	382.14	454.44	486.98	576.21	652.18	668.21	703.40
	230	206.04	264.62	327.87	380.31	446.02	484.17	571.96	624.47	665.15	701.31
	300	203.92	268.95	329.94	380.77	452.18	484.34	572.13	643.33	660.72	699.64
		FWHM (cm^{-1})									
0.8	150	-	-	26.65	61.41	20.81	32.87	48.50	29.26	49.37	29.47
	230	-	-	29.92	40.35	03.67	45.50	61.73	24.37	45.99	27.45
	300	-	-	33.57	50.32	10.28	44.90	63.31	33.37	44.06	33.67
0.9	150	-	-	29.42	63.26	21.40	36.26	55.94	30.30	61.80	24.48
	230	45.63	60.28	33.91	52.93	27.93	36.53	49.74	30.69	49.65	31.31
	300	-	-	38.21	62.63	24.77	41.15	64.51	37.84	49.90	32.30
1	150	17.93	87.61	33.82	34.75	33.70	32.94	44.71	09.25	54.27	28.20
	230	33.79	66.78	48.76	44.01	30.56	38.09	45.56	12.81	56.50	30.84
	300	24.73	74.65	40.39	36.45	31.81	33.19	48.96	38.83	49.23	33.18

The fitted curves corresponding to NFO and BTO modes are represented with green and violet color peaks, respectively. In the composites, A_1(LO3), A_1(TO3), E(TO1) modes were found to show a shift towards the lower frequency side with increased NFO content in composites, whereas A_1(TO2) peak shows a shift towards higher frequency side. However, the Raman modes corresponding to NFO were found to show no variation in the peak positions. The observed variations in peak positions were attributed to the tensile and compressive strains released by the counterpart phase in these composites [29, 30].

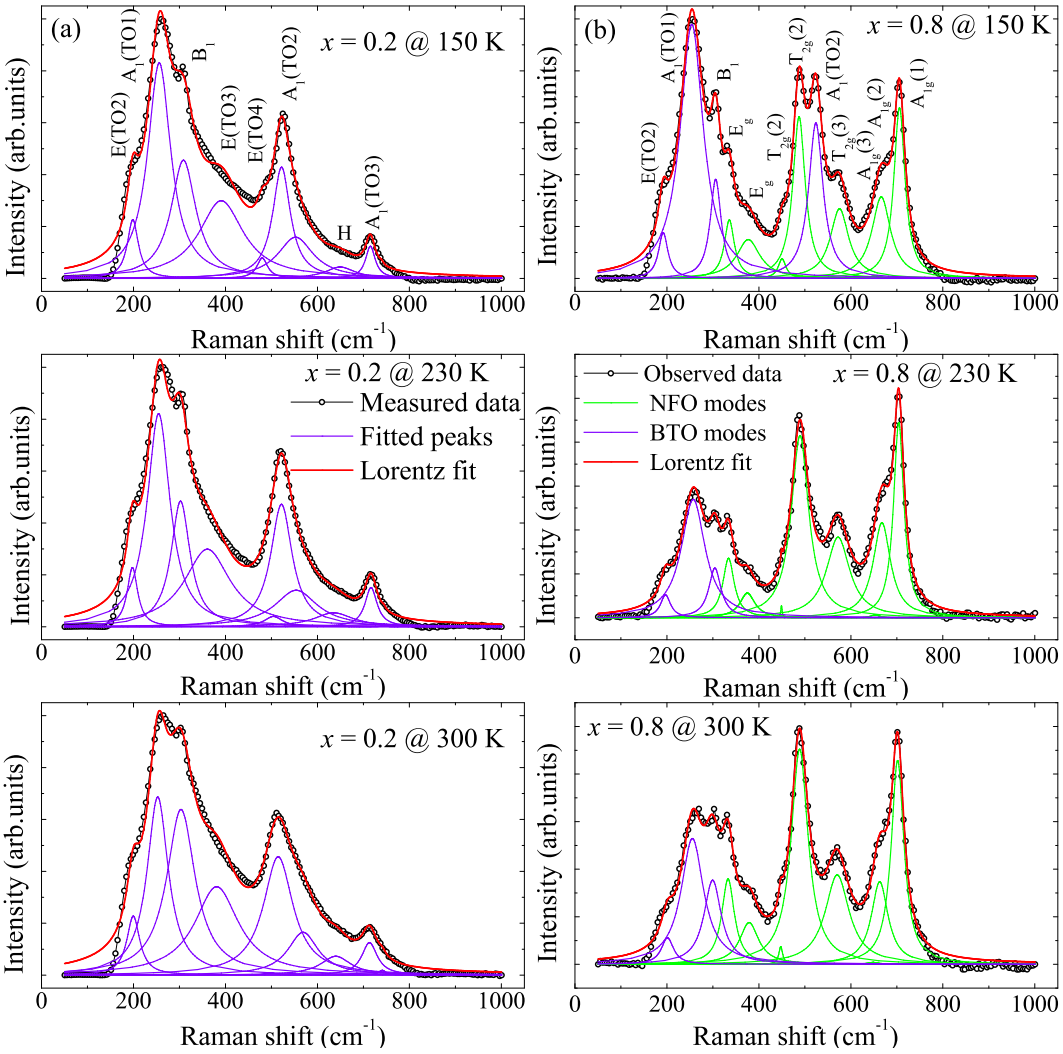

FIGURE 4.15: The Raman spectra along with Lorentz fitting of NFO − BTO samples for (a) $x = 0.2$ and (b) $x = 0.8$ at different temperatures.

4.2.4 Cation distribution

With a view to knowing the effect of lattice strain from BTO on the cation distribution of NFO, the following analysis was done. Also, the obtained results were corroborated the cation arrangement estimated from XRD data and the Raman data.

It is known that the intensity ratio relation of $A_{1g}(3)$ and $A_{1g}(2)$ modes give the information about cation distribution between the "tetrahedral" and "octahedral" sites in NFO. The cation distribution, in turn, will affect the magnetic properties [9],

$$y = \frac{I(A_{1g}(3))}{I(A_{1g}(3)) + I(A_{1g}(2))} \tag{4.11}$$

here, y represents the cation arrangement between the "tetrahedral" and "octahedral" sites of mixed spinel ferrites.

$$[Ni_yFe_{1-y}]_T[Ni_{1-y}Fe_{1+y}]_OO_4 \tag{4.12}$$

Since the Raman modes corresponding to NFO are visible for x = 0.8, 0.9, and 1 samples, the data was analyzed only for these samples. Based on the estimated cation distribution, the magnetic moment per formula unit was calculated for the x = 0.8, 0.9, and 1 samples and are given in Table 4.8. The calculated values are matching well with the magnetic moments calculated from magnetic measurements in chapter 5.

Further, the peak shift can be realized quantitatively by calculating the vibrating cation's effective force constant. The effective force constant of the ions pertaining to "tetrahedral" and "octahedral" sites of NFO was estimated for x = 1, 0.9, and 0.8 composite samples by the following equations [9],

$$k_T = 7.62 \times M_T \times \nu_T^2 \times 10^{-3} \tag{4.13}$$

$$k_O = 10.62 \times M_O \times \nu_O^2 \times 10^{-3} \tag{4.14}$$

here, k_T, M_T and ν_T are the force constant, molecular weight and frequency of A_{1g} of tetrahedral site, whereas the k_O, M_O and ν_O are the force constant, molecular weight and frequency of E_g of "octahedral" site of NFO in composites.

TABLE 4.8: The cation distribution, magnetic moment per formula unit and the effective force constant values for x = 0.8, 0.9 and 1 samples.

x	Temp. (K)	y	μ ($\mu_B/f.u.$)	ν_O (cm^{-1})	ν_T (cm^{-1})	M_T (g/mol)	M_O (g/mol)	k_T	k_O
0.8	150	0.0313	2.19	335.77	705.66	55.929	114.444	2.122	1.370
0.8	230	0.0289	2.17	333.99	704.14	55.922	114.451	2.113	1.356
0.8	300	0.0230	2.14	332.97	701.67	55.906	114.467	2.097	1.348
0.9	150	0.0184	2.11	338.35	709.58	55.892	114.480	2.144	1.392
0.9	230	0.0200	2.12	335.75	705.38	55.897	114.476	2.119	1.337
0.9	300	0.0221	2.13	334.35	704.57	55.903	114.470	2.115	1.359
1	150	0.0594	2.36	332.65	703.40	56.009	114.364	2.112	1.344
1	230	0.0364	2.22	327.87	701.31	55.944	114.429	2.097	1.306
1	300	0.0154	2.09	329.94	699.64	55.884	114.489	2.084	1.324

The obtained parameters are given in Table. 4.8. It was observed that the "tetrahedral" site's force constant values were increasing with temperature and were varying randomly with NFO content. The constant force values of the "octahedral" site were not varying systematically. Since the constant force value is inversely proportional to atoms' bond length, it was understood that the cation distribution is not sufficient to see the substantial changes in the parameters related to Raman data. A detailed and deeper analysis with better sensitivity is required to see the substantial changes in the present investigation.

4.3 Chapter summary

The variation of crystallographic parameters of the constituent phases, BTO and NFO, was attributed to the strain that is pertaining to different FE phases of BTO in composites. The Raman data shows the significant changes in peak positions, and FWHM was also attributed to the structural changes of BTO. The estimated cation distribution in "tetrahedral" and "octahedral" sites of the NFO phase supports the results obtained from temperature-dependent x-ray diffraction data. The magnetic moment per formula unit calculated from XRD and Raman was in correlation with each other and in agreement with the values measured from magnetization data.

Bibliography

[1] J. Su and J. Zhang, J. Mater. Sci.: Mater. Electron. **30**, 1957 (2019).

[2] J. J. Shephard, S. Ling, G. C. Sosso, A. Michaelides, B. Slater and C. G. Salzmann, J. Phys. Chem. Lett. **8**, 1645 (2017).

[3] V. Gorige, R. Kati, D. H. Yoon and P. S. Anil Kumar, J. Phys. D: Appl. Phys. **49**, 405001 (2016).

[4] M. K. Lee, T. K. Nath, C. B. Eom, M. C. Smoak and F. Tsui, Appl. Phys. Lett. **77,** 3547 (2000).

[5] B. Sarkar, B. Dalal, V. D. Ashok, K. Chakrabarthi, A. Mitra and S. K. De, J. Appl. Phys. **115**, 123908 (2014).

[6] R. N. Bhowmik, G. Vijayasri and R. Ranganathan, J. Appl. Phys. **116**, 123905 (2014).

[7] C. Jacinto, T. Catunda, D. Jaque, J. García Sole and A. A. Kaminiskii, J. Appl. Phys. **101**, 023113 (2007).

[8] C. Peng, Y. Zhang, Z. W. Cheng, X. Cheng and J. Meng, J. Mater. Sci. Mater. Electron. **13**, 757 (2002).

[9] K. K. Bestha, J. J. Abraham, J. A. Chelvane and V. Gorige, Phys. Scr. **95**, 085802 (2020).

[10] R. W. James, The optical principles of the diffraction of x-rays, (1962).

[11] K. B. Modi, T. K. Pathak, N. H. Vasoya, V. K. Lakhani, G. J. Baldha and P. K. Jha, Indian J. Phys. **85**, 411 (2011).

[12] B. D. Cullity, Elements of x-ray diffraction, 2^{nd} edition, (1978).

[13] E. Prince, International tables for crystallography, Vol. C (New York, Wiley), 578 (2004).

[14] C. S. Kim, S. W. Lee, S. I. Park, J. Y. Park and Y. J. Oh, J. Appl. Phys. **79**, 5428 (1996).

[15] A. Wei, L. T. Hui, W. C. Hai, D. C. Ling, L. N. Neng, L. Yong, Q. Z. Ming, S. Tao, W. Y. Yin, J. Huan, T. G. Shan and J. X. Ping, Acta Phys. Chim. Sin. **31**, 1059 (2015).

[16] J. L. Parsons and L. Rimai, Solid State Commun. **5**, 423 (1967).

[17] E. Smith and G. Dent, Modern Raman spectroscopy-A practical approach, John Wiley and sons limited, (2005).

[18] V. T. Srikar and S. M. Spearing, Exp. Mech. **43,** 238 (2003).

[19] F. Urena, S. H. Olsen, L. Siller, U. Bhaskar, T. Pardoen and J. P. Raskin, J. Appl. Phys. **112**, 114506 (2012).

[20] A. Gajovic, J. V. Plestina, K. Zagar, M. Plodinec, S. Sturm and M. Ceh, J. Raman Spectrosc. **44**, 412 (2013).

[21] L. V. Leonel, A. Righi, W. N. Mussel, J. B. Silva and N. D. S. Mohallem, Ceram. Int. **37**, 1259 (2011).

[22] N. Khatun, Anita, P. Rajput, D. Bhattacharya, S. N. Jha, S. Biring and S. Sen, Ceram. Int. **43**, 14128 (2017).

[23] M. Osada, M. Kakihana, S. Wada, T. Noma and W. S. Cho, Appl. Phys. Lett. **75,** 3393 (1999).

[24] A. Ahlawat and V. G. Sathe, J. Raman Spectrosc. **42**, 1087 (2011).

[25] Z. Z. Lazarevic, C. Jovalekic, D. Sekulic, M. Slankamenac, M. Romcevic, A. Milutinovic and N. Z. Romcevic, Sci. of Sinter. **44**, 331 (2012).

[26] M. N. Iliev, D. Mazumdar, J. X. Ma, A. Gupta, F. Rigato and J. Fontcuberta, Phys. Rev. B, **83**, 014108 (2011).

[27] B. Nandan, M. C. Bhatnagar and S. C. Kashyap, J. Phys. Chem. Solids **129**, 298 (2019).

[28] Y. Wang, L. Li, Y. Zhang, X. Chen, S. Fang, and G. Li, J. Phys. Chem. C **121**, 19467 (2017).

[29] S. Umashankar, T. Parida, K. R. Kumar, A. M. Strydom, G. Markandeyulu and K. K. Barathi, J. Magn. Magn. Mater. **439**, 213 (2017).

[30] R. Djemour, A. Redinger, M. Mousel, L. Gutay, X. Fontane, V. I. Roca, A. P. Rodriguez and S. Siebentritt, Opt. Express **21**, A695 (2013).

Chapter 5

Magnetic properties of NFO−BTO composites

The study of ME coupling phenomena in the two-phase particulate multiferroic materials by measuring ME coupling coefficient, particularly in NFO−BTO particulate composites is a complicated process because of the leakage current caused by the NFO. For measuring the ME coupling coefficient in these multiferroics, applying the electric voltage to the sample for polling is unavoidable. Therefore, to circumvent these difficulties, it will be interesting to obtain the same information alternatively. It is believed that the temperature-dependent magnetic measurements of these samples would give the signature of strain-induced ME coupling phenomena [1].

This chapter demonstrates the significance of the strain-mediated ME coupling phenomenon by performing the temperature-dependent magnetization and electron spin resonance measurements. Also, magnetic hysteresis loops measured at different temperatures representing to the different FE phases of BTO give a hint of the ME coupling effect at the interface of ferrite−FE in composites. Also, to understand the effect of BTO on the magnetic transition temperature of NFO, the temperature-dependent magnetization measurements over a temperature range, 300-700 K was performed. Also, to complement the magnetization measurements, the room - temperature electron spin resonance measurements were carried out for all the samples, and data were analyzed. The underlying mechanism responsible for "ME coupling" in the NFO−BTO composites has been explained by analyzing composites' magnetic data.

5.1 Temperature dependent magnetization

5.1.1 Low-temperature regime (100 < T < 330 K)

Figure 5.1 shows the variation of magnetization with temperature (*M-T*) measurements of NFO−BTO composites for x = 0.1 to 1 samples in the range, 100 - 330 K with field cooling (FC) and field warming (FW) modes at 250 Oe applied magnetic field. The *M-T* curves were found to show an enhancement in magnetization with decreasing temperature, and the reason may be the reduction in spin fluctuations in the NFO phase of composites at lower temperatures [1]. It is a well-known fact

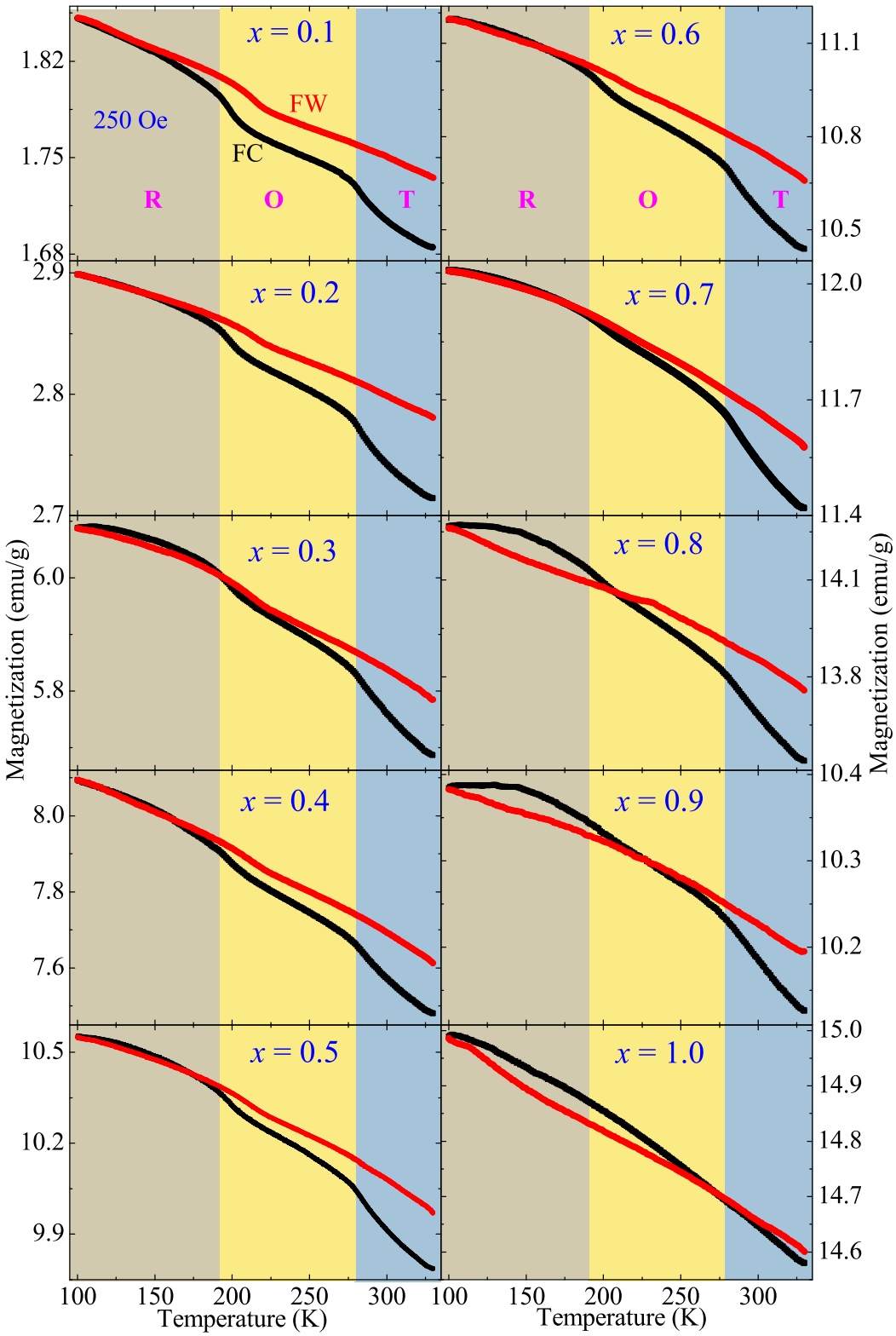

FIGURE 5.1: The temperature-dependent magnetization of NFO - BTO composites for different x values.

that the BTO exhibits structural transitions from "tetragonal" to "orthorhombic" and "orthorhombic" to "rhombohedral" at 278 K and 190 K temperatures, respectively [2]. Interestingly, the *M-T* curves show jumps for composite samples around 190 K and 278 K, but no jumps in x = 1 sample, signifying the effect of BTO on the *M-T* measurements. The observed jumps are found to match with the structural phase transitions of BTO. The BTO possesses different strain states corresponding to the different FE phases. During the phase transition, the strain generated in the BTO will transfer from the FE phase to the magnetic phase via a hetero-grain interface. Here strain acts as a driving force to reorient the magnetic moments present in the magnetic grains. The strain transfer across the NFO−BTO interface becomes possible because of ME coupling that is present at the interface between BTO and NFO grains.

The jumps are found to be significant in FC curves than the FW curves due to irreversible thermal relaxation of the magnetic moments induced by temperature. These jumps are gradually decreasing with a decrease in BTO content in the composite; this indicates that the strain transfer across the heterograin is reduced. Usually, these jumps are very much prominent in heterostructured thin films [3], but it isn't easy to observe in polycrystalline materials, particularly in particulate composites. It has become possible due to high-quality samples with a clear contact interface without any dead layer in between NFO and BTO grains. Here, coupling phenomena depends on the amount of strain generated in BTO transferred across the hetero-grain. In the *M-T* curves, a hysteresis behavior was observed in between FC - FW curves, a hysteric behavior increases with NFO concentration in the composite due to the "magnetic anisotropy" caused by the different domain orientation configurations with minimum energy [1].

5.1.2 High-temperature regime (30 < T < 700 °C)

Figure 5.2 shows the M−T measurements for x = 0.1 to 1 at an applied magnetic field of 250 Oe. The data was collected in heating mode. It is quite visible from the figure that the hump was observed at around 420 °C temperature in all the composites (marked with dotted line in Fig. 5.2). This hump was found to be significant in NFO rich composites, which ensures that the hump is originating from the NFO and it is due to the thermally activated electron hopping between Fe^{+2} and Fe^{+3} in the "octahedral" sites of NFO unit cell [4, 5, 6]. Subsequently, when the temperature is decreased further, a kink was observed at 120 °C in some samples (marked with arrow symbol in Fig. 5.2), which corresponds to the structural phase transition of BTO from "tetragonal" to "cubic" phases. However, this kink was not significant in NFO rich composites. The M−T curves were found to have different magnetization values with increased x values. However, the values were found to be consistent with x values beyond 400 °C. The applied magnetic field (250 Oe) is probably not sufficient to orient the magnetic moments in the applied field direction.

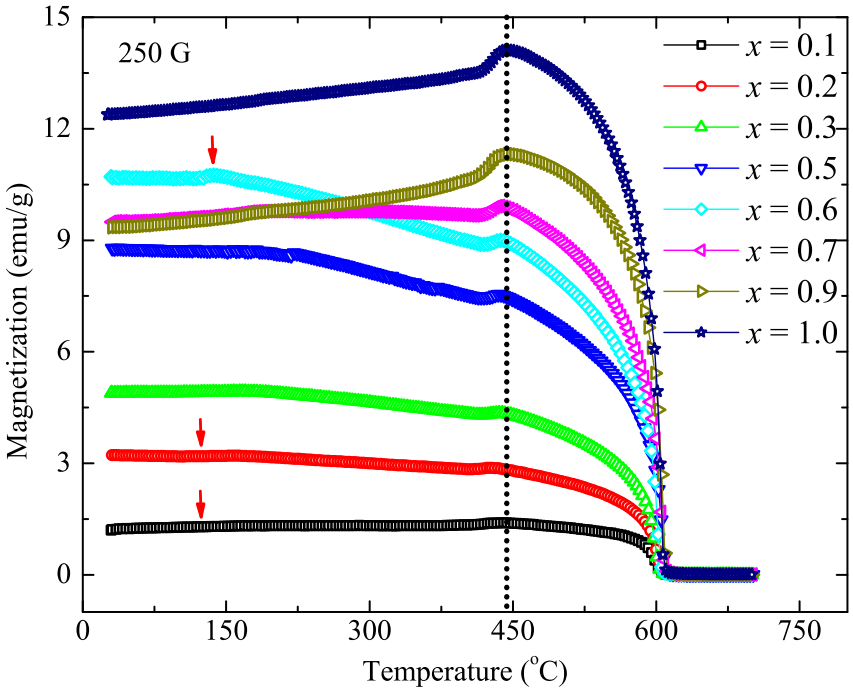

FIGURE 5.2: The temperature-dependent magnetization of NFO−BTO composites for different x values.

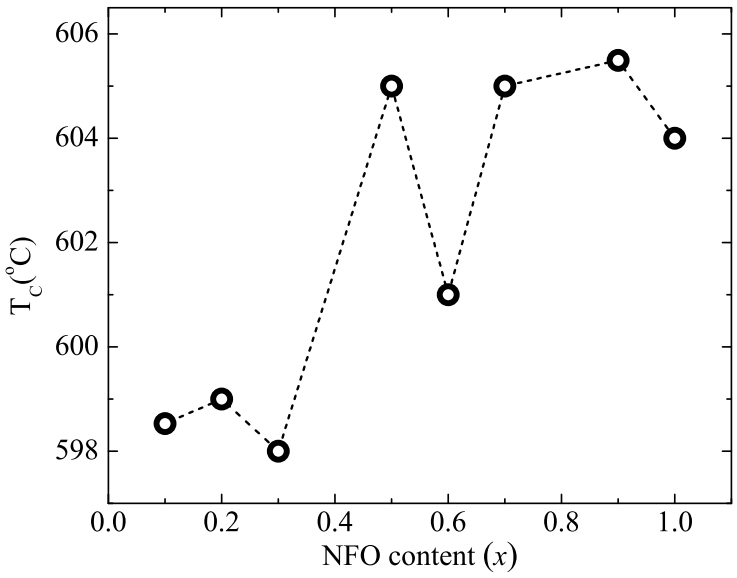

FIGURE 5.3: The variation of Curie temperature of NFO with x in NFO−BTO composites (dotted line is the guide to eye).

The ferri to paramagnetic transition temperature, T_C was obtained from the dM/dT versus T plots. The T_C of single-phase NFO was found to be at 604 °C, and the values for composites were found to increase with the increase of the NFO phase in samples, and the variation is shown in Fig. 5.3. The obtained T_C value is in agreement with the reported literature [7, 8], and this shows the quality of the samples in the present investigation. It is a known fact that the grain size is directly related to the T_C; that is, the T_C will increase with an increase in grain size [9]. The present work found that the NFO grain sizes are increasing with increasing NFO content. Therefore, the observed behavior conforms with the observations made via microstructure analysis in the previous chapter.

5.2 Magnetic hysteresis loops

5.2.1 Low-temperature regime (100 < T < 330 K)

Figure 5.4(a-c) shows the magnetic hysteresis ($M-H$) loops of samples for x = 0 to 1, measured at 300 K, 230 K and 150 K, respectively. All the key magnetic parameters such as "coercivity" (H_C), "remanence magnetization" (M_R) and "saturation magnetization" (M_S) were obtained from the $M-H$ data and the variation of these values as a function of NFO content (x) are shown in Fig. 5.5. The saturation magnetization of single-phase NFO was found to be 48 emu/g at 300 K, and it is in good agreement with the reported values [1, 10]. The M_S values were found to increase with decreasing temperature for a given x in the composites. The observed behavior is due to the alignment of magnetic moments in the applied field direction at low temperatures [11]. Similarly, the increased M_S values with an increase in NFO content is understandable. The linear increment in M_S values with x indicates enhanced NFO content. The M_R values of composite samples were found to increase up to x = 0.5 sample and decrease for further increase of x values. The observed variation is attributed to the maximum interface contact between the magnetic and FE domains. That means, beyond x = 0.5 composition, the contact interface starts breaking, and spin canting effects may take place at the surface of the NFO grains, thereby decreasing M_R values.

Figure 5.5(a) shows the variation of H_C values with x. The H_C values for the composites were found to decrease with an increase in NFO content except for x = 0 and 0.1 samples. This particular observation is in agreement with the earlier report for similar systems [7, 8]. The variation of the observation is mainly attributed to the pinning of magnetic moments of NFO with BTO grains at NFO−BTO interface during the process of domain switching [1]. Here, the BTO grain acts like a defect and dead layer in between the NFO grains.

Figure 5.6 shows the $M-H$ loop measured at room temperature for single-phase NFO in an applied magnetic field of ± 90 kOe. The sample was found to show no saturation behavior even at 90 kOe applied magnetic field due to the ferrimagnetic

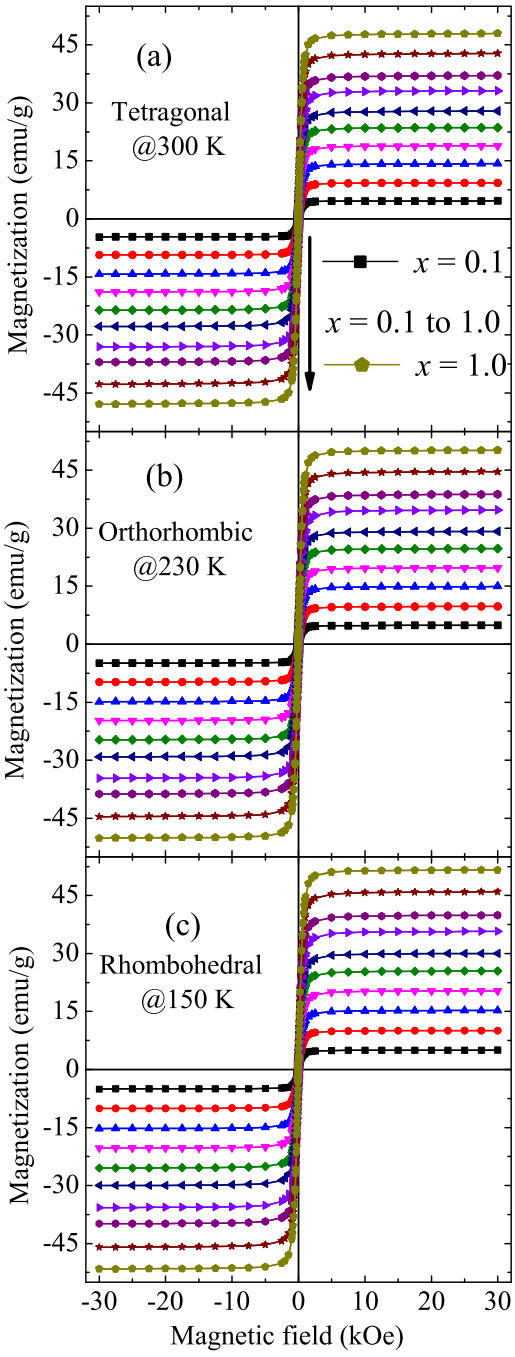

FIGURE 5.4: (a-c) Magnetic hysteresis loops of NFO−BTO composites at 300 K, 230 K and 150 K.

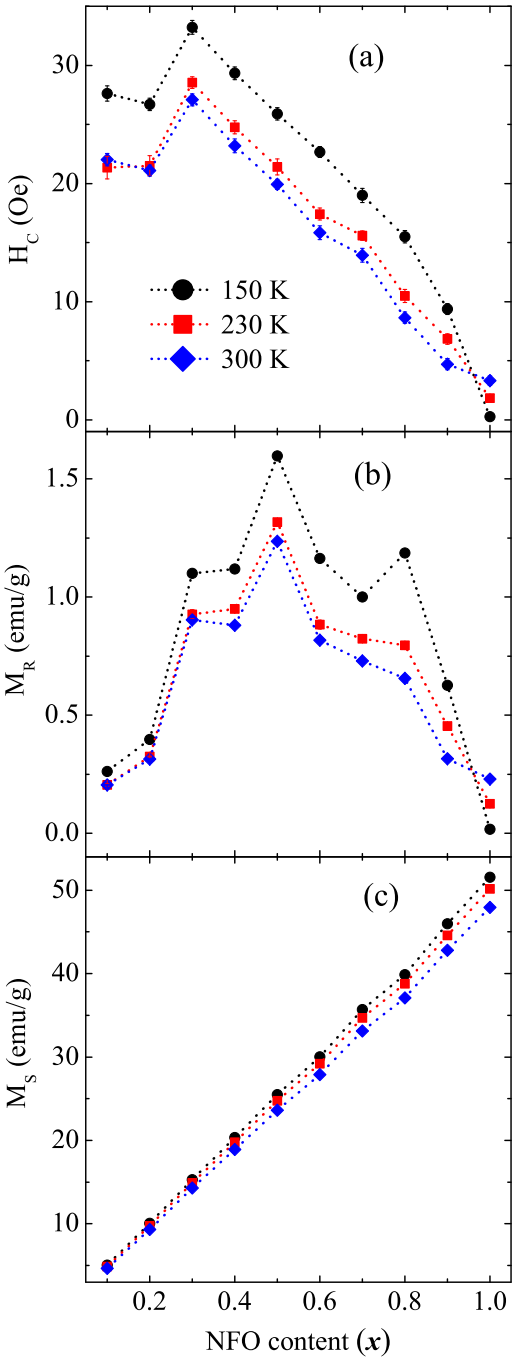

FIGURE 5.5: (a-c) Variation in the H_C, M_S, M_R with respect to x in NFO-BTO composites (dotted line is the guide to eye).

nature of the ferrite. However, magnetization value (at 90 kOe) was found to be 53 emu/g and 48 emu/g at 5 K and 300 K, respectively, which are in agreement with reported values [10].

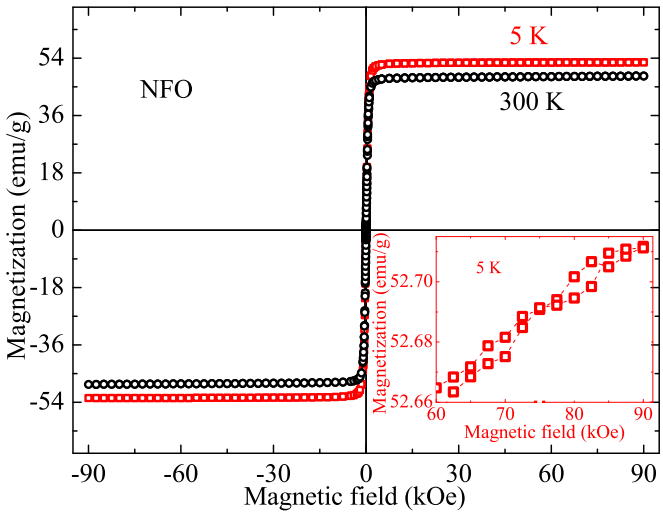

FIGURE 5.6: The magnetic hysteresis loops of NFO sample at 5 K and 300 K.

The outermost d electronic configuration of "Fe^{3+}" and "Ni^{2+}" are $3d^5$ and $3d^8$, respectively. The magnetic moments of "Fe^{3+}" and "Ni^{2+}" ions were found to be 5 μ_B and 2 μ_B, respectively. Therefore, the ferrites are antiferromagnetic materials with unequal magnetic moments in the "tetrahedral" and "octahedral" site. The net magnetic moment (μ) will be the difference between these two sites as given,

$$\mu = \mu_o - \mu_t \tag{5.1}$$

here, μ_o and μ_t are the magnetic moment in "octahedral" and "tetrahedral" site, respectively. If NFO has a normal spinel structure, then the Ni^{2+} ion will be in the "tetrahedral" site, and two Fe^{3+} ions will be in the "octahedral" site. The net magnetic moment comes out by 8 μ_B/f.u. If NFO has an inverse spinel structure, then a fraction of Fe^{3+} ions will be in "tetrahedral" sites, Ni^{2+} and remaining Fe^{3+} ions will be in "octahedral" sites. Then the net magnetic moment will be 2 μ_B/f.u.

In the present case, μ values were obtained from experimentally measured data by using the following formula,

$$\mu_{f.u.}(\mu_B) = \frac{M \times W_m}{\mu_B \times N_A} \tag{5.2}$$

here, M, W_m, μ_B and N_A are the magnetization (emu/g), molecular weight (g), Bohr magneton (9.274×10^{-21} emu) and Avagadro constant (6.022×10^{23} mol^{-1}), respectively.

The variation of experimentally measured μ values with x is shown in Fig. 5.7. The experimentally observed saturation magnetic moment of single-phase NFO (at 300 K) is found to be 2.01 μ_B/f.u. The experimentally measured magnetic moment

values were found to be in good concurrence with the theoretically obtained values. This observation confirms that the NFO in composites has an inverse spinel structure. A small deviation of experimental values from the theoretical values is due to the variation in nickel ferrite.

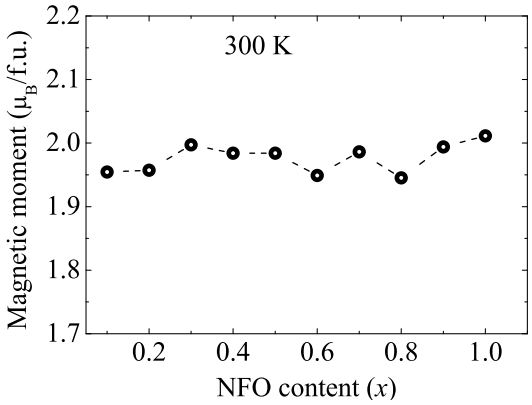

FIGURE 5.7: The variation of magnetic moment with x for NFO−BTO composites at 300 K (dotted line is the guide to eye).

5.2.2 High-temperature regime (30 < T< 700 °C)

Figure 5.8 shows the M−H loops of composite samples measured at 300 °C. As mentioned in the previous section, the parameters such as H_C, M_R, and M_S were obtained, and their variation with NFO content x were given in Fig. 5.9. From the figure, it has been found that the variation is almost similar to that of the variation observed for low temperature.

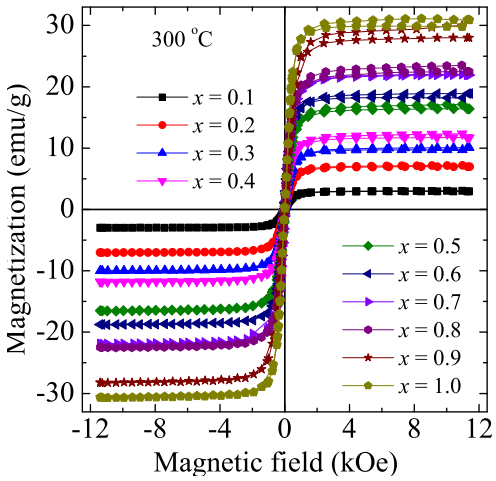

FIGURE 5.8: The magnetic hysteresis loops of NFO-BTO composites for different x values at 300 °C.

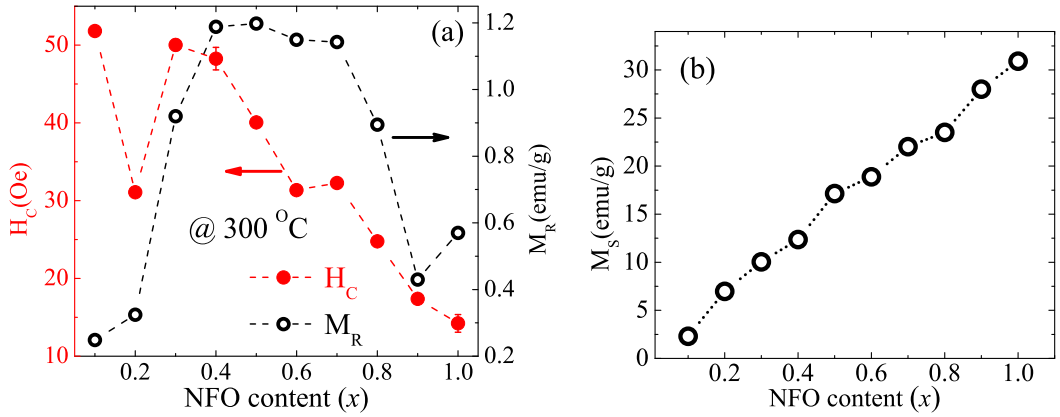

FIGURE 5.9: The variation of remanence magnetization and coercive field values for different x values at 300 $^{\circ}C$ of NFO-BTO composites (dotted line is the guide to eye).

5.3 Electron spin resonance

The room-temperature ESR or EPR measurements for all the composite samples were measured in the magnetic field range, 0 - 800 mT, and the derivative of the microwave absorption versus magnetic field plots are shown in Fig. 5.10. The parameters such as "g-factor", "resonance field" (H_r), "peak to the peak" line width (ΔH_{PP}), and the ratio between positive and negative absorption intensity ($\frac{A}{B}$) were obtained, and the values are given in Table 5.1.

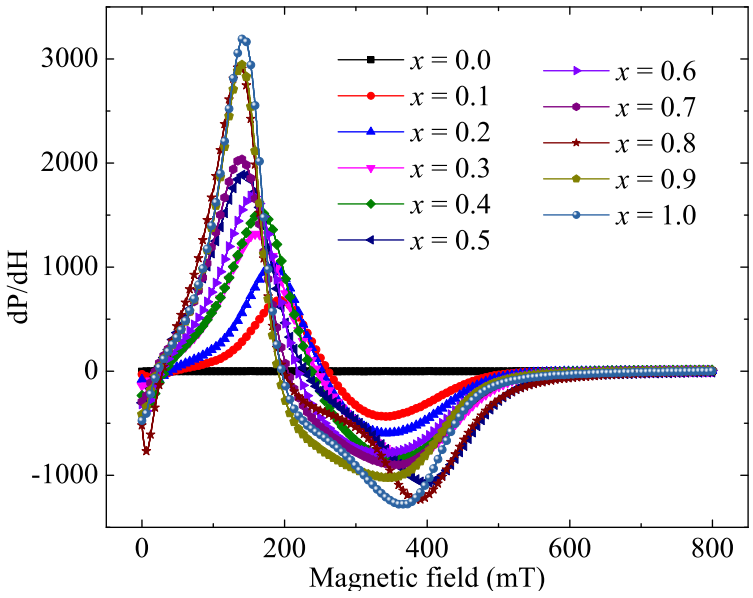

FIGURE 5.10: The electron spin resonance spectra of NFO-BTO composites for different x values.

It is clear from Fig. 5.10 that the single-phase BTO was found to show straight-line behavior of ESR signal with varying applied magnetic field due to nonmagnetic in nature. Except for the $x = 0$ sample, all the composites showed magnetic spin resonance with positive and negative peaks with varying the applied magnetic field.

TABLE 5.1: The resonance field (H_r), peak to peak line width (ΔH_{pp}) and ratio between positive and negative intensity(A/B) of NFO-BTO composite samples for different x values.

x	H_r (mT)	ΔH_{pp}(mT)	A/B
0.0	-	-	-
0.1	260.87	145.87	1.56
0.2	252.16	158.35	1.70
0.3	245.85	212.50	1.64
0.4	237.88	189.91	1.82
0.5	228.89	253.63	1.76
0.6	218.61	178.23	2.15
0.7	204.56	217.92	2.26
0.8	198.46	250.08	2.37
0.9	191.07	207.25	2.88
1.0	195.93	224.14	2.49

It is known that the unpaired electrons present in the ferrite phase of composites are responsible for the ESR. The g-factor was obtained based on the following equation [12],

$$g = \frac{h\nu}{\mu_B H_r} \tag{5.3}$$

here, h, ν, μ_B and H_r are Plank's constant, applied microwave frequency, Bohr magneton and spin resonance field, respectively. The variation in g-factor with x is shown in Fig. 5.11. The g−factor values were found to increase with an increase of x values. The reason for the observed behavior is explained as follows: In the case of BTO rich composites, the magnetic moments are randomized at magnetic grain boundaries, which in turn results in reduced net magnetization per NFO phase [12]. In order to resonate the spins present in the compound, a higher magnetic field is required. Therefore, resonance field increases with decreasing in x in the composites. As the non magnetic material (BTO) present in the composite will reduce the net magnetization of the composite and hence, the resonance magnetic field is increased. It is clear from the above equation, g−factor is inversely proportional to the resonance field. Therefore, g−factor is increases with NFO content (x). Generally, the g-factor will be 2 for a free electron. However, in the present case, the "spin-orbit" interaction is not negligible, and it might have contributed to the obtained g-factor of more than 2 [13]. The g−factor of single-phase NFO was found to be 3.42, which is in agreement with the earlier reports [14, 15].

Another interesting observation one can make out from figure that the ESR spectra contain asymmetric signal variation. This asymmetry in spectra arises due to the existence of weak "inter-cluster" interaction of magnetic atoms [16]. This slight "asymmetry" in the shape of the spectrum also suggests the non-equivalent positions

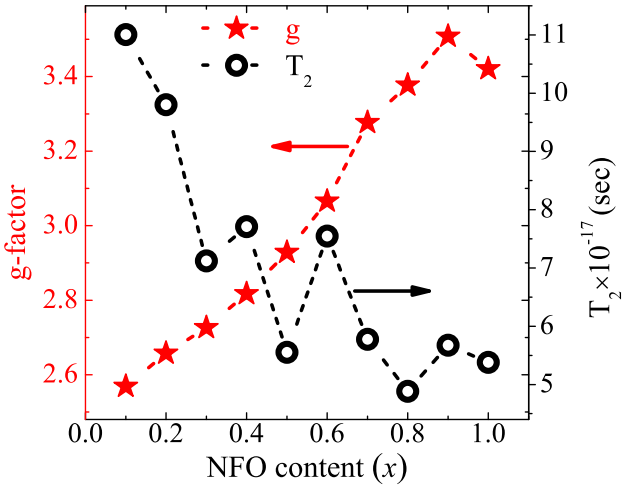

FIGURE 5.11: The variation of g - factor and spin−spin relaxation time values with x of NFO-BTO composites (dotted line is the guide to eye).

of the Fe^{3+} ions in the ferrite [16].

The "peak to peak" line width (ΔH_{PP}) values of the composites are in the range, 145 mT − 224 mT, and are given in Table. 5.1. These values were found to be smaller than those for the NFO bulk compounds reported in the literature [15, 17], which clearly indicates that the non-magnetic BTO in the composite makes the samples show decreased line widths compared to single-phase bulk NFO. The ΔH_{PP} values were increasing with NFO content (x). The high peak to peak line width values indicate the clustering behavior of the grains in the sample [15]. The FESEM images (chapter 3) shows the clustering behavior of NFO grains in composites and this clustering behavior increases with NFO content (x). Another interesting parameter, "spin-spin relaxation" time (T_2), has been considered, which is related to the line width of the ESR spectra, which is caused by the influence of the surrounding magnetic ions. The "spin-spin relaxation" time (T_2) was calculated from the obtained parameters ΔH_{PP} and g-factor by the following equation [18],

$$T_2 = \frac{\hbar}{\sqrt{3} g \beta \Delta H_{PP}} \tag{5.4}$$

where, $\hbar$ is the "Plank constant" (6.626×10^{-34} J s) and β is the "Bohr magneton" (9.274×10^{-24} J T^{-1}). The calculated T_2 values are in concurrence with the reported values for similar compounds [18] and were found to decrease with increase in x (shown in Fig. 5.11). The BTO present in the compound may act as a potential pinning source for the spins at the hetero-domain interface, thereby reducing the spin-spin relaxation time [19].

The ratio of the intensities positive to negative peaks (A/B ratio) of the ESR spectra is given in Table 5.1. If the A/B ratio is unity, then the resonating spin corresponds to the free electron [19]. In the present samples, the A/B ratio was found

to be larger than unity, which indicates that the resonating spins are highly interacting in nature, probably with other spin, lattice and defects. The A/B ratio values were increasing at x due to increased magnetic phase content. That means the increased BTO found to enhance the destabilization of magnetic moments and their interactions.

5.4 Chapter summary

The observed jumps in temperature-dependent magnetization curves of NFO−BTO composites confirm the strain-mediated ME coupling between NFO and BTO. The Curie temperature of the NFO was found to increase with NFO content (x) in composites. The observed hump in the temperature-dependent magnetization curves at 420 °C was ascribed to the thermally activated electron hopping between two cations in the octahedral site of the NFO unit cell. The remanence magnetization was found to be maximum for x = 0.5 sample; it hints that the maximum contact interface between ferrite and FE is crucial for observed behavior. The magnetic coercivity of the composites was decreasing with ferrite content (x) due to the pinning of spins at the hetero-interface. The calculated magnetic moment values at saturation magnetization for all the composites samples, including single-phase NFO, was found to be around $\approx 2\ \mu_B/f.u.$, indicating the inverse spinel structure of NFO in the samples of the present investigation. The g−factor of composites was increasing with x and the underlying reasons were discussed. The A/B ratio of the ESR resonance spectra was close to unity in composites and increased with an increase in x. The observed behavior was due to enhanced destabilization of magnetic interactions with increased BTO in the composites.

Bibliography

[1] V. Gorige, R. Kati, D. H. Yoon and P. S. Anil Kumar, J. Phys. D: Appl. Phys. **49**, 405001 (2016).

[2] J. Su and J. Zhang, J. Mater. Sci.: Mater. Electron. **30**, 1957 (2019).

[3] Y. S. Koo, K. M. Song, N. Hur, J. H. Jung, T. H. Jang, H. J. Lee, T. Y. Koo, Y. H. Jeong, J. H. Cho and Y. H. Jo, Appl. Phys. Lett. **94**, 032903 (2009).

[4] G. Sathishkumar, C. Venkataraju and K. Sivakumar, J. Mater. Sci. Appl. **1**, 19 (2010).

[5] M. H. Mahmoud, A. M. Elshahawy, S. A. Makhlouf and H. H. Hamdeh, J. Magn. Magn. Mater. **343**, 21 (2013).

[6] K. K. Patankar, S. S. Joshi and B. K. Chougule, Phys. Lett. A **346**, 337 (2005).

[7] B. Sarkar, B. Dalal, V. D. Ashok, K. Chakrabarthi, A. Mitra and S. K. De, J. Appl. Phys. **115**, 123908 (2014).

[8] J. P. Zhou, L. Lv, Q. Liu, Y. X. Zhang and P. Liu, Sci. Technol. Adv. Mater. **13**, 045001 (2012).

[9] J. L. Clabel, F. A. Ferri, F. L. Zabotto, V. A. G. Rivera, I. C. Nogueira, D. Garcia, O. F. delima, E. R. Leite, M. A. P. Silva and C. A. Cardoso, J. Magn. Magn. Mater. **407**, 160 (2016).

[10] S. Umashankar, T. Parida, K. R. Kumar, A. M. Strydom, G. Markandeyulu and K. K. Barathi, J. Magn. Magn. Mater. **439**, 213 (2017).

[11] S. Chikazumi and C. D. Graham, Physics of Ferromagnetism, second edition , International series of monographs on physics, 94 (1996).

[12] X. Cao and L. Gu, Nanotechnology **16**, 180 (2005).

[13] J. W. Lin, T. Tite, Y. H. Tang, C. S. Lue, Y. M. Chang and J. G. Lin, J. Appl. Phys. **111**, 07D910 (2012).

[14] Y. Wang, L. Li, Y. Zhang, X. Chen, S. F. Fang and G. Li, J. Phys. Chem. C **121**, 19467 (2017).

[15] L. Li, G. Li, R. L. Smith and H. Inomata, Chem. Mater. **12**, 3705 (2000).

[16] P. C. Sati, M. Kumar, S. Chhocker and M. Jewariya, Ceramic. Int. **41**, 2389 (2015).

[17] J. Snieder, Appl. Sci. Res. B **7**, 185 (1958).

[18] T. H. Ting and K. H. Wu, J. Magn. Magn. Mater. **322**, 2160 (2010).

[19] C. C. Yang, Y. J. Gung, C. C. Shih, W. C. Hung and K. H. Wu, J. Magn. Magn. Mater. **323**, 933 (2011).

Chapter 6

Dielectric properties of NFO−BTO composites

The ME coupling between ferrite and FE materials enables us to observe the substantial changes in the physical properties of the individual materials [1, 2]. Notably, the effect of electric/magnetic properties on FM/FE materials, respectively. In similar lines, an effort has been made to explore the possibility of measuring the dielectric and FE properties of composite and ferrite phase impact on them. It is known that the high dielectric constant materials as one of the constituent phases exhibit the high ME coupling in composites [3]. Therefore, the measurement of dielectric constant and FE properties for the ME multiferroic composites are worth performing to explore the underlying mechanism behind these physical properties. In the process, several properties such as permittivity, electric resonance, dielectric loss, impedance, and FE polarization, etc. will be analyzed; furthermore, underlying mechanisms will be discussed.

In this chapter, the dielectric constant variation of temperature measurements were performed in temperature range, $30 - 225$ °C. The frequency-dependent dielectric constant and dielectric loss over different temperatures (30 °C, 100 °C, 200 °C, and 300 °C) were measured over a frequency range, $20 - 40$ MHz. The room-temperature ferroelectric hysteresis ($P - E$) loops were measured for BTO and BTO rich composite samples in the applied field range $\pm$ 40 kV/cm. The variation of dielectric constant, dielectric loss, Curie temperature, piezoelectric resonance, FE coercivity, and FE remanence with NFO content (x) were analyzed; furthermore, the related mechanisms were discussed in the light of ME coupling.

6.1 Dielectric constant

6.1.1 Temperature-dependent dielectric constant ($BaTiO_3$)

Figure 6.1 shows variation of dielectric constant with temperature measurement of a single-phase BTO sample. The data were collected while heating the sample over the temperature range, 50−225 °C at 1 kHz frequency. The dielectric constant was increasing with increase in the temperature until it reaches the Curie temperature

and decreases for further increase in the temperature. The increase in dielectric constant is attributed to the thermally activated electric dipoles [2, 4]. Also, the width of the domain increases as it approaches to phase transition temperature [5]. At 122 $^{\circ}C$ a sharp peak in the temperature-dependent dielectric constant was noticed. The maximum dielectric constant was found to be around 10500, and it is consistent with the reported literature [6, 7]. The obtained high dielectric constant values infer the prepared BTO sample's high quality in the present investigation.

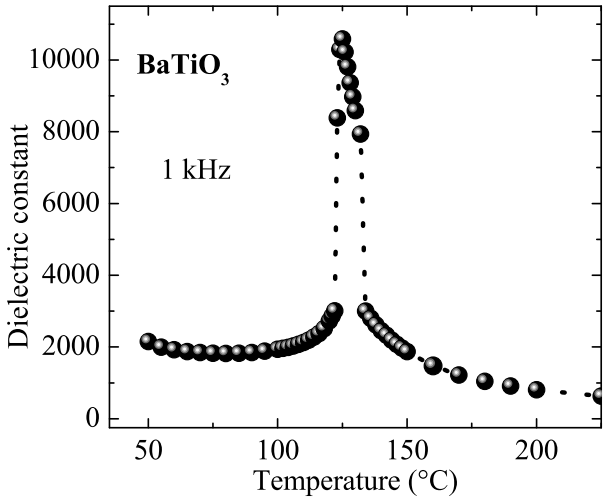

FIGURE 6.1: The temperature-dependent dielectric constant of single phase BTO measured at 1 kHz frequency.

6.1.2 Temperature dependent dielectric constant (NFO−BTO composites)

The temperature-dependent dielectric constant of composite samples for $x = 0.1-1$, measured at 1 kHz frequency were shown in Fig. 6.2. The single-phase NFO sample showed almost straight line behavior with an increase in the temperature [8] and was showing less dielectric constant due to the conducting nature of NFO [9]. The increased dielectric constant of NFO with temperature is attributed to the delocalization of dipoles with increased thermal energy, and in fact, these dipoles will align in the direction of applied electric field [10, 11]. The composite samples ($x = 0.1$ to 0.9) were shown to be showing a peak around 120 $^{\circ}$ C temperature, which corresponds to the phase transition temperature of BTO from FE to paraelectric (PE) phase, i.e., Curie temperature of BTO in composites. The variation in Curie temperature of the composite samples with x at 1 kHz frequency is shown in Fig. 6.3. The single-phase BTO shows Curie temperature at 122 $^{\circ}$C and was found to increase with increase of BTO in composites from $x = 0$ to 0.5 and becomes constant for the values beyond $x = 0.5$. The increase in Curie temperature with increased FE material is due to the lattice deformation in BTO with the addition of NFO [12].

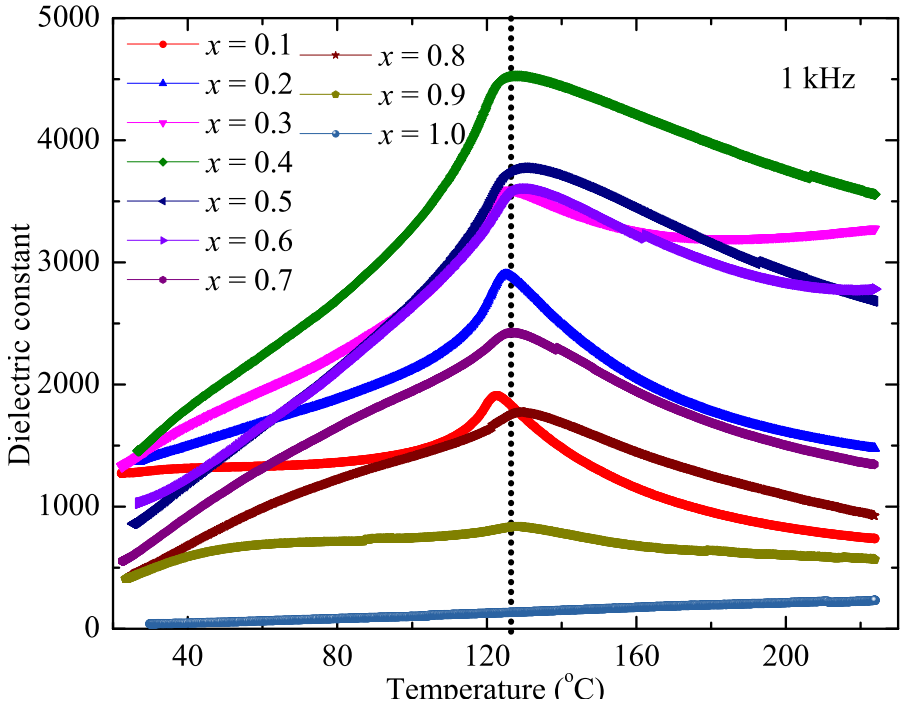

FIGURE 6.2: The temperature-dependent dielectric constant of NFO−BTO composites for x = 0.1 to 1 measured at 1 kHz frequency.

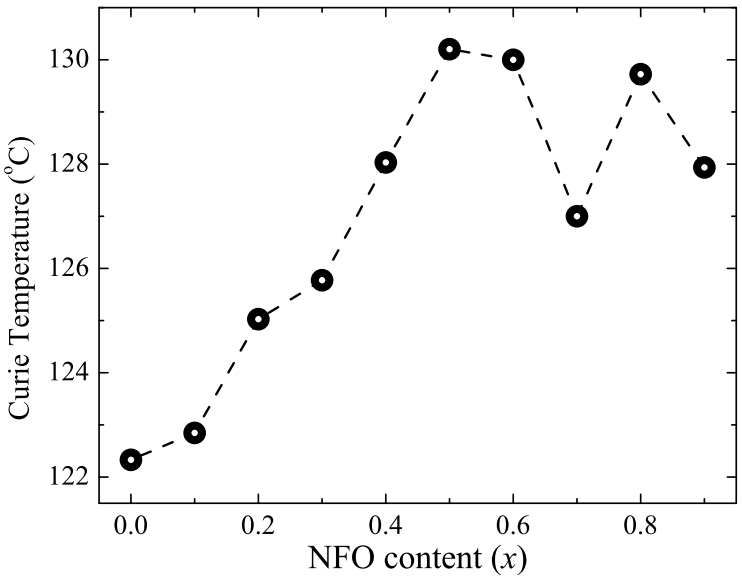

FIGURE 6.3: The variation of Curie temperature of NFO−BTO composites with respect to x (NFO content) (dotted line is the guide to eye).

The obtained dielectric constant values from the temperature-dependent dielectric constant measurements were plotted as a function of x and are shown in Fig. 6.4. The dielectric constant value of single-phase BTO was found to be higher than the values obtained for composite samples. The dielectric constant values were found to be increasing initially up to x = 0.4 and decreased thereafter for a further increase of x from 0.5 to 0.9. The observed variation is inconsistent with the variation of magnetic parameters with x. The reason for the observed behavior is mainly because of the enhanced interface contact between the ferrite and FE domains. Around x= 0.4 compositions, the NFO grains start breaking the electric circuit of BTO grains, and this may increase with an increase in x. Therefore, the high dielectric constant is susceptible to show high ME coupling in the composites [3]. In the prepared composite samples, the dielectric constant was found to increase with the contact interface, and it is maximum for equal ratios of individual phases in the composites. Therefore, in the present case, the x = 0.4 composite sample is showing the high ME coupling. Moreover, it was established in the literature that the high ME coupling coefficient was observed with 50% of the ferrite phase in NFO−PZT particulate composites [13].

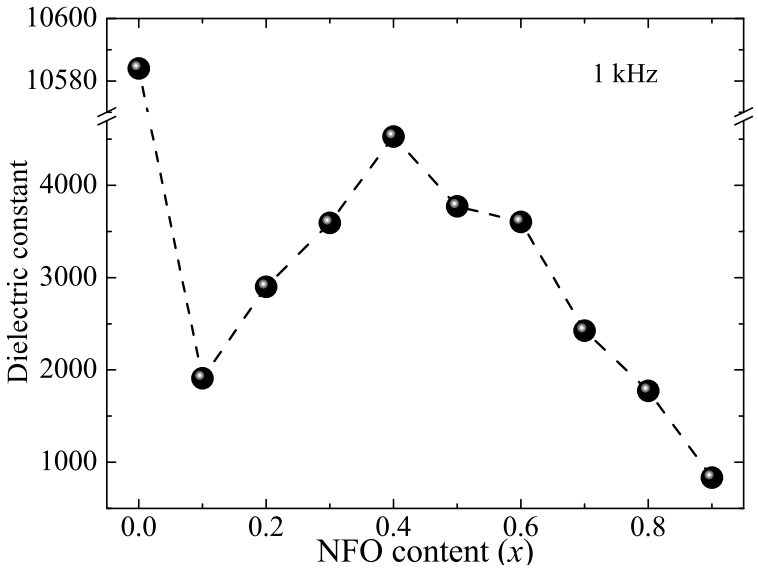

FIGURE 6.4: The variation of dielectric constant of NFO−BTO composites with NFO content (x) at 1 kHz frequency (dotted line is the guide to eye).

6.1.3 Dielectric constant of NFO−BTO composites at different frequencies

The temperature-dependent dielectric constant measurements were done for all the samples at 1, 10, 50, 100, 500, and 1000 kHz frequencies. A representative of x = 0.2 sample's dielectric constant variation with the temperature at different frequencies is shown in Fig. 6.5. In fact, similar behavior was noticed for all other samples in

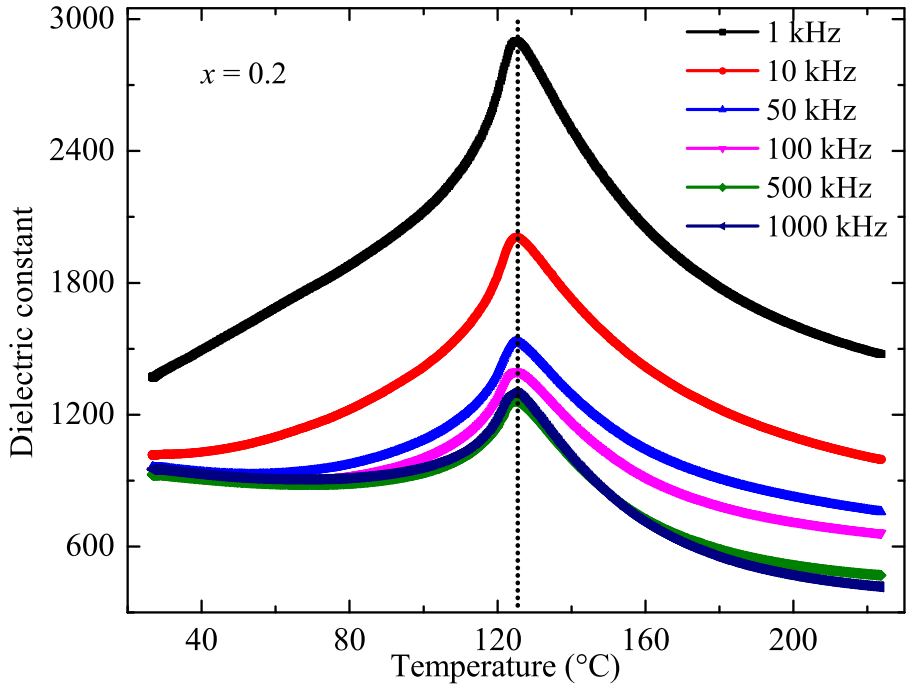

FIGURE 6.5: The temperature−dependent dielectric constant of x = 0.2 composite at different frequencies.

the series. From the figure, it is clear that the T_C is found to be the same for all frequencies. It is a fact that the "Curie temperature" is independent of frequency in the case of non-relaxor FEs [14, 15, 16]. In the present composites, one of the constituent phase BTO is a non-relaxor FE material. The Curie temperatures obtained at different frequencies for all the samples were found to remain constant. The reason may be due to the fact that in the case of non-relaxor materials, the electric dipoles may easily respond to the applied external field for a wide range of frequencies. In fact, there is no energy loss in these dipoles, and can able to follow the externally applied frequencies. Because of this reason, the FE domain sizes are more in non-relaxor FE compared to relaxor FE materials [17]. While in the case of relaxor FE, the energy loss of dipoles due to relaxation may lead to smaller domains than non-relaxor FEs. Further, the dielectric constant values at transition temperature were found to be higher at lower frequencies. The details of these observations will be explained in the next section.

6.1.4 Frequency−dependent dielectric constant

Figure 6.6 shows the dielectric constant as a function of frequency measurements of composite samples for x = 0 to 1 measured at different temperatures 30 °C, 100 °C, 200 °C and 300 °C in the range of 20 Hz to 40 MHz. The dielectric constant values are found to decrease continuously with increasing frequency. The observed high values of dielectric constant for all the samples at lower frequencies (below 1 kHz) may be attributed to the space charge or interfacial polarization contribution to the

net dielectric constant [7]. At high frequencies (above 1 kHz) dipolar or orientational polarization may contribute to the dielectric constant [7]. On further increase in frequency, the dielectric constant was found to be constant due to the inability of dipoles to respond with applied ac electric field [7].

Mainly, at lower frequencies (below 1 kHz), dielectric constant values of composites were found to vary randomly with x, and this behavior is common in ferrite−FE particulate composites [3, 7, 9, 18] and the possible reason could be as mentioned: As it was known from the FESEM images (chapter 3) that the ferrite and FE grains were randomly arranged with different connectivities. Therefore, it is very difficult to expect a systematic variation of dielectric values with x values [3]. An assembly of space charges present in an inhomogeneous dielectric medium requires a finite time to line up in an axis parallel to the applied electric field. Hence, the dielectric constant naturally decreases with increasing frequency [20].

A small kink was observed in the temperature-dependent dielectric constant at around 50 Hz frequency in all the composites samples. This is due to the power line frequency. In the present investigation, the NFO is a non-dielectric material; however, it is showing response in dielectric measurements due to the following reasons: (i) "space charge polarization" and "interfacial polarization" at the grain boundary and at the electrodes, (ii) "dipolar polarization" by $Fe^{2+/3+}$ ion pair formation, (iii) "atomic polarization" with strain and vacancies and (iv) "electronic polarization" [21].

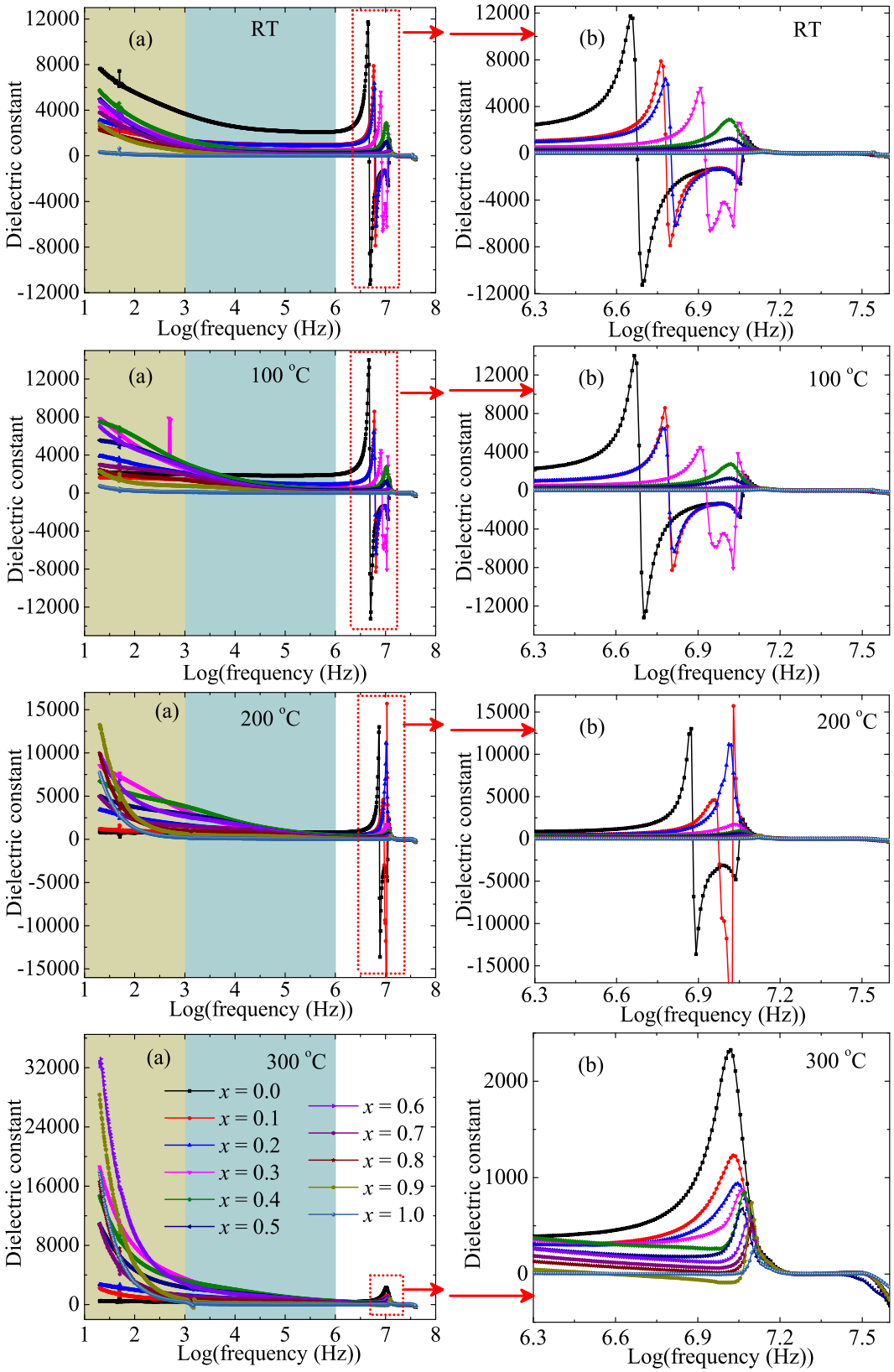

FIGURE 6.6: The frequency−dependent dielectric constant plots of NFO−BTO composites for x = 0 to 1 at RT, 100, 200, 300 °C, (b) magnified plots of figure (a).

The occurrence of piezoelectric resonance in FE and ferrite-FE composites was explained in the literature [26, 27, 28, 29]. In fact, the charged particles in the FE phase are driven to move with the external electric field; in the process, when the frequency of the applied electric field equals the natural frequency of charged particle in motion, then the dielectric resonance takes place [26].

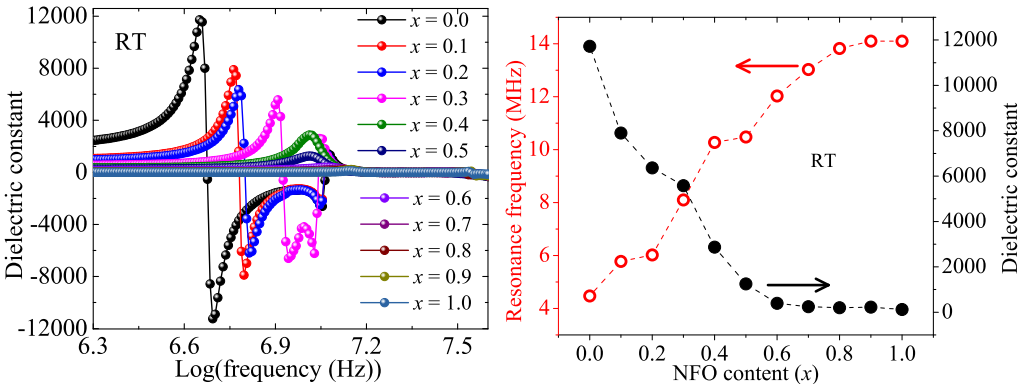

FIGURE 6.7: (a) Frequency−dependent dielectric constant of x=0−1 composite samples at resonance (b) Variation in the resonance and dielectric constant of composites with respective x (NFO content) (dotted line is the guide to eye).

Figure 6.7 shows the resonance observed for composite samples in the present investigation at different temperatures. The values of resonance frequency were found to increase with an increase of x. The observed behavior is quite common in magnetodielectric composites [26, 27, 28, 29]. The reason may be attributed to the effect of the electromagnetic environment on dielectric response. In the present case, the increased NFO in the composite shows increases in the magnetic domain influence on the dielectric permittivity; additionally, the material requires a higher frequency to resonate with it. Therefore, the resonance frequency is increasing with x values [26].

The dielectric constant values were obtained at resonance, and its variation with x is shown in Fig. 6.7. The dielectric constant (at resonance) values were found to decrease with an increase of x. In the present case, the BTO content is being suppressed by the magnetic content as x increases. The overall dielectric nature of the samples decreases; hence the dielectric constant is decreasing with x.

Similarly, the resonance frequency and dielectric constant (at resonance) values were obtained for different temperatures (from 30 °C − 300 °C), and the corresponding plots are shown in Fig. 6.8. The values of resonance frequency were found to increase with an increase in frequency up to x = 0.6, and thereafter it is showing opposite behavior. The reason may be due to increased natural frequency of the dipoles in BTO with increased thermal energy, thereby resulting in the resonance at higher frequencies [26, 29]. In the case of x = 0.6 samples, due to the high concentration of NFO, the piezoelectric resonance frequency is decreasing with temperature because of the more leaky nature of the dipoles. Therefore, the decrease in resonance

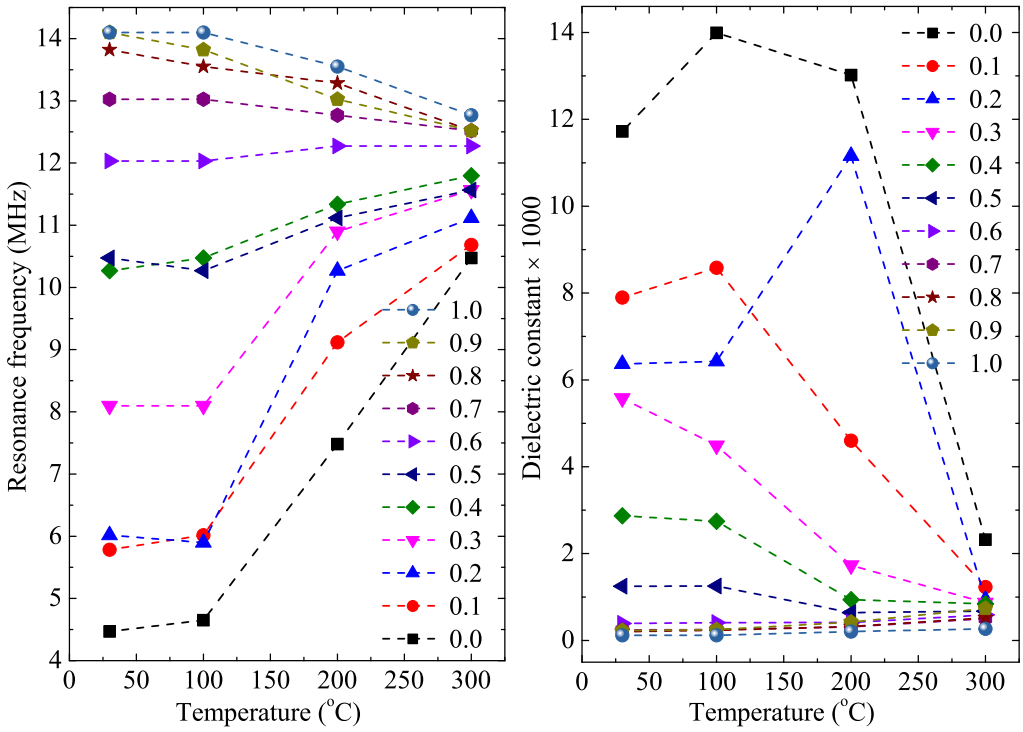

FIGURE 6.8: Variation in the resonance frequency and dielectric constant of NFO−BTO composites with respective temperature (dotted line is the guide to eye).

frequency with temperature was noticed. In fact, the variation of dielectric constant with temperature is varying oppositely with the resonance frequency. The trends are matching with variation in x. A similar reason may be attributed to the observed behavior [26, 29].

6.2 Dielectric loss

6.2.1 Temperature-dependent dielectric loss

Figure 6.9 shows temperature-dependent dielectric loss factor of NFO−BTO samples for x = 0 to 1, in the temperature range, 25 - 225 °C. The small peak was observed in the dielectric loss at around 120 °C corresponds to the phase transition of BTO from FE/tetragonal to PE/cubic phase. The dielectric loss of the single-phase BTO was found to be 0.23 at room temperature, and this value is gradually decreasing with increasing temperature. Similarly, the dielectric loss values for single-phase NFO was found to be 17 at room temperature, and this value increases with the increase of temperature for 1 kHz frequency. Here, in the present investigation, composites' dielectric loss values were systematically increased with an increase in NFO content (x) in the composites. The reason may be due to increased conducting channels that are being facilitated by NFO in the composites. Therefore, the low dielectric loss composite samples may be useful for battery and energy storage applications [22].

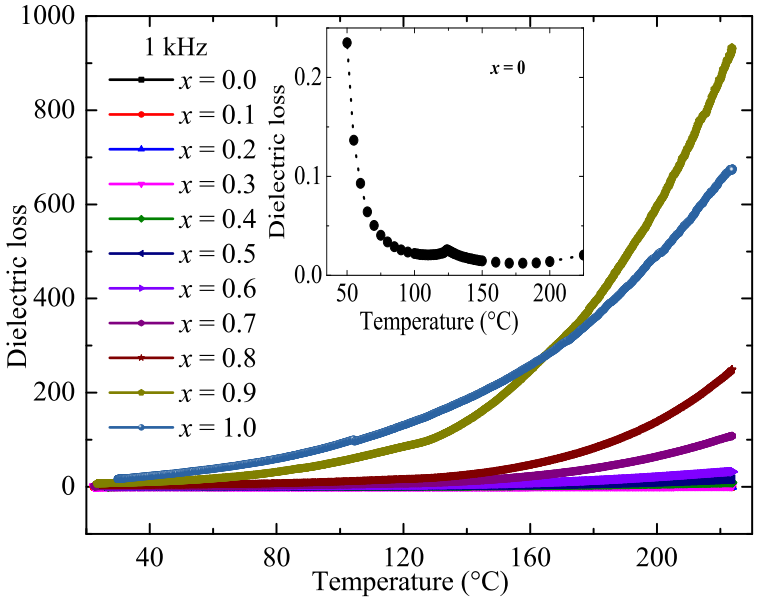

FIGURE 6.9: The variation of dielectric loss with temperature of NFO−BTO composites for $x = 0$ to 1.

In all the samples, the dielectric loss was found to increase with temperature. The dielectric loss factor rises rapidly, which is attributed to the "space charge conduction". The transport of defects such as "oxygen vacancies" to the dielectric-electrode interface is responsible for "space charge conduction" [2]. In summary, the dielectric loss was found to increase with increasing ferrite content in the composites as well as the temperature.

6.2.2 Frequency-dependent dielectric loss

In general, the FE materials are having a high dielectric constant with low dielectric loss, whereas ferrites show a low dielectric constant with high dielectric loss [7, 23]. As discussed in the previous section, the origin of the dielectric loss in the present case is the relaxation of dipoles and the leakage current. It is clear from Fig. 6.10 that the high dielectric loss was observed at lower frequencies and decreases for further increase of frequency. The reason for the observed behavior is due to the losses in "space charge polarization" at the interface of NFO and BTO grains [3].

Generally, ferrites have a high dielectric loss due to it's conducting nature [10]. In the present case, as expected, the dielectric loss was found to increase with an increase in the ferrite content (x) in the composites. Similar to the dielectric constant, the variation of dielectric loss with x can be explained by "Koop's phenomenological theory" [19], based on the underlying conduction mechanism in the composites. As per the "Rezlescu model" [24], the dielectric losses will be less for higher frequencies due to inhibition of domain wall motion. It is a well-known fact that the dielectric loss arises when polarization lags behind the applied ac electric field due to its "grain boundaries", "impurities", and "imperfections" in the crystal lattice [25].

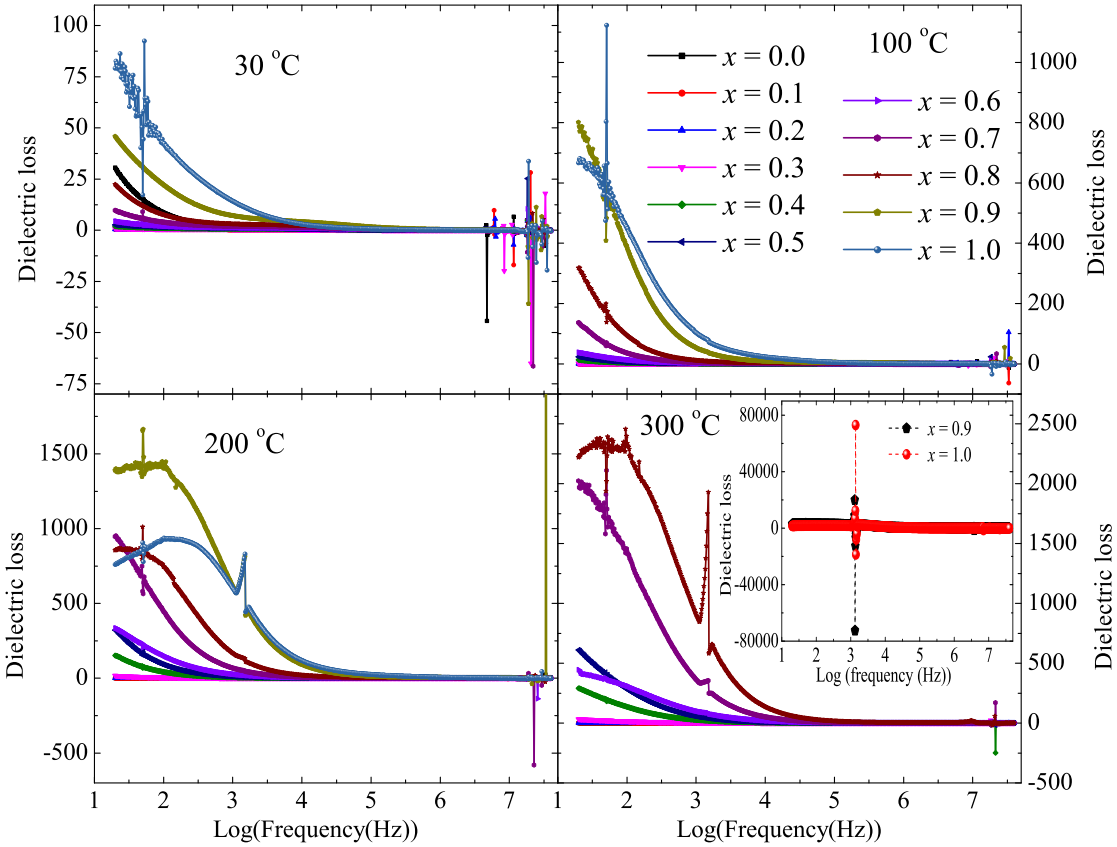

FIGURE 6.10: The frequency dependent dielectric loss of the x = 0.0 to 1.0 composites at 30 °C, 100 °C, 200 °C, 300 °C.

Beyond a 1 MHz frequency, the dielectric loss was found to resonance behavior with an applied external field. At resonance, the dielectric constant and dielectric loss factor were found to show fluctuating behavior. The dielectric loss factor was found to increase with temperature (30 °C to 300 °C) as well as with frequency. Further, the ferrite rich composites were showing humps at around 1 kHz frequency at the temperatures 200 °C and 300 °C. These humps are mainly arising due to the variation of cation distribution (Ni^{2+} and Fe^{3+}) that was occurring due to phase transition of BTO at 120 °C. Therefore, the phase transition might have resulted in electron hopping between the A- and B-sites of mixed spinel structures [20].

6.3 Ferroelectic hysteresis loops

The $P-E$ loop measurements were measured at room temperature for x = 0 – 0.3 samples at 1 Hz frequency and the plots are shown in Fig. 6.11. The x = 0 sample (BTO) shows almost saturated $P-E$ loop with large remanent polarization (P_r = 7.7 μ C/cm^2). The P_r values for x = 0.1 and 0.2 were found to be 2 $\mu C/cm^2$ and 6.6 $\mu C/cm^2$, respectively. Also, the abnormal hysteresis loop observed for x = 0.3 composite sample attribute the lossy behavior mainly arises due to higher content of NFO, which lead to increase in charge leakage in composite [30]. The composite

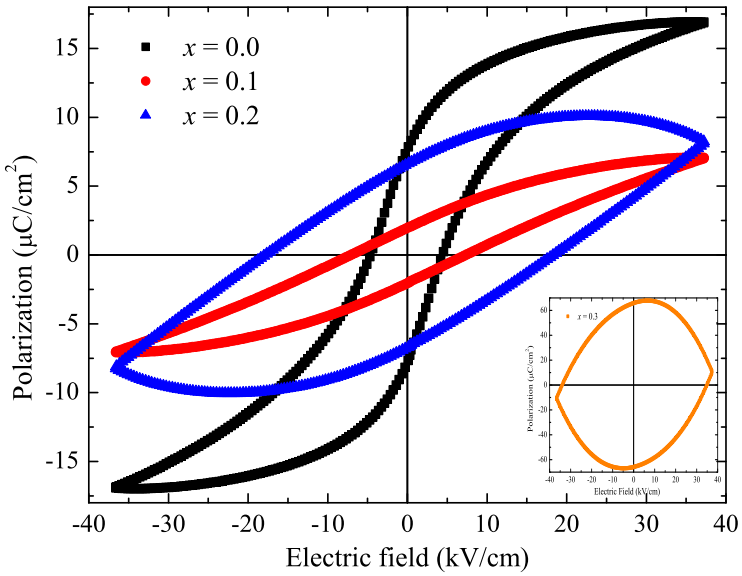

FIGURE 6.11: The ferroelectric hysteresis loops of NFO−BTO composites for x = 0 - 0.3.

samples with $x > 0.3$, the $P - E$ measurements were not performed due to leakage current issue arising from NFO. The electric coercivity values of composite samples are found to be 7.2 kV/cm, 18.1 kV/cm and 34.4 kV/cm for x = 0.1, 0.2 and 0.3 samples, respectively. The value of E_c for x = 0 is found to be 4.5 kV/cm, the value is in good concord with reports for single crystal BTO [31] and it assures the sample quality in the present work. The increase of E_c values with increase in NFO content of composite samples surely attributes the pinning effect arising due to NFO phase [20].

6.4 Chapter summary

The variation of dielectric constant with temperature, frequency of NFO-BTO composites clearly revealing the increase in the FE Curie temperature with NFO content (x) and is independent of frequency. The observed high dielectric constant values for some of the composites were attributed to maximum interface contact between the ferrite and FE hetero-grains. The frequency-dependent dielectric constant is clearly revealing that the values are decreasing with frequency, and dispersion behavior was observed at a lower frequency regime. The observed piezoelectric resonance frequency and dielectric constant values with x were explained by considering different portions of constituent phases. The same parameters (piezoelectric resonance frequency and dielectric constant) variation with temperature was attributed to the stiffness of the FE dipoles. Further, the electric hysteresis loops measured at room temperature for few samples clearly indicating the significant effect of NFO on the FE polarization of BTO.

Bibliography

[1] R. Grigalaitis, M. M. V. Petrovic, J. D. Bobic, A. Dzunuzovic, R. Sobiestianskas, A. Brilingas, B. D. Stojanovic and J. Banys, Ceram. Int. **40,** 6165 (2014).

[2] N. Adhlakha, K. L. Yadav and R. Singh, J. Mater. Sci. **50,** 2073 (2015).

[3] K. K. Patankar, S. S. Joshi and B. K. Chougule, Phy. Lett. A **346**, 337 (2005).

[4] M. N. Siddique, A. Ahmed and P. Tripathi, J. Alloys Compd. **735**, 516 (2018).

[5] B. Jaffe, H. Jaffe and W. R. Cook, Piezoelectric ceramics, 1st edn. Academic Press, London (1971).

[6] J. L. Clabel, F. A. Ferri, F. L. Zabotto, V. A. G. Rivera, I. C. Nogueira, D. Garcia, O. F. delima, E. R. Leite, M. A. P. Silva and C. A. Cardoso, J. Magn. Magn. Mater. **407**, 160 (2016).

[7] R. S. Devan, D. R. Dhakras, T. G. Vichare, A. S. Joshi, S. R. Jigajeni, Y. R. Ma and B. K. Chougule, J. Phys. D: Appl. Phys. **41**, 105010 (2008).

[8] G. R. Mohan, D. Ravinder, A. V. Ramana Reddy and B. S. Boyanov, Mater. Lett. **40**, 39 (1999).

[9] A. S. Gaikwad, S. E. Shirsath, S. R. Wadgane, R. H. Kadam, J. Shah, R. K. Kotnala and A. B. Kadam, J. Magn. Magn. Mater. **465**, 508 (2018).

[10] S. Joshi, M. Kumar, S. Chhoker, G. Srivastava, M. Jewariya and V. N. Singh, J. Mol. Struct. **1076**, 55 (2014).

[11] M. M. Haque, M. Huq and M. A. Hakim, Mater. Chem. Phys. **112**, 580 (2008).

[12] H. Zhang and P. Du, Solid State Commun. **149**, 101 (2009).

[13] M. Zeng, J. G. Wan, Y. Wang, H. Yu, J. M. Liu, X. P. Jiang and C. W. Nan, J. Appl. Phys. **95**, 8069 (2004).

[14] A. A. Bokov and Z. G. Ye, J. Mater. Sci. **41**, 31 (2006).

[15] V. V. Shvartsman and D. C. Lupascu, J. Am. Ceram. Soc., **95**, 1 (2012).

[16] S. Sharma, V. Singh and R. K. Dwivedi, J. Alloy. Compd. **682**, 723 (2016).

[17] G. A. Samara, J. Phys.: Conds. Matter **15**, R367 (2003).

[18] J. Li, Y. Pu, Y. Shi, R. Shi, X. Wang, M. Yang, W. Wang, X. Guo, X. Peng, Ceram. Int. **45**, 16353 (2019).

[19] C. Koops, Phys. Rev. **83**, 121 (1951).

[20] Y. Wang, Y. Wang, W. Rao, M. Wang, G. Li, Y. Li, J. Gao, W. Zhou and J. Yu, J. Mater. Sci. Mater. Electron. **23**, 1064 (2012).

[21] H. Zheng, W. Weng, G. Han and P. Du, J. Phys. Chem. C **117**, 12966 (2013).

[22] R. J. Cava, J. Mater. Chem. **11**, 54 (2001).

[23] N. B. Velhal, N. D. Patil, A. R. Shelke, N. G. Deshpande and V. R. Puri, AIP Adv. **5**, 097166 (2015).

[24] R. C. Kambale, P. A. Shaikh, C. H. Bhosale, K. Y. Rajpure and Y. D. Kolekar, Smart Mater. Struct. **18**, 115028 (2009).

[25] S. Jabez, S. Mahalakshmi and S. Nithiyanantham, J. Mater. Sci: Mater. Electron **28**, 5504 (2017).

[26] Y. Bai, J. Zhou, Y. Sun, B. Li, Z. Yue, Z. Gui and L. Li, Appl. Phys. Lett. **89**, 112907 (2006).

[27] C. E. Ciomaga, I. Dumitru, L. Mitoseriu, C. Galassi, A. R. Iordan, M. Airimioaei and M. N. Palamaru, Scr. Mater. **62**, 610 (2010).

[28] J. I. Gittleman and B. Abeles, Phys. Rev. B **15**, 3273 (1977).

[29] J. P. Zhou, L. Lv, Q. Liu, Y. X. Zhang and P. Liu, Sci. Technol. Adv. Mater. **13**, 045001 (2012).

[30] N. S. Negi, R. Kumar, H. Sharma, J. Shah and R. K. Kotnala, J. Magn. Magn. Mater. **456**, 292 (2018).

[31] G. Venkataiah, Y. Shirahata, M. Itoh and T. Taniyama, Appl. Phys. Lett. **99**, 102506 (2011).

Chapter 7

Summary and future scope

7.1 Summary

The ME multiferroics with room-temperature magnetic and FE order parameters have drawn substantial interest from the "scientific community" in the recent past due to their promising device applications [1, 2, 3]. Due to the scarcity of single-phase, ME multiferroics, the two-phase materials, composed of FM and FE materials with room-temperature ordering, strong ME coupling become important candidate materials in the form of particulate composites with different connectivity and heterostructured bilayer, multilayer thin films, and laminates. In the present thesis, an attempt was made to study the ME coupling in NFO and BTO bulk composites by correlating the structural, morphological, magnetic, and FE properties.

The research findings were presented in the form of a thesis consisting of seven chapters. In summary, the chapter 1 consists of an overview of the thesis and some basic understanding of the topics needed as a background study. This chapter also presents a thorough literature survey on ME multiferroics in general and NFO-BTO in particular. The gap between the work done by others and the present work was explained. A clear motivation behind this present thesis was described. Finally, the chapter also consists of specific objectives of the research work. The chapter 2 summarizes the basic principles involved in the preparation, characterization, and physical property measurements of the NFO-BTO composite materials. Chapters 3 $-$ 6 describe the results obtained in the present work, and chapter 7 summarizes the work with future prospects.

The single-phase NFO, BTO and composites with the formula, (x)NFO + (1-x)BTO with $0 \leq x \leq 1$, were successfully prepared by using SSR method, sintering at 1300 °C. The XRD clearly reveals the required phase formation without any detectable impurity. The Rietveld refinement of XRD data was analyzed, and a systematic variation of lattice parameters with NFO$-$BTO was observed. The measured bulk densities of the samples were found to be 90%. The FESEM measurements both in FE and backscattered modes clearly reveals the clear grain growth with uniform distribution of the phases. The negligible chemical reaction, less lattice mismatch, clear contact interface, and without dead layer in between grains were confirmed

from the present investigation to ensure the promising ME coupling phenomena in these composites.

The temperature-dependent XRD data of the composite samples ensures the structural phase transitions of BTO both in constituent phases and composite samples. The Rietveld analysis of the data depicting the different strain states pertaining to different FE phases of BTO. A significant change in lattice parameters of NFO was noticed in accordance with the phase transitions of BTO. This ensures the significant strain transfer between BTO and NFO phases across the interface. With a view to finding the impact of this strain on cation distribution in NFO, cation distribution from XRD data was analyzed, and found a significant change in the cation distribution. With a view to corroborating these composites' structural properties, the temperature-dependent Raman measurements were done, and data were analyzed. The significant changes in Raman peak positions, the area covered under the peaks revealing the considerable strain transfer across the heterograins of NFO and BTO. The cation distribution in NFO was estimated from Raman data and correlated with XRD data. Finally, the XRD and Raman measurements were clearly showing the signatures of "strain-mediated ME coupling" between NFO and BTO in the present study.

The prominent jumps noticed in M−T curves of composites at the structural phase transitions of BTO clearly indicates the strain-mediated ME coupling in NFO − BTO composites. This is one of the important findings from the present thesis work and a signature of "strain-mediated ME coupling" in NFO−BTO multiferroic composites. The Curie temperature of composites, which corresponds to the NFO, was increasing with an increment of NFO content (x). Magnetic coercivity values were found to decrease with respective NFO content (x) in the composites due to the pinning of magnetic moments with nonmagnetic grains. The magnetic coercivity values were found to be maximum for the equal mole ratios of ferrite−FE materials. The calculated magnetic moment values of the composite samples were corroborated with the magnetic moments calculated from XRD and Raman data. The resonance field of composites was decreasing with the increase in NFO content in composites because of enhanced SE interaction in NFO content. The peak to peak linewidth values of the composites are smaller than single-phase NFO; it indicates the localization of magnetic moments with increasing NFO content. Finally, the impact of strain generated in BTO due to structural phase transitions on magnetic parameters clearly confirms the strain mediated ME coupling in NFO-BTO composites.

With a view to understanding the impact of NFO on the physical properties of BTO, the dielectric and FE polarization measurements were carried out. The T_C of the BTO was increasing with NFO content (x) in the composites. The dielectric constant was found to be maximum in composites due to the maximum contact interface between ferrite and FE materials. The T_C of BTO was found to be independent of frequency in single-phase and composite samples. The frequency-dependent dielectric

constant values were decreasing with frequency, and dispersion behavior was observed at lower frequency region. The piezoelectric resonance frequency increased with the increase of NFO content in composites, whereas the dielectric constant (at resonance) was found to decrease. The high dielectric loss was observed for NFO rich composites, mainly at a higher frequency. The P−E loops measured at room temperature for x = 0 to 0.3 samples clearly indicating the impact of NFO on the physical properties of BTO. Due to leakage issues, electric polarization measurements could not be performed for other samples in the series (x = 0.4 to 1).

7.2 Future scope

It is believed that the work carried out in the present thesis is very much useful for expanding the research in the ME multiferroics, particularly in particulate composites, make them for promising applications at room temperature. The new developments are happening in the field at a rapid pace, giving a scope for further probe onto these materials. The advanced material synthesis/growth and characterization techniques are the key enablers to realize new discoveries and futuristic ultra-low power consumption application devices. In fact, the ME multiferroic materials become material candidates to explore new fundamental science due to the complexity involved in coupling between the "order parameters" via the interactions between "spin", "charge", "orbital", and "lattice" degrees of freedom. The new dimensions in fundamental science lead to different pathways to have a new design and create devices structures, these devices lead to different architectures, and these architectures become a part of new technologies; of course, new technologies will impact the consumer markets. Therefore, there is a promising future for the field of ME multiferroics to explore.

In the future, the present ferrite-FE composite system can be extended to explore the magnetic response in the applied electric field, at least for electrically poled composites to establish ME coupling. This particular demonstration will enable the researcher to realize the magnetization switching under the externally applied field to make the materials suitable for ultra-low power consumption applications.

The synthesis of ME multiferroics itself is a challenging task; optimization and the standardization of preparation methodology enable the researchers to realize new ME materials with promising coupling at room temperature. Therefore, different synthesis techniques need to be explored.

With a view to understanding the underlying ME coupling in this system, the thin film bi-layer and multilayer heterostructures of NFO−BTO are the best candidates. The magnetic response of these heterostructures in the applied electric field and thermal field may be useful for memory and switching applications in devices.

It was noticed from the thesis work that the uniform distribution of grains corresponding to single-phase materials remains a challenging issue. The uniform distribution may give promising ME coupling. Of course, the density of the samples is

also an important issue one needs to focus on it. One can see some focus on these aspects in the future for these particulate composites.

Applications based on domain wall dynamics in the multiferroics materials can be explored for "spintronics", which enumerates new pathways to novel multi - functional devices. Therefore, domain wall dynamics and its manipulation in the applied fields will be an interesting area to explore further.

The ME in nanoscale compounds may be an exciting aspect of the fundamental science viewpoint. It is interesting to explore the underlying ME coupling mechanism in nanoscale materials.

In the end, the progress made in multiferroics has propelled MEs to the cutting edge areas of "condensed matter physics". These material's diverse functionalities may drive the research towards many major scientific queries that exist today-from kitchen to aircraft and beyond.

Bibliography

[1] K. F. Wang, J. M. Liu and Z. F. Ren, Adv. Phys. **58**, 321 (2009).

[2] C. A. F. Vaz, J. Hoffman, C. H. Ahn and R. Ramesh, Adv. Mater. **22,** 2900 (2010).

[3] J. Ma, J. Hu, Z. Li and C. W. Nan, Adv. Mater. **23**, 1062 (2011).

Structural, magnetic and dielectric properties of NiFe2O4-BaTiO3 magnetoelectric multiferroic composites

by Prakash Bongurala

Structural, magnetic and dielectric properties of NiFe2O4-BaTiO3 magnetoelectric multiferroic composites

ORIGINALITY REPORT

10%	4%	8%	2%
SIMILARITY INDEX	INTERNET SOURCES	PUBLICATIONS	STUDENT PAPERS

PRIMARY SOURCES

1	Prakash Bongurala, Venkataiah Gorige. "Structural, magnetic and electric properties of multiferroic NiFe2O4-BaTiO3 composites", Journal of Magnetism and Magnetic Materials, 2018 Publication	2%
2	Song, G.B.. "Subsolidus phase relation, crystal structure and superconductivity of the SmBa"2"-"xSr"xCu"3O"7"-"@d system", Journal of Alloys and Compounds, 20041103 Publication	1%
3	Kranthi Kumar Bestha, Joyal John Abraham, Jeyaramane Arout Chelvane, Venkataiah Gorige. " Influence of cation distribution on magnetic response of polycrystalline Co Ni Fe O (0 ≤ ≤ 1) ferrites ", Physica Scripta, 2020 Publication	<1%
4	Prakash Bongurala, Venkataiah Gorige. "Structural, magnetic and electric properties of multiferroic NiFe2O4-BaTiO3 composites",	<1%

Dr. VENKATAIAH GORIGE
Assistant Professor
School of Physics, University of Hyde
Gachibowli, Hyderabad 500046, I

22/11/2020

Dr. VENKATAIAH GORIGE
Assistant Professor
School of Physics, University of Hyderabad
Gachibowli, Hyderabad 500046, INDIA

22/11/2020

	Journal of Magnetism and Magnetic Materials, 2019 Publication	
5	etheses.saurashtrauniversity.edu Internet Source	<1%
6	hdl.handle.net Internet Source	<1%
7	J. P. Velev, S. S. Jaswal, E. Y. Tsymbal. "Multi-ferroic and magnetoelectric materials and interfaces", Philosophical Transactions of the Royal Society A: Mathematical, Physical and Engineering Sciences, 2011 Publication	<1%
8	Venkataiah Gorige, Raju Kati, D H Yoon, P S Anil Kumar. " Strain mediated magnetoelectric coupling in a NiFe O –BaTiO multiferroic composite ", Journal of Physics D: Applied Physics, 2016 Publication	<1%
9	Submitted to University of Hyderabad, Hyderabad Student Paper	<1%
10	Submitted to Higher Education Commission Pakistan Student Paper	<1%
11	baadalsg.inflibnet.ac.in Internet Source	

73 Granger, Robert M.. "Instrumental Analysis", Oxford University Press <1%

Publication

Exclude quotes	On	Exclude matches	< 14 words
Exclude bibliography	On		

University of Hyderabad
School of Physics
Professor C R Rao Road, Central University P O
Gachibowli, Hyderabad 500046, India

Dr. Venkataiah Gorige
Assistant Professor
E-Mail: vgsp@uohyd.ac.in

Tel: +91 40 2313 4303
Fax: +91 40 2301 0227

November 23, 2020
Hyderabad

TO WHOM IT MAY CONCERN

This is to certify that the thesis entitled "**Structural, magnetic and dielectric properties of $NiFe_2O_4$ – $BaTiO_3$ magnetoelectric multiferroic composites**", submitted by **Mr. Prakash Bongurala** (Reg. No.: 14PHPH10), has been screened by the Turnitin software at the Indira Gandhi memorial library (IGML), University of Hyderabad. This software shows 10% similarity index out of which approximately 3% came from the candidate's own research article (where he is the first author) directly related to this thesis.

From the detailed similarity index report, it is obvious that the remaining 7% of the similarity index, is due to the resemblance caused by the frequent use of the well-known standard terms such as multiferroic, ferroelectric, ferromagnetic, ferrimagnetic, magnetoelectric, strain, phase transition, structure, x-ray diffraction, Rietveld refinement, Raman effect, temperature, spectra, coupling, magnetization, magnetic moment, coercivity, hysteresis loop, resonance, dielectric constant and dielectric loss, etc. to name a few. The use of such terms is rampant in the literature, and hence it is not surprising that the similarity index is artificially inflated. It should be noted that the use of such standard terms cannot be avoided.

23/11/2020

Dr. Venkataiah Gorige
(Thesis supervisor)

Dr. VENKATAIAH GORIGE
Assistant Professor
School of Physics, University of Hyderabad
Gachibowli, Hyderabad 500046, INDIA

Ph.D. Thesis

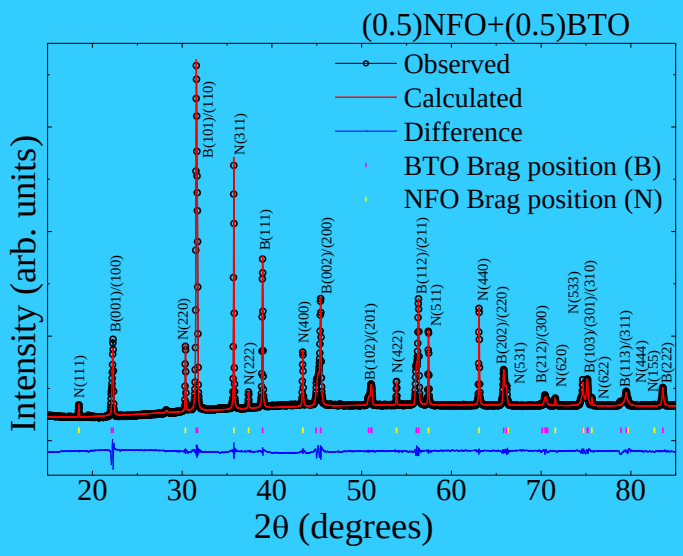

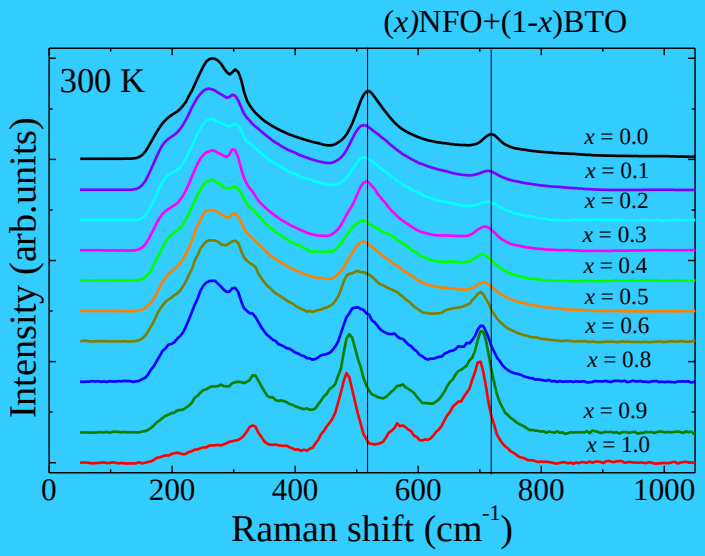

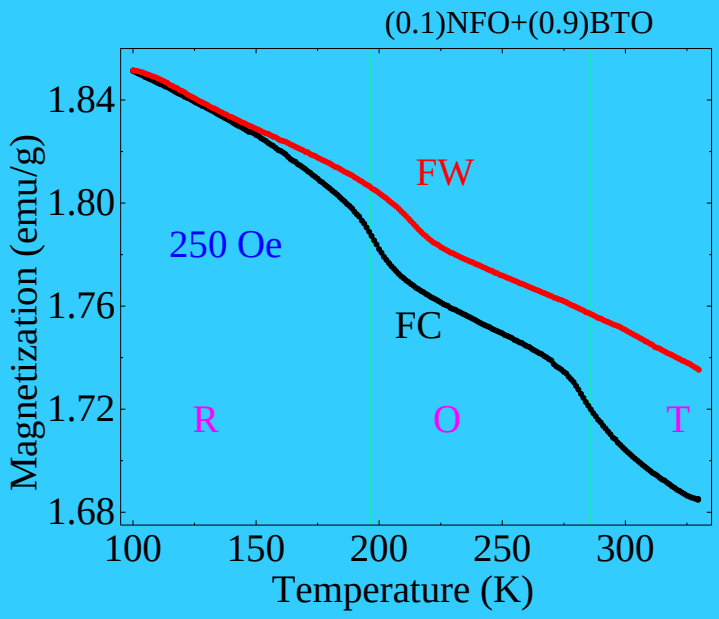

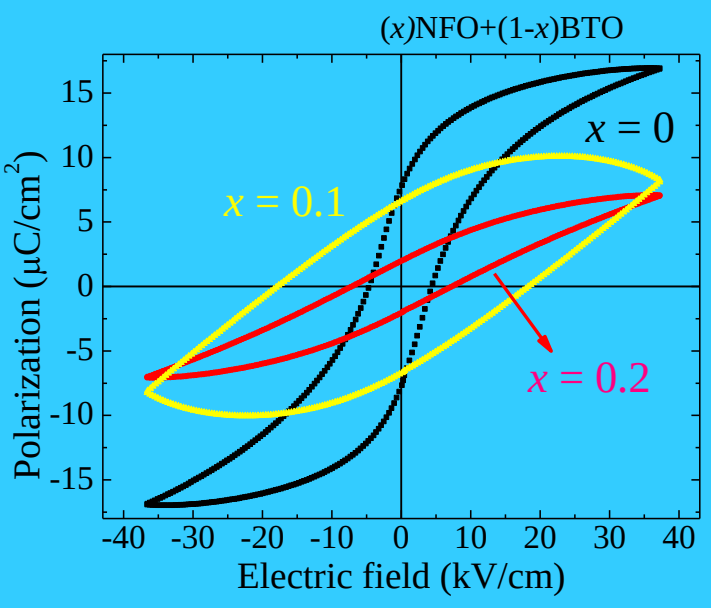

School of Physics
University of Hyderabad
Telangana, India